ELECTRON MICROSCOPY

IN SITU TRANSMISSION ELECTRON MICROSCOPY CHARACTERIZATION OF DYNAMIC PROCESSES INVOLVING NANOSCALE MATERIALS

By JIE YANG, M. A. Sc.

A Thesis Submitted to the School of Graduate Studies in Partial Fulfilment of the Requirements for the Degree Doctor of Philosophy in Biomedical Engineering

McMaster University

McMaster University DOCTOR OF PHILOSOPHY (2018) Hamilton, Ontario
(Biomedical Engineering)

TITLE: *In situ* Transmission Electron Microscopy Characterization of Dynamic Processes Involving Nanoscale Materials
AUTHOR: Jie Yang, M. A. Sc.
SUPERVISOR: Professor Gianluigi A. Botton and Professor Leyla Soleymani
NUMBER OF PAGES: xix, 189

LAY ABSTRACT

Nanostructured materials have been widely used in various fields. *In situ* transmission electron microscopy, a technique used to characterize nanomaterials involved in different dynamic processes in their operating environments, is an advanced tool over the traditional characterization methods such as *ex situ* microscopy and spectroscopy. However, there are several challenges in applying this *in situ* technique to processes occurring in liquid media. In this thesis, an *in situ* transmission electron microscopy system is applied to study the mechanisms of structural changes during different processes in liquids with both high spatial and temporal resolution. Protocols to evaluate and optimize the *in situ* system are developed to provide results comparable with those from their actual applications. Then *in situ* studies on the structural evolution of nanomaterials during electrochemical processes are performed and different theoretical models are applied to describe these processes. Finally, this technique is extended to investigate biomineralization to show its capabilities in future studies on biological processes.

ABSTRACT

The characterization of nanomaterials involved in dynamic processes are conventionally conducted using microscopy, spectroscopy and other physical/chemical methods through the pseudo-dynamic approach. In details, the dynamics processes are recorded by repeating or terminating the process multiple times. However, the above approach can lead to missing important transition information and inducing contamination for mechanistic studies. This motivates the efforts to develop real time characterization techniques which can probe the dynamic change of nanoparticles in their native operating environments. With the capability of probing structural change at the nanoscale, *in situ* transmission electron microscopy, has shown great potential in studies and applications of various processes. Targeting at conducting precise analysis, which has been limited by many uncertainties from electron beam effects and the miniaturized reaction cell used for TEM, the work presented herein pursues a quantitative characterization of a few electrochemical and biological processes through *in situ* liquid-phase transmission electron microscopy.

In this work, the *in situ* transmission electron microscopy system is evaluated by comparing the *in situ* results with those from standard experiments to show its capabilities in studying dynamic processes. The *in situ* system is quantitatively calibrated to obtain the optimized observation conditions to avoid detectable electron beam interference, solution depletion and achieve sufficient resolution for analysis through micrometer thick liquid. These form the fundamentals for the *in situ* studies. Moreover, a comprehensive analysis protocol is established by incorporating multiple *ex situ* and *post situ* characterizations.

Using this optimized *in situ* system, the mechanism of electrodeposition of gold on carbon electrode is studied. The *in situ* results allow quantitative analysis of the growth process. The prevailing diffusion limited three dimensional growth model is examined. A study of the effect of supporting electrolyte on the electrodeposition of palladium is also conducted. The self-limiting, surface diffusion and aggregation/recrystallization growth model is found to describe the early stage of growth, rather than the classical Volmer-Weber growth model. A further study is conducted on the structural evolution of palladium nanoparticles under electrochemical cycling. The mechanisms involved in this process, including electrodeposition, dissolution, hydrogen co-deposition and hydrogen desorption, are studied. The supporting electrolyte, HCl, is found to enhance the dissolution of deposited palladium clusters and induce movements and aggregation of the deposits during the hydrogen interaction process to form chain-like and irregular clusters, which provide direct experimental proof on the morphology formation of palladium with hydrogen involvement. Ultimately, the *in situ* technique is applied to the study of calcium phosphate biomineralization. Combined with multiple *post situ* characterization techniques, the study provides direct experimental evidence of the non-classical pre-nucleation and attachment growth of calcium phosphate structures. This demonstrates the potential of the *in situ* technique for studying the mechanisms involved in biological processes.

ACKNOWLEDGEMENTS

I would like to express my sincerest gratitude and appreciation to my supervisors Dr. Gianluigi A. Botton and Dr. Leyla Soleymani for their guidance, support and patience throughout this research project. They took me to the exciting microscopy world and guide me to explore the world at the nanoscale. Thank you Gianluigi and Leyla for your exceptional mentorship and your creativity and energy in producing new ideas will always inspire me in my future research.

I would like to thank my supervisory committee member, Dr. Igor Zhitomirsky for his help, guidance, and advice throughout this research work. I would like to thank Dr. Glynis de Silveira for arranging trainings on the light microscope, electron microscope and atomic force microscope and providing suggestions and guidance on imaging techniques and analysis.

It is great experience for me to work in the Canadian Centre for Electron Microscopy. I have had great time being with so many excellent staff members. Thank Dr. Carmen M. Andrei, Dr. Andreas, Andy Duft, Chris Butcher and Travis Casagrande for the trainings on different microscopes and their support on experimental establishment. I would like to give my special thanks to Dr. Carmen M. Andrei for her help on TEM imaging.

I would like to thank our collaborators Dr. B. Layla Mehdi and Dr. Nigel D. Browning (Liverpool), Dr. Kathryn Grandfield, Dr. Xiaoyue Wang, Dr. Yingfu Li, Dr. Meng Liu for their contributions to this thesis project. I would like to thank Dr. Gregory Jerkiewicz and his group (Kingston) for their help and guidance on electrochemical techniques. Thank Dr.

Madeline Dukes, Dr. John Damiano, Daniel Frank and other experts from Protochips (Morrisville, USA) who provided help on instrument maintenance.

I am grateful to have been in the two excellent groups from Dr. Botton and Dr. Soleymani and become friends with them. Thanks to the earliest members Christine, Amin, Joey, Stephen, Barnabas and Roqibul from Dr. Solyemani's group, and Guzohen, David, Matthieu, Steffi, Hanshuo, Edson, Sagar and Samantha from Dr. Botton's group. Thank the current lab members Sudip, Amanda, Eric, Yuting, Larona, Sadman, Isobel, Alex, Viktor and other friends. I very much appreciate the opportunities to work with Christine, Guozhen, Barnabas, David and Amin on different projects and I thank Yuting, Eric and Sagar for their help on language corrections on my thesis writing.

I would like to thank Dr. Qiyin Fang for his guidance and suggestions throughout my Ph.D. life. I would like to thank my friends Michel, Zhaojun, Fiona, Alison, Leo, Hugo, Fangfang, Yin, Yushan, Tianyi and Bertha for always being with me- the best memories are those simple moments we spent together.

I would like to thank my family for their constant support. To my parents and grandparents, thank you for encouraging me to overcome the difficulties and initiate a new project from the fundamental basis.

Finally, I wish to acknowledge the Natural Sciences and Engineering Research Council of Canada (NSERC), and McMaster University for their financial support.

TABLE OF CONTENT

LIST OF FIGURES

LIST OF ABBREVIATIONS AND SYMBOLS

AFM	Atomic Force Microscopy
BF-STEM	Bright field scanning transmission electron microscopy
CE	Counter electrode
CA	Chronoamperometry
CV	Cyclic Voltammetry
DI water	Deionized Water
DNA	Deoxyribonucleic acid
EDS	Energy-dispersive X-ray spectroscopy
EELS	Electron Energy Loss Spectroscopy
ILs	Ionic liquids
LC-TEM	Liquid cell transmission electron microscopy
LEC-TEM	Liquid electrochemical cell transmission electron microscopy
LP-TEM	Liquid-phase transmission electron microscopy
OCP	Open circuit potential
Ox	Oxidation
RE	Reference electrode
Red	Reduction
SEM	Scanning electron microscopy
SPM	Scanning probe microscopy
STM	Scanning tunneling microscope
STEM	Scanning transmission electron microscopy
S-H Model	Scharifker-Hills model
TEM	Transmission electron microscopy
WE	working electrode
XPS	X-ray photoelectron spectroscopy

DECLARATION OF ACADEMIC ACHIEVEMENT

The majority of the written work described within the written thesis was conceived, conducted, analyzed, and written by the author of the thesis, in consultation from Dr. Gianluigi A. Botton and Dr. Leyla Soleymani, with the exception to the following:

Chapter 3: Dr. Carmen M. Andrei aided with TEM imaging.

Chapter 4: Dr. Carmen M. Andrei aided with TEM imaging. Yuting Chan did the analysis on particle size and distribution from the *post situ* SEM images. Dr. B. Layla Mehdi and Dr. Nigel D. Browning contributed to the writing of the manuscript.

Chapter 6: Dr. Xiaoyue Wang prepared the sample solution, performed *post situ* XPS and analyzed the data. Dr. Carmen M. Andrei performed the *post situ* TEM-EELS. Dr. Kathryn Grandfield contributed to the writing of the manuscript.

Chapter 1 Introduction

Chapter outline

This chapter discusses the motivation of this thesis work to apply *in situ* electron microscopy to study dynamic processes involving nanomaterials. It firstly introduces different analytical techniques to characterize nanomaterials and nanostructures. Afterwards, a summary of different *in situ* microscopy techniques, including their advantages and challenges, is presented. Then the *in situ* transmission electron microscopy (TEM) system used in this study is introduced. Finally, this chapter concludes with the motivation, objectives, and organization of the thesis.

1.1 Electron microscopy for characterizing dynamic processes involving nanoscale materials

Nanomaterials and nanostructures refer to those materials whose main structural dimensions are in nanometer range[1]. More significantly, these materials exhibit unique physical and chemical properties that are quite different from what are observed at macroscale. The nanoscale properties can be designed and applied to realize various functionalities in our everyday life, such as bio-sensing, catalysis, semiconductors, magnetic materials, optical filters, energy storage and etc. For example, gold nanostructures are used as substrates for biosensors that make medical diagnosis devices portable, miniaturized, and more affordable in resource-poor and remote settings[2]. Nanoparticles from platinum group act as a catalyst in fuel cells, leading to increased efficiency and decreased cost. Fuel cells are clean energy sources that could be widely applied to overcome global energy challenge and solve environmental issues[3]. Nanomaterials are also used as cathode/anode in energy storage devices such as lithium batteries in portable electronics for applications in powering electrical vehicles, stationary power backup for fluctuating energy sources such as wind and solar energy[4]. Characterizing and achieving controllable and precise nanostructured materials/nanostructures has been a prevailing topic since the composition, morphology and dimension of the nanostructures greatly determine their functionalities, such as residual stress, wear resistance, melting point, magnetic properties, chemical reactivity, catalytic properties, optical and electronic properties. If we want to understand the behavior and functionalities of nanomaterials in their operating conditions and how their properties are affected by different processing conditions, for example, how certain nanostructures form, how biomolecules self-assemble on surfaces, how catalysts corrode, or battery electrodes degrade, new analytical tools are needed to observe these processes at different time points and to probe the dynamic changes as they occur. Different techniques have been developed and applied to investigate these changes, including traditional characterization (*ex situ*) methods and the recently developed real time imaging (*in situ*) techniques. For some of the dynamic processes, although they have been under investigation for a long time, both from theoretical and experimental point of view, there still remains controversies over the involved mechanisms and there is plenty of room for further improvement. However, conventional *ex situ* characterization methods have inherent difficulties due to the indirect methods they use: they are carried out separately from the dynamic process under study and they are not able to capture essential kinetic information occurring during some of the most significant events. The recently developed *in situ* microscopy, based on the use of radically different approaches to modify the environment inside the microscope and to realize real time imaging, has shown its potential to probe dynamic processes in the native environment of sample, providing information on the early stage of nanoscale materials growth and/or materials degradation. Due to the limitations of this novel *in situ* technique such as limited resolution and interference of electron beam, however, there are still many developments required to overcome these challenges and perform more reliable analysis of *in situ* experiments.

1.1.1 *Ex situ* characterization on dynamic processes in liquid

Traditional nanomaterials characterization techniques, such as spectroscopies (X-ray dispersive spectroscopy, X-ray diffraction, small angle X-ray scattering, X-ray photoelectron spectroscopy and surface enhanced Raman spectroscopy) and microscopies (optical microscopy, scanning probe microscopy, scanning electron microscopy and transmission electron microscopy) provide information on the morphology, distribution, elemental composition and other structural properties of materials. Since several chemical and biological processes occur in the liquid state, in order to follow the change of the nanomaterials in liquid medium, the sample must be fixed (frozen or dried out) at various stages of the process and microscopy or spectroscopy characterization is carried out on these samples at different time points during such processes. Although this procedure has resulted in major progress in various fields of studies, there are still several limitations to this approach and these have been a major obstacle preventing better understanding of chemical and biological processes. These limitations are as follows:

The variability of samples and the effect of the sample preparation may not be de-coupled from analysis on the dynamic process. Also, under certain conditions, the dynamic information cannot be captured from imaging on fixed samples due to fast transition to different phases, and it is difficult to stop the event "at the right time" to fix the sample. Furthermore, sample preparation process can also alter the sample's state through possible physical and chemical changes during sample treatments and transfer. For example, some nucleation sites or porosities on a surface might be etched or damaged during fixation and transfer to a new sample holder, while some oxygen-sensitive samples may suffer from corrosion, degradation by being exposed to ambient air during preparation before observation in a microscope.

The abovementioned shortcomings have led researchers to the development of advanced *in situ* imaging techniques to provide direct experimental information which might be missed or misunderstood during *ex situ* characterization. Today, based on the developments in MEMS-based devices and new sample holders in the field of transmission electron microscopy, there have been major developments allowing researchers to probe dynamic changes in materials during growth and operation of materials in a liquid environment. This allows the study of nano and micro scale phenomena with better insights than possible with traditional *ex situ* or *post situ* methods.

1.1.2 *In situ* TEM technique and its challenges

Three well-known classes of microscopes- optical, electron and scanning probe microscopes - have been utilized to observe dynamic processes in liquids in real-time (*in situ* imaging). *In situ* imaging was initially based on light microscopy, but this technique has been limited in spatial resolution due to the wavelength limit of photons. For example, even for confocal optical microscopy, a technique commonly used in biological studies, the typical spatial resolution is greater than 100 nm[5]. Since higher resolution has been achieved with scanning probe microscopy (SPM) and electron microscopy (EM), these tools have been used by researchers to observe physical, chemical or biological processes at micro and nano scale. *In situ* techniques based on SPM, such as STM (scanning tunneling microscopy) and AFM (atomic force microscopy), have enabled researchers to observe the morphological changes of materials by scanning a physical probe across the surface[6] and acquiring local real-space information on the structure and morphology of the substrates. These techniques have enabled *in situ* studies on solid-liquid interfaces at the atomic level [6–12]. However, surface analytical imaging techniques also have some limitations: firstly, only the surface morphology can be observed and the structure and phase change inside the material cannot be studied. Secondly, the imaging characteristics and sensitivity is greatly dependent on the specific probes, which can interact with the process under study and lead to difficulties in the interpretation of results. Thirdly, all experiments require a fixed surface where the probe can be used, leading to limitations for materials that are suspended in the liquid. Finally, such probes provide very localized information with limited temporal resolution thus severely limiting *in situ* STM/AFM techniques to effectively realize real-time imaging during the whole dynamic process.

The Transmission electron microscope (TEM) has the potential to overcome the above difficulties. The TEM uses a high velocity electron beam as the imaging source, and electrons are accelerated under vacuum, focused by condenser lenses and passed through the sample. Imaging is realized by (elastic and inelastic) scattering of electrons through interactions with individual parts of material and the environment. The TEM provides both high spatial (down to atomic level) and temporal resolution (up to millisecond per image) as compared to light microscopy, X-ray scattering and diffraction, STM and AFM. Moreover, TEM can combine other analytical technique such as Energy Dispersive X-ray Spectroscopy (EDS), electron diffraction, and electron energy loss spectroscopy (EELS), to provide information not only on the morphology, size and distribution of the materials but also elemental composition and crystal structure, phase and orientation in transient and dynamic states during reaction processes. TEM and scanning TEM (STEM) have been standard analytical tools for solid and dry materials in physical and biological sciences since its invention in 1930's, and lots of efforts have been made to insert a miniaturized liquid cell into the TEM chamber and perform imaging through liquids. However, until a few years ago, *in situ* TEM was only applied into few fields. The long delay between imaging in solid phase and liquid phase was due to several challenges. First, (S) TEM requires high vacuum to allow electrons to travel within the instrument without obstruction. For liquid samples, with the exception of low vapour pressure liquids which can be put into TEM without special preparations[13], most of the aqueous liquids evaporate quickly under high vacuum, making the real time observation impossible. Second, the sample must be thin enough for electrons to pass through: for thick liquids, multiple scattering and absorption of electrons occur, resulting in low quality imaging. Third, the electron beam affects the *in situ* processes and the beam-induced effects must be studied thoroughly and their contribution should be de-coupled from the dynamic process under study. Such interaction between the electron beam and liquid is complicated, and requires complementary investigations. Fourth, the *in situ* system uses miniaturized reaction cells which contain a liquid at the microliter level and the cell is immersed in the high vacuum environment of the microscope. These issues must be considered so that the process occurring inside the miniaturized liquid cell is representative of events in standard reaction cells. Such experiments therefore require quantitative analysis and base level comparison for most of the studies. Lastly, experimental conditions of in the miniaturized liquid cell must be optimized to satisfy imaging quality and decrease beam effect. For example, a high beam dose results in high resolution images but induce strong beam interference, while a thin enough liquid provides high resolution but may result in depletion of reagents under study. A liquid flow reduces beam-induced effect but decreases the spatial resolution, so that the operating conditions must be balanced to achieve high quality imaging in liquid environment. To overcome these difficulties, distinctive designs of liquid cell and control methods have been developed, which are discussed below.

To address the first challenge and place liquid into vacuum, two different kinds of liquid cells have been developed: open liquid cell and enclosed liquid cell.

The open liquid cell uses an environmental chamber for the sample, which creates a wet environment containing mixture of liquid and vapour, this brings the pressure up to 0.2

bar by using differential pumping system and keeps the rest of the microscope under high vacuum at the same time[14]. This is how an environmental (wet) TEM works and it is used in gas and liquid phase studies[14,15]. Recently there is another emerging technique using low vapor pressure liquids such as ionic liquids (ILs) which do not evaporate under vacuum. Therefore, neither a differential pump system nor sealing methods is needed. The interested materials and reactions are maintained inside the liquid, through which *in situ* observation is performed[16–19]. However, the ionic liquids have limited applications since many reactions cannot happen in ILs.

In general, it is difficult to exert much control over an open cell, the resolution is limited by the thickness of the liquid, and it is not possible to characterize dynamic process with a flowing liquid[20].

Enclosed cells, built by sealing a liquid within thin films that are transparent to electron beam, provide a better way to control the liquid thickness. These designs address the second challenge that was discussed above. Today, such approach has become the most prevailing design of liquid cell for the *in situ* system. These cells include lab-fabricated capsules which are compatible with conventional TEM sample holders, and cells that are based on thin film sandwiched within Si based devices. The latter ones are integrated with circuity and circulation systems fitting into specially designed TEM holders so that electrochemistry or heating experiments can be effectively carried out within the TEM.

With regards to the third challenge, the interaction between the electron beam and liquid initiates radiolysis of water and other solutions. The beam effect includes physical and chemical changes, which can be subdivided into direct and indirect effects. Such contributions will be extensively discussed later in chapter 2. Finally, in relation to the fourth challenge, the system has to be evaluated before any *in situ* studies are performed, to assess the beam effect and size scaling issues. Lastly, in order to obtain high quality images with high resolution and contrast, experimental conditions must be optimized, including the setup of liquid cells, preparation of liquid samples and microscope conditions. Such effects will be extensively discussed in chapter 2.

1.1.3 *In situ* liquid cell TEM

The most applied *in situ* TEM system in general uses two electron transparent thin films to sandwich the liquid, and the total thickness can be controlled by adding spacers between the membranes. There have been distinctive designs of liquid cells which differ in terms of materials used for membranes and spacers and sealing methods. In this thesis, we use a liquid cell design with integrated fluid circulation and electric circuitry (Figure 1.1). The system uses silicon nitride membranes to sandwich the liquid in which the sample is immersed. The control of the liquid thickness is achieved by adding spacers between the membranes. All the devices are sealed using O-rings to protect the microscope vacuum.

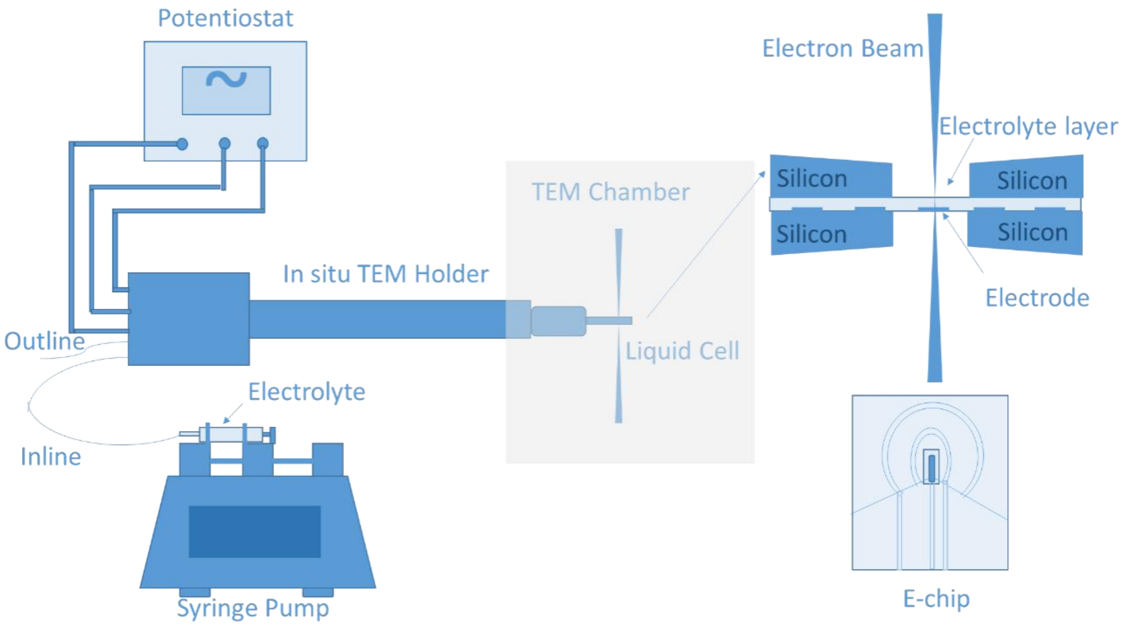

Figure 1.1. A typical commercial *in situ* TEM system for electrochemistry, including the liquid cell TEM holder, potentiostat, syringe pump and E-chips. Top right shows the cross section of the liquid cell inside the TEM chamber and bottom right shows the design of the E-chip with three microelectrodes.

1.2 Motivation

Given the developments in *in situ* liquid cell TEM and the various limitations discussed in the previous section, the motivation of this thesis is to overcome the shortcomings of the traditional characterization methods, such as low accuracy in tracking localized information on individual nanostructures, time consuming sample preparations or multiple retreatments, the possibility of missing intermediate product or transition phase during the whole process, and the difficulties in integrating multiple characterization techniques. Ultimately, the aim is to apply an *in situ* TEM technique with high spatial and temporal resolution, integrated with multiple analytical methods, to observe and quantitatively analyze the behaviour and structural evolution process of different nanomaterials during dynamic processes. This work therefore includes *in situ* studies and analyses to validate hypotheses related to the growth mechanisms of nanomaterials and proposes new models and mechanism related to the dynamic structural evolution of nanomaterials. This thesis will explore how the electron beam interferes with the processes of interest, and how one can decouple the beam-induced effects from the intrinsic changes in the structure of materials. By combining *post situ* characterization, such as SEM, EDS, EELS and XPS and comparing the results obtained *in situ* with *ex situ* characterization, the thesis provides protocols for controlling and understanding the electron beam effects to investigate intrinsic dynamic processes. The ultimate goal of this work is to optimize the *in situ* experimental conditions, decouple these from beam-induced effects, study the structural evolution of nanomaterials during fabrication operation and find or develop appropriate models to describe these processes. In this thesis, *in situ* approaches will be extended to biological processes by observing the assembly of structural building blocks of biomolecules or biominerals into larger assemblies inside model biological solutions.

1.3 Objectives

The objectives of this research can be enumerated as follows:

(1) Evaluating the *in situ* TEM system and optimizing imaging conditions for *in situ* studies (Chapter 3, 4, 5 and 6)

The *in situ* technique has shown great potential in investigating different dynamic processes, but one of the biggest challenges for applying this technique is to convince researchers that the *in situ* procedure is able to mimic the actual process happening in its operating environment and the electron beam interference can be properly evaluated and analyzed. The *in situ* analysis in this study originates from evaluation of the *in situ* system, and starts from the investigation of the electron beam effect. Therefore, by optimizing the *in situ* experimental conditions, we aim to develop appropriate protocols to perform further *in situ* studies.

(2) Performing *in situ* electrodeposition of nanostructures and study the nucleation and growth mechanism (Chapter 3 and 4)

Among the fabrication methods of nanomaterials and nanostructures, electrodeposition is one of the most effective and flexible technique. The advantage of electrodeposition over chemical and physical methods is the high purity of the particles, higher control over the dimension, lower particle size distribution and more control over the density. Electrodeposition is done on a much shorter time scale than other methods, due to the easy and precise structural control and its capability for low cost and bulk production. There are several models that predict the nucleation and growth processes occurring during electrodeposition such as Scharifker-Hills model[21], Scharifker-Mostany model[22], Mirkin-Nilov model[23], Heerman-Tarallo model[24], Bewick-Fleischman-Thirsk model[25] and Surface diffusion and aggregation model[26,27]. We aimed to fit our experimental results in electrodeposition of gold and palladium with these models to assess their validity in predicting current versus time trends and nucleation density.

(3) Performing *in situ* electrodeposition to study the effect of electrochemical conditions on the structural evolution of nanostructures (Chapter 4 and 5)

Noble metallic nanostructures fabricated via electrodeposition are widely used as substrates to immobilize molecular probes for bio-sensing. The morphology and distribution of the deposited nanostructures determine the sensitivity and selectivity of the biosensors. Therefore, we seek to link certain electrodeposition condition and the morphology (and further the functionalities) of nanostructures by the investigating the effect of supporting electrolyte on the growth process of the deposits, and study the mechanism.

(4) Performing *in situ* electrochemical potential cycling of nanoparticles to study the mechanism of structural evolution (Chapter 5)

Electrochemical characterization is an effective technique to analyze the properties of nanostructures. Furthermore, there are some applications of nanomaterials where electrochemical process play an important role on the functionalities. For example, catalyst nanoparticles are electrochemically cycled during the operation of fuel cells, and Li battery materials are electrochemically cycled during charge-discharge process. We aimed at observing structural changes in noble metal catalysts undergoing periodic potential cycling to provide feedback on the design of innovative and potentially improved functional materials.

(5) Exploring *in situ* Microscopy in the realm of bio-mineralization and other biological processes (Chapter 6)

The challenge in applying the *in situ* technique to study biological processes is related in the difficulties in mimicking the actual biological environment in the miniaturized liquid cell, and protecting samples from electron beam damage. Here we aimed to observe the formation and movement of nanoparticles during a bio-mineralization process to demonstrate the potential of applying the *in situ* technique to study biological processes.

1.4 Thesis outline

The thesis outline is summarized as follows.

Chapter 2 provides background information on the mechanism of electrodeposition and characterization methods used throughout this thesis, including electrochemical methods and existing models on nucleation and growth of nanostructures by electrodeposition. The chapter also covers *in situ* microscopy conditions that affect dynamic processes in liquid, especially electron beam effect, including radiolysis of electrolyte in electron microscope and related issues for *in situ* imaging and methods to decrease the beam effect. The chapter also covers the application of the *in situ* liquid cell TEM in various fields, followed by the review of *in situ* studies of electrodeposition.

Chapter 3 concentrates on the quantitative analysis of electrodeposition of gold on carbon electrodes by correlating current transients and corresponding *in situ* STEM images. Electron beam-induced growth and electrochemical deposition are studied separately and an effective strategy is proposed to reduce the amount of beam-induced crystallites to negligible levels. The growth process of gold crystals is quantitatively analyzed by fitting the most prevailing 3D growth model, and *in situ* TEM and *post situ* SEM are compared.

Chapter 4 focuses on the effect of electrolyte on the morphology formation of palladium nanostructures on carbon electrode. Combined with *post situ* scanning electron microscopy, the effect of electron beam on electrodeposition in different electrolyte is analyzed, and a self-limiting, diffusion and aggregation growth model is found to describe the early stage of electrodeposition and explain the morphology formation process.

Chapter 5 focuses on the structural evolution of palladium nanostructures under a periodic potential waveform. Deposition, dissolution, oxidation and hydrogen adsorption/absorption/evolution and desorption processes are observed at different time points during the application of potential. The morphology formation mechanism was studied in different electrolyte. The effect of electrolyte and hydrogen adsorption/absorption/evolution and desorption are analyzed on the morphology formation mechanism of the nanostructures. This work also shows the potential of the *in situ* system to follow and investigate intermediate reaction and products during electrochemical processes.

Chapter 6 expands the *in situ* technique on bio-mineralization studies. It investigates the mechanism of calcium phosphate nucleation and growth process, which is an important process in formation of bones and teeth. The early stage of mineralization process is observed *in situ* from simulated body fluid at the nanoscale. *Ex situ* biomineralization experiments are conducted to compare with the *in situ* observation. *Post situ* characterizations such as X-Ray Photoelectron Spectrometry and electron energy loss spectroscopy are performed to support the *in situ* results. This work also shows the potential of the *in situ* technique in studies on biological processes such as the self-assembly of DNA based nanostructures.

Chapter 7 provides the conclusions of this research, summarizing the key findings, contributions to the field, and potential future work.

Chapter 2 Background

Chapter outline

As discussed in the previous chapter, the *in situ* transmission electron microscopy (TEM) technique is a highly promising tool for studying electrochemical processes[1], for example, the electrodeposition of nanomaterials with high spatial and temporal resolution. This chapter introduces the relevant background on the mechanism of nanostructure evolution with primary focus on electrodeposition. First, the thermodynamic and kinetics of nucleation and growth are discussed, followed by a brief introduction to electrochemical characterization methods. Relevant terminologies such as *overpotential*/*underpotential* are defined, brief introductions to charge transfer mechanisms (e.g., Faradaic vs. non-Faradaic process) are provided, summary of Cyclic Voltammetry (CV) and Chronoamperometry (CA) techniques is presented, and finally, a review of the relevant mathematical models (S-H Model, S-M model, M-N Model and surface-diffusion model) is included. Besides electrochemical methods, this chapter introduces the *in situ* (S)TEM system used for characterizing electrodeposition. A review of the *in situ* liquid cell design is presented. This is followed by a discussion of the effect of experimental conditions used in in situ *microscopy* (imaging mode, resolution and electron beam effect) on the reaction under study. Finally, applications of *in situ* (S)TEM in life science and materials science, particularly with regards to electrodeposition, are reviewed.

2.1 Electrodeposition

---

[1] Electrochemical process refers to the electrons participating reduction/oxidation reactions that happen at the conductor (electrode) and ion conductor (electrolyte) interface.

Electrodeposition is one of the most versatile fabrication methods for developing nanostructured materials. Electrodeposition uses electric current to reduce dissolved cations (e.g., metal ions) to form micro/nano-structures on a given electrode. For example, for electrodeposition of copper from a solution of $CuSO_4$, the Cu^{2+} ions are reduced to Cu by electrons provided from an external power source. Since the study conducted in this thesis work is mostly on in situ characterization of *metal nanostructures* during *electrochemical processes*, in this section we mainly focus on the electrodeposition of metals. Nucleation is the initial stage of electrodeposition during which a small number of ions or atoms become arranged in a pattern characteristic of a crystal solid, forming a growth site upon which additional particles are deposited. Growth results in the subsequent increase in the size of the particle beyond the critical nucleus size, leading to the formation of a well-defined morphology. The theory of nucleation and growth originated from the basic concepts of thermal nucleation and growth, and then the electrochemical analysis methods were incorporated to link the thermal kinetic models. Since the process is controlled by *electric signals* (voltage, current or charge) and the electric response of the system is collected at the same time, the nucleation and growth process is conventionally quantified by measuring and analyzing the *current/voltage transients* and correlating them to different growth models[26].

Here we start with the thermodynamic aspects of nucleation and growth and then introduce electrochemical methods to characterize these processes.

2.1.1 Thermodynamic aspects of electrodeposition

As discussed by E. Budevski *et al*[28], at the electrolyte/ electrode interface, electrodeposition of metals occurs through the following processes:

1. Formation of metal adatoms (adsorbed atoms)[2] on substrates such as native metal[3], or foreign substrate[4] *via* adsorption;
2. Two-dimensional (2D) or three-dimensional (3D) metal phase formation *via* phase transitions (nucleation) and cluster growth;
3. Crystal growth of the 3D metal bulk phase.

According to the classical nucleation and growth model, the processes described in step-2 and step-3 occur through two possible mechanisms. The first is the direct deposition of metal atoms on the growth site; the second is the migration of metal adatoms (through reduction of metal ions on the substrate surface) to the growth sites. If we further consider the most important factors influencing the nucleation and growth mechanism, i.e. the binding energy between the metal adatom and the substrate atom, and the misfit of their lattices parameters, there are three different growth modes, as shown in Figure 2.1.1.

---

[2] Adatom is an atom that lies on a crystal surface, and can be thought of as the opposite of a surface vacancy.

[3] Native substrate refers to a solid with the same material as the depositing material.

[4] A foreign substrate refers to a solid with a different composition from that of the depositing material.

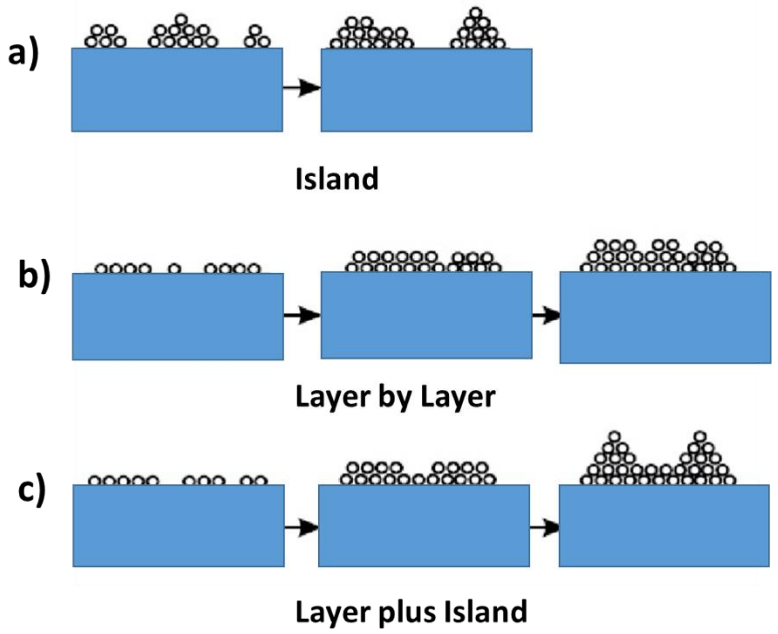

Figure 2.1. Illustration of three different growth modes of metals on foreign substrate: (a), Volmer-Weber island growth; (b), Frank-van der Merwe layer by layer growth and (c) Stranski-Krastanov layer plus island growth. Figure adapted from reference[29].

1. “Volmer-Weber” island growth mode:

If the binding energy of metal adatoms on a foreign substrate is lower than that of metal adatoms on native substrate, then there will be few metal adatoms on the interface of substrate and electrolyte. As shown in Figure 2.1 (a), a 3D metal islands will grow on the substrate surface, without being affected by crystallographic misfit between the metal and substrate.

2. “Frank-van der Merwe” growth mode:

If the binding energy of metal adatoms on the foreign substrate is higher than that of metal adatoms on a native substrate and the metal-substrate crystallographic misfit is very small and can therefore be neglected, the metal adatoms will attach to surface sites resulting in an atomically smooth, fully formed layer. The subsequent full layer then grows on the pre-formed layer. As shown in Figure 2.1 (b), this is a 2D growth process, which is also called *layer by layer* growth mode.

3. “Stranski-Krastanov” growth mode:

Under the same condition of binding energy as described in the *layer by layer* mode, if there exists significant lattice parameter misfit between the crystallographic metal film and the substrate lattice, there will be internal strain in the 2D atom phase. Then 3D metal islands will grow on top of strained 2D overlayers to eliminate the misfit between them, as shown in Figure 2.1(c). This is also called *layer plus island growth mode.*

Metal electrodeposition from aqueous solutions typically occurs by the “Stranski-Krastanov” and “Volmer-Weber” modes. The deposition starts on foreign electrodes with the formation of individual growth centers until a continuous or disperse layer is produced. After sufficient nucleation and growth, the subsequent deposition is becoming more dependent on the electrochemical conditions other than the substrate, since it effectively represents deposition on a native substrate. The growth with non-coherent nucleation results in structures with *defects*[4], which are very important for 3D nanostructure formation.

2.1.2 Electrochemical characterization techniques

Since the growth of nanostructures by electrodeposition is through the transfer of electrons, electrochemical analysis is the process of studying the movement of electrons in an oxidation-reduction reaction and relates the flow of electrons to chemical changes[30]. Electrochemical characterization is the basis for modeling electrodeposition processes. The following content starts with an introduction of the configuration of an electrochemical cell and then introduces electrochemical techniques used to fabricate and characterize nanostructured materials. Afterwards, electrochemical analysis of kinetics involved in electrodeposition and other electrochemical processes are discussed. Finally, the factors that affect the morphology of the nanostructures are reviewed and summarized.

2.1.2.1 Electrochemical cell

All electrochemical processes (including electrodeposition) in this thesis work are performed inside an electrochemical cell. Figure 2.1.2 shows a typical setup of an electrochemical cell. The working electrode (WE), counter electrode (CE), and reference electrode (RE) are immersed into the electrolyte and are connected to an external power source. The power source applies a voltage/current to the cell, and the ions in the electrolyte are transferred between the electrodes. The power source also collects the current, charge or potential, which serve as analytical signals for determining an analyte's concentration or for characterizing an analyte's chemical reactivity[31]. The WE is the electrode on which the reaction of interest is occurring. The potential of the working electrode is measured versus the RE and the current is carried between WE and CE. The three electrode setup in Figure 2.2 can accurately characterize the kinetics of a particular electrode. This configuration has two advantages over the two electrode setup (WE and

CE without RE): First, the RE has a known absolute potential value. Second, the potential polarization of the CE does not interfere with potential measurement between WE and RE. For most electrochemical setups, a relatively large area of counter electrode is used to reduce the impedance at the electrolyte/electrode interface. This is also preferred for electrochemical processes that consume the counter electrode. A small reference electrode close to the working electrode helps to reduce the ohmic drop through the electrolyte.

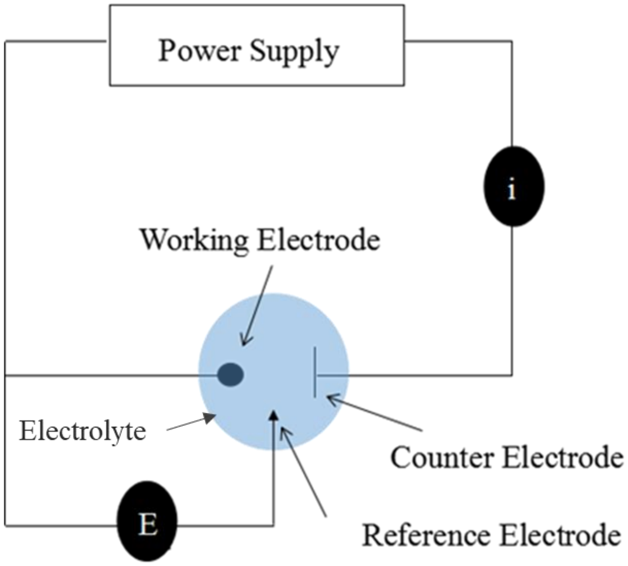

Figure 2.2. Typical three electrode setup of an electrochemical cell. Figure adapted from reference[31].

2.1.2.2 Electrochemical characterization techniques

Using the above electrochemical cell, a number of electrochemical techniques are available to study the formation and properties of nanomaterials. Notable ones are open circuit potential, chronoamperometry and cyclic voltammetry.

Open circuit potential (OCP) is the voltage between working and reference electrode under which there is no current flow through the cell. OCP is often used to determine the equilibrium status of the system, state of charge in a battery, or physical or chemical reactions (for example, specific adsorption) occurring at the electrolyte/electrode interface.

Chronoamperometry (CA) measures the current of the working electrode when a fixed potential is applied between a working electrode and reference electrode. This technique is widely used in electrodeposition to fabricate nanostructures. As shown in Figure 2.3(a), a given potential is applied to an electrochemical cell for a certain amount of time, and the current through WE and CE is acquired as shown in Figure 2.3 (b).

Cyclic voltammetry (CV) measures the current generated following an applied periodic triangular potential waveform (as shown in Figure 2.4 (a)) to the working electrode. CV provides dynamic information on multiple step reactions under a range of potentials.

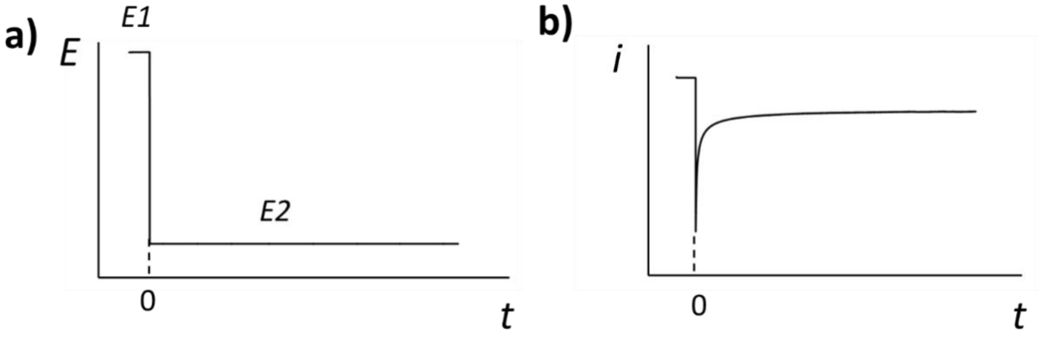

Figure 2.3. Illustration of chronoamperometry. (a): potential wave form applied to an electrochemical cell; (b): current transient in response to the applied potential from (a).

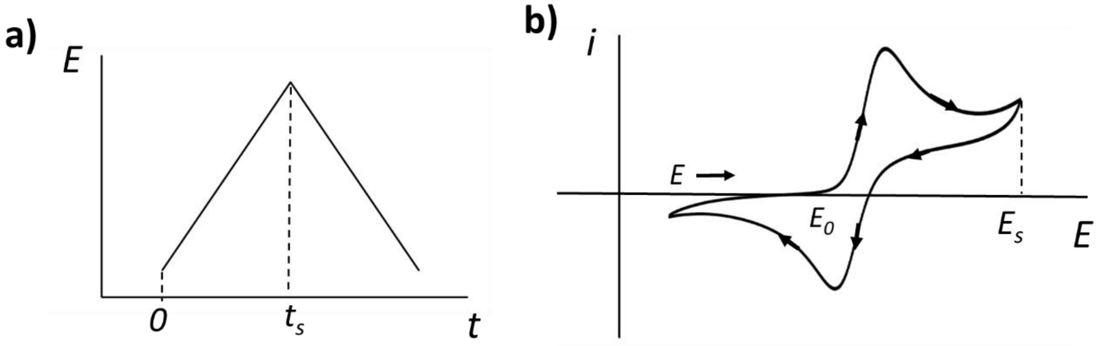

Figure 2.4. Illustration of one cycle from cyclic voltammetry. (a): potential waveform applied to an electrochemical cell; (b): current transient in response to the applied potential from (a).

The study of the growth process of nanostructures in this thesis work is performed using chronoamperometry and the study of the structural evolution of nanomaterials is carried out using cyclic voltammetry. Thus, the following content will focus on the dynamics involved in chronoamperometry and cyclic voltammetry and evolve around nucleation and growth under the influence of electric fields in electrochemical systems.

2.1.3 Dynamics involved in electrochemical processes

In the previous section, the setup of an electrochemical cell and electrochemical techniques were introduced. Here we introduce fundamentals of electrochemical methods describing the conditions under which electrodeposition can occur, how an electrochemical system responds under a given potential, and which kind of dynamic processes take place at the electrode/electrolyte interface.

To electrochemically deposit metals (Me) on a substrate, a voltage or current is needed to provide electrons through WE to reduce metal ions on the electrode surface. A potential or current can also oxidize the deposited metal. The applied potential or current determines the direction of deposition or dissolution (reduction/oxidation) [28].

In an electrochemical system consisting of metal ions (Me^{z+} in an electrolyte) and deposited metal, there is an overall reaction described as[28]:

$$\text{Me (on the substrate)} \rightleftarrows \text{Me}^{z+} \text{(in electrolyte)} + ze^- \qquad (2.1.1)$$

The thermal equilibrium[5] of the above system is given by the **Nernst equation**. The Nernst equation describes the relationship between the electrode potential and the bulk concentration of the Me and Me^{z+} species. For reaction (2.1.1) at thermal equilibrium[28]:

$$E_{Me/Me^{Z+}} = E^{0'}_{Me/Me^{Z+}} + \frac{RT}{zF} ln \frac{a_{Me^{z+}}}{a_{Me}} \qquad (2.1.2)$$

Where $E_{Me/Me^{Z+}}$ is the Nernst equilibrium potential of the cell. $E^{0'}_{Me/Me^{Z+}}$ is the standard potential of the cell. $a_{Me^{z+}}$ and a_{Me} are the activity of the solvated metal ions and the reduced state of the metal ions.

---

[5] The thermal equilibrium refers to a state that the charge transfer, diffusion, chemical reaction processes on the electrode-electrolyte interface are fast enough to be neglected.

The additional potential (beyond the thermodynamic requirement) needed to drive a reaction at a certain rate is called the *overpotential*[31]. The "departure of the electrode potential (or cell potential) from the equilibrium value" is described by the *overpotential*[28]:

$$\eta = E - E_{Me/Me^{Z+}} \tag{2.1.3}$$

For metal deposition on native substrate, the 3D bulk deposition happens at a potential E more negative than the equilibrium potential $E_{Me/Me^{Z+}}$. If E is more positive than$E_{Me/Me^{Z+}}$, the deposited metal is not stable and will be dissolved[28].

The *Nernst equation* only describes the *3D bulk deposition* on a native substrate since the deposition of *3D clusters on a foreign substrate* normally requires more negative potential[28]. However, under certain conditions, *2D metal deposition* occurs at potentials more positive than the equilibrium potential $E_{Me/Me^{Z+}}$ [28]. For example, copper is deposited on a platinum substrate at potentials more positive than when copper is deposited on copper[31]. This is called *underpotential deposition* during which a monolayer of copper is formed on a platinum substrate. Similar to *overpotential*, *underpotential* can also be written as[28]:

$$\Delta \mathrm{E} = E - E_{Me/Me^{Z+}} \tag{2.1.4}$$

Thus, 3D and 2D deposition are related to *overpotential* and *underpotenital*, respectively[28]. If *overpotential* or *underpotential* deposition are carried out under non-equilibrium conditions, the contribution of charge transfer, mass transfer, chemical reactions and adsorption/desorption to the *overpotential* or *underpotential* should also be considered[28].

When a certain potential is applied to an electrochemical system, the total current passing through the electrochemical cell includes non-faradaic and faradic current. The non-faradaic current represents a capacitive process caused by the charge and discharge of the electrode, whereas the faradaic current represents the redox reactions on the electrode. These two different processes are discussed below.

2.1.3.1 Non-faradaic process

When charge is accumulated on or removed from the electrode due to potential change or adsorption/desorption, the electrode-electrolyte interface is considered as bearing a capacitance. The process can then be modeled as an equivalent *resistance-capacitance (RC) circuit*, as shown in Figure 2.5(a).

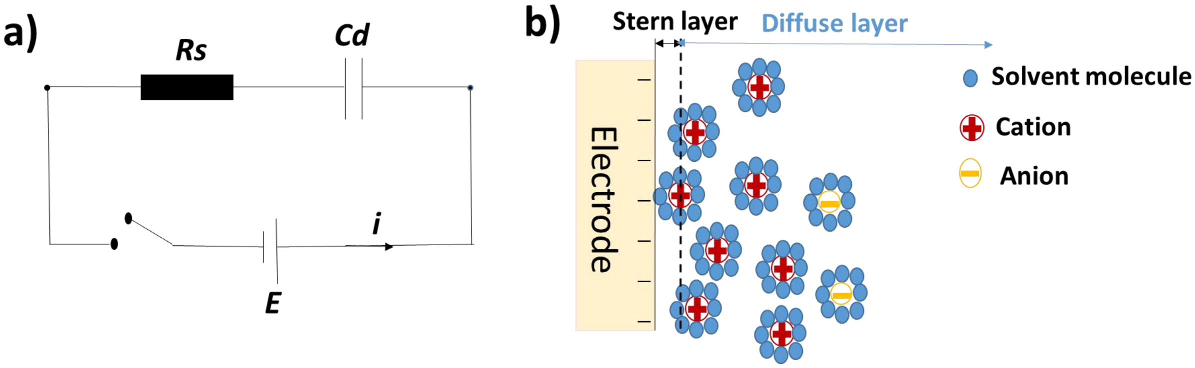

Figure 2.5. Non faradaic process of an electrochemical cell under a step potential. (a): equivalent RC circuit under a step potential and (b): Schematic drawing of the electrical double layer. Figure adapted from reference[32].

The capacitive current, also called "non-faradaic" or "double-layer" current, does not involve any chemical reactions (charge transfer). It only causes accumulation (or removal) of electrical charges on the electrode and in the electrolyte solution near the electrode. At the electrode/electrolyte interface, there are two parallel layers of charge[32], as shown in Figure 2.5 (b). The first layer is a compact layer composed of the positively/negatively charged electrode surface and the counter-ions adsorbed onto it. This is called Stern layer. The thickness of this layer is assumed to be limited to the radius of the ion and a single sphere of solvation round each ion. The second layer is composed of ions attracted to the surface charge. In this layer, called the "diffuse layer", the ions are mobile under the coupled influence of diffusion and electrostatic forces.

The responding capacitive current under a potential step E at a given time *t*, is described as[31]:

$$i = \frac{E}{R_s} e^{-t/R_s C_d} \ , \tag{2.1.5}$$

where R_s is the electrolyte resistance and C_d is the capacitance of the double layer. R_sC_d is the time constant, which determines how fast the current decays after the potential is applied. It drops to 5% of its original value after three times constants ($3R_sC_d$).

For a ramp potential V without pre-charging, the responding current can be described as:

$$i = VC_d[1 - exp\,(- t/R_sC_d)] \tag{2.1.6}$$

The above relationships represent the simplest cases of an electrochemical process. However, in complex situations involving the adsorption of species, multistep charge transfer, or heterogeneous reactions at the electrolyte/electrode interface, the expected behavior would require extensive modeling.

2.1.3.2 Faradaic process

In contrast to the non-Faradaic process discussed above, the Faradaic process represents the chemical reactions occurring on the electrode. To simplify the process, a Faradaic process can be classified into charge transfer and mass transfer limited processes[6].

During a charge transfer limited process, the growth rate is limited by the rate of ions that are incorporated into new phase, and in a mass transfer limited process, the growth is limited by the rate of active species transported from bulk solution to the surface of the electrode. Charge-transfer limited processes normally occur under high concentration and low *overpotentials*, whereas mass transfer limited processes are favoured at low concentrations and high *overpotentials*.

(1) Charge transfer limited processes

If an electrochemical process is controlled by **charge transfer**, it can be described by the **Bulter-Volmer equation** relating the current density j of the electrode to the *overpotential* η on homogeneous surface:

$$j = j_0[\exp\left(\frac{\alpha zF\eta}{RT} - \frac{(1-\alpha)zF\eta}{RT}\right)], \tag{2.1.7}$$

where j_0 is the exchange current density at equilibrium where the reduction and oxidation reactions share the same reaction rate, α is the charge transfer coefficient at the electrode, z is the number of electrons transferred per reduction/oxidation for each metal ion, F is

---

[6] In actual electrodeposition process, there are also other factors that determine the overall rate of the process occurring on the electrode surface, including chemical reactions and other surface reactions such as adsorption and desorption which should be considered based on the conditions of the system under study. But as general information, the two different control categories are introduced here.

the Faraday constant, R is the universal gas constant, and T is the absolute temperature.

Equation (2.1.7) shows that under charge transfer control, the electron transfer rate at the electrolyte/electrode interface is dependent exponentially on the applied voltage. This exponential relationship is the fundamental basis of cyclic voltammetry.

(2) Mass transfer limited process

If the process is controlled by **mass transfer**, three different modes should be considered[33]: diffusion, convection and migration. Diffusion refers to the movement of species under a concentration gradient; convection is caused by stirring or hydrodynamic transport; and migration is the movement of charged species under the effect of electric field. A process involving all these modes is complicated for analysis and, in practice, the conditions of an electrochemical cell are always optimized to maintain only one mode. For example, avoiding vibration and stirring results in reduced convection, and adding a supporting electrolyte[7] reduces the migration of active species in solution.

If we consider the simplest case, a linear diffusion-limited growth process on a planar electrode, according to Fick's first law, the transfer rate of a species at a given location x at time t, written as $J_O(x, t)$ is given by：

$$-J(x,t) = D\frac{\partial C(x,t)}{\partial x}, \tag{2.1.8}$$

and the change of species' concentration with time (*Fick's second law*) is

---

[7] Supporting electrolyte only increases the ionic strength and conductivity of the solution, but does not contain electroactive species within the range of applied potentials. It is sometimes referred to as *inert electrolyte* or *inactive electrolyte*.

$$\frac{\partial C(x,t)}{\partial t} = D\left(\frac{\partial^2 C(x,t)}{\partial x^2}\right) \tag{2.1.9}$$

If we consider an electroactive species[8] transported purely by diffusion to an electrode, and if this is the only species involved in reactions on the electrode, the current on the electrode surface is

$$i = -zFAJ(x,t) = zFAD\left[\frac{\partial C(x,t)}{\partial x}\right],\ at\ x = 0, \tag{2.1.10}$$

combined with equation (2.1.5) and the boundary conditions:

$$C(x,0) = C^*$$

$$\lim_{t \to \infty} C(x,t) = C^* \tag{2.1.11}$$

$$C(0,t) = 0, t > 0,$$

and the current is described by

$$I = \frac{zFAD^{1/2}C}{\pi^{1/2}t^{1/2}}, \tag{2.1.12}$$

Equation (2.1.12) is called **Cottrell equation**.

2.1.4 Theoretical modeling of electrodeposition by chronoamperometry

Cottrell equation describes a diffusion-limited growth process during electrodeposition. It is used in practice to model a growth process by plotting the current vs. $\sqrt{t}$ (square root of time) which can be derived from current time transient obtained experimentally. However,

---

[8] Electroactive species in electrochemical system undergoes chemical reactions in response to electrical stimuli.

this equation does not consider the actual situation of nucleation process that the size of the nuclei are too small that the linear diffusion does not fit the nucleation mode. The transition from nucleation to growth, during the early stages of deposition, is missing, which is a very important component of the studies of the mechanism of electrodeposition. Therefore, more detailed modeling is needed.

Different models and hypotheses have been developed to describe the growth process. These models have shown their ability to describing the electrodeposition process for some specific conditions and systems. However, due to the complex conditions and variations in electrochemical conditions, each model can only fit part of the whole growth process. As new discoveries in new characterization methods have been emerging, there is still plenty of space for improvement. Here we therefore introduce electrochemical characterization methods related to the early stages of electrodeposition and review different models that take into account of the actual conditions so that the models can be improved upon. Since this thesis work mainly focuses on electrodeposition of noble metals on low energy substrate under *overpotentials* using *chronoamperometry*, the growth modes introduced here are basically the 3D growth processes under diffusion control. The following discussion starts from the classical "Volmer-Weber" island growth mode as discussed in section 2.1. This includes the single nucleus growth model and multiple nuclei growth models (known as the Scharifker-Hills Model, and other derived improved models). Furthermore, a recently proposed growth model, which is different from traditional growth models, is introduced.

2.1.4.1 Single nucleus growth mode

As discussed in section 2.1.3, the Cottrell equation assumes a linear diffusion of ions to the individual growing nucleus. However, later studies reported by Hills *et al*[34] propose that, due to the small size of the nuclei, the nucleation is controlled by localized spherical diffusion instead of linear diffusion. For a single hemispherical nucleus growth, the current I is given by：

$$I = zF2\pi rDc = \frac{zF\rho}{M}\frac{dV}{dt} \ , \tag{2.1.13}$$

， where C is the concentration, D is the diffusion coefficient, M is the molecular weight, ρ is the density and V is the volume of the hemisphere. Since $V = \frac{2}{3}\pi r^3$, then $I = \frac{zF\rho}{M} 2\pi r^2 \frac{dr}{dt} = zF2\pi rDC$ and, by solving equation (2.1.13), we obtain:

$$I = \frac{zF\pi(2DC)^{\frac{3}{2}}M^{1/2}t^{1/2}}{\rho^{\frac{1}{2}}} \tag{2.1.14}$$

For multiple nucleation, it is assumed that nuclei grow independently of each other, and the total current can be calculated by the sum of individual currents:

$$I_{N,t} = \sum_1^N I_{i,t} \tag{2.1.15}$$

Where $I_{i,\ t}$ is the current at an individual nucleus i of age t, and N is the total number of nuclei.

The nucleation process can be divided into two different modes: *instantaneous* and *progressive nucleation*. Assuming N_0 is the number of active nucleation sites, at the time when a voltage is applied (i.e., t=0), if the number of nuclei is close to N_0, this is considered as an *instantaneous nucleation* process. On the other hand, if (at time t=0) the number of nuclei is close to zero and, within a short time, the number grows linearly with time t, this is called *progressive nucleation process* (here, $N = k_m N_0$, where k_m is the rate constant for the formation of nuclei).

Combining equation (2.1.14) and (2.1.15), the transient current under a potentiostatic time for:

Instantaneous nucleation is given by:

$$I(t) = \frac{zFN_0\pi(2Dc)^{3/2}M^{1/2}t^{1/2}}{\rho^{1/2}} \qquad (2.1.16)$$

and for *progressive nucleation*:

$$I(t) = \frac{4zFk_mN_0\pi(2Dc)^{3/2}M^{1/2}t^{3/2}}{3\rho^{1/2}} \qquad (2.1.17)$$

Equation (2.1.16) and (2.1.17) show the relationship between the current versus deposition time, which can be used to predict the nucleation process. However, these equations do not consider the nuclei that are formed with interacting with the adjacent ones. Previous studies have shown that there are discrepancies between the growth rate, nucleation density and current[21]. Additionally, studies have found a transition for the relationship of the current versus time from $I{\sim}t^{3/2}$ to $I{\sim}t^{1/2}$, which indicates that there is a progressive regime in the early stage of current transients, thus, the transition from progressive to instantaneous nucleation might be missing if equations (2.1.16) and (2.1.17) are used[21].

2.1.4.2 Multiple nuclei growth mode

Based on the above limitations, Scharifker and Hills developed a model by accounting for the interference between the *diffusion zones* of individual particles and described why nucleation terminated before reaching the theoretical maximum value. In addition, Scharifker and Hills explained the rise and decay of the current transients. Their model, called the **S-H model**, is mostly used to describe the '3D growth' in electrodeposition.

Scharifker and Hills[21] were the first to consider the random distribution of hemispherical nuclei and the overlap of their diffusion zones. According to them, once a nucleus is formed, a "local deformation of the electric field" around the growing centre occurs due to the depletion of concentration under mass transport control as shown in Figure 2.6. Thus, it is impossible for new nuclei to grow in the vicinity of the formed nuclei, but growth can occur at a given distance from the initial nucleus. The *S-H model* treats this overlap of diffusion zones of individual nuclei using *Avrami theorem* (explained below), which is also the basis for other models.

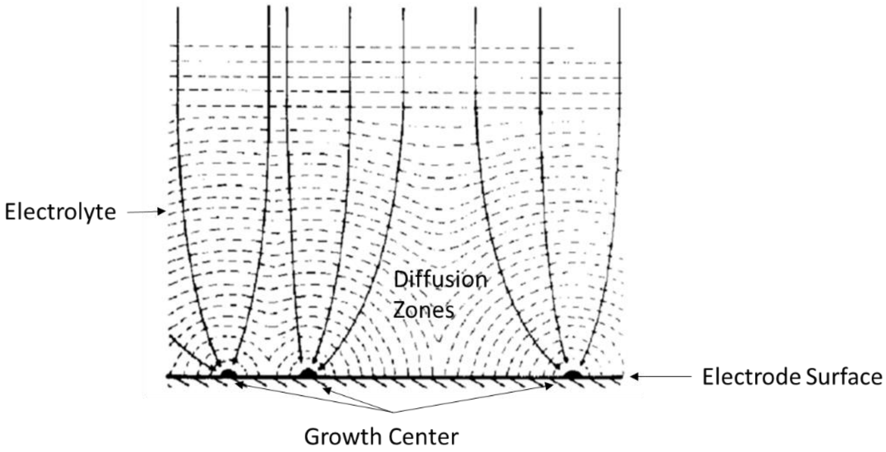

Figure 2.6. Schematic drawing of the growth of diffusion zones of individual nuclei and their overlap during electrodeposition. The arrows indicate the directions of the diffusion field during the growth process. Figure adapted from reference[21].

The *Avrami theorem* describes the relationship between the extended area or volume and the actual covered area or volume. Here, the extended area or volume refers to the fraction of volume or area covered by diffusion zones without overlapping with each other.

The *Avrami* relationship is given by:

$$V = 1 - exp\,(-V_{ex}), \tag{2.1.18}$$

or:

$$\theta = 1 - \exp\,(-\theta_{ex}) \tag{2.1.19}$$

Where V and θ represents volume and area, separately.

If all nuclei form at *t=0*, then: $\theta_{ex} = \pi r(t)^2 = N\pi kDt$, where r(t) is the radius of the hemispherical diffusion zone radiating from a nucleus center growing radially as a function of time *t*. By considering the mass conservation, the S-H model becomes as follows:

For *instantaneous nucleation*:

$$I = \frac{zFD^{1/2}c\theta}{\pi^{1/2}t^{1/2}} = \frac{zFD^{1/2}c}{\pi^{1/2}t^{1/2}}[1 - exp\,(-N\pi kDt)] \tag{2.1.20}$$

For *progressive nucleation*:

$$I = \frac{zFD^{1/2}c}{\pi^{1/2}t^{1/2}}[1 - exp\,(- AN_{\infty}\pi k'Dt^2/2)], \tag{2.1.21}$$

where k and k' are the numerical constants determined by the experimental system, for the instantaneous nucleation, $k = (8\pi cM/\rho)^{1/2}$ and for the progressive nucleation, $k' = \frac{4}{3}(8\pi cM/\rho)^{1/2}$, N_{∞} is the number density of the active sites.

Equation (2.1.20) and (2.1.21) show that the current passes through a maximum and then approaches the diffusion limited current to a planar electrode.

The current and the time corresponding to the maximum can be calculated and equations (2.1.20), (2.1.21) can be written as:

For instantaneous nucleation:

$$\frac{I^2}{I_m^2} = \frac{1.5942}{t/t_m}\{1 - \exp\left[- 1.2564\left(\frac{t}{t_m}\right)\right]\}^2 \tag{2.1.22}$$

For progressive nucleation：

$$\frac{I^2}{I_m^2} = \frac{1.2254}{t/t_m}\{1 - \exp\,[- 2.3367(t/t_m)^2]\}^2 \tag{2.1.23}$$

Equations (2.1.22) and (2.1.23) are widely applied to predict the nucleation process by plotting $(\frac{I}{I_m})^2$ as a function of $\frac{t}{t_m}$ according to the current time transients obtained experimentally.

Although the S-H model provides an improved description of the nucleation process as well as a quick method to identify the process experimentally, later studies found inconsistency between the parameters obtained from the model and those from the experimental data. Scharifker and Mostany[22] suggested that the S-H model treats instantaneous and progressive nucleation separately, which is not always the case in the actual electrodeposition process. Thus, they improved the S-H model (for diffusion limited 3D growth) by developing a new model (called **S-M model**), by defining $k = (8\pi cM/\rho)^{1/2}$ for the nucleation process. Through the S-M model, the two types of nucleation (instantaneous and progressive) do not have to be treated separately. The radius for a single growing hemispherical nucleus is given by: $\mathrm{r} = (kDt)^{1/2}$

And the total current is given by:

$$\mathrm{I} = \left(\frac{\mathrm{zF}D^{\frac{1}{2}}}{\pi^{\frac{1}{2}}t^{\frac{1}{2}}}\right)\left\{1 - \exp\left[-\,N_0\pi kD\left(t - \frac{1-e^{-At}}{A}\right)\right]\right\}, \tag{2.1.24}$$

where A and N_0 can be extracted from the experimental current transient.

The S-M model later was modified to account for the independent nuclei growth before overlapping by considering a uniform concentration gradients over the electrode surface[35]. This means that the thickness of the *diffusion layer* λ is the same for all nuclei, and in this case the current is given by:

$$I = \frac{1}{\alpha(At)^{1/2}}\{1 - \exp\,[\,-\,\alpha(At)^{\frac{1}{2}}\{(At)^{\frac{1}{2}} - e^{-At}\int_0^{\sqrt{At}} e^{\lambda^2}\,d\lambda\}]\} \quad , \tag{2.1.25}$$

where $\alpha = (2\pi)^{\frac{3}{2}}D\left(\frac{Mc}{\rho}\right)^{\frac{1}{2}}(N_0/A)$. When time *t* tends to infinity, this equation becomes the *Cottrell equation* (discussed earlier). However, it has been reported by Mirkin and Nilov[23] and Heerman-Tarallo[24] that the thickness of the diffusion layer λ is also dependent on the nucleation constant. They provided the description of the current under sweeping potential or cyclic voltammetry (as the **M-N model**):

$$I = \frac{(At)^{1/2} - e^{-At} \int_0^{\sqrt{At}} (e^{\lambda^2} d\lambda)}{\alpha(at - 1 + e^{-At})} \{1 - \exp[-\alpha(At - 1 + e^{-At})]\} \tag{2.1.26}$$

The above models predict current transients as a function of time by considering the kinetics occurring during electrodeposition. The M-N model was supported by studies of different systems. There were other models subsequently developed that combined the above three models in order to give the parameters used in the equations a physical meaning[36–38]. There were also models that modified or challenged the *Avrami theorem* by considering the nucleation rate as a function of potential, the concentration of depositing ions, the distance from one single growing nucleus[39], the number of active nucleation sites, nucleation rate, deposition time[40,41], and the variability of the nucleation constant[42,43].

Most of the established models consider that growth during the early stages of electrodeposition is through direct attachment of metal ions/reduced adatoms. These models also exhibited discrepancies between parameters obtained from the models and experimental data[44–46]. One can find studies pointing out that, on low energy substrates, besides the classical Volmer-Weber growth mode, a generalized *electrochemical aggregative growth mechanism* should also be considered[26,27,47], which is introduced below.

2.1.4.3 Surface diffusion and aggregation model

Using high resolution transmission electron microscopy, Ustarroz *et al*[26,27] have found that the early stage of deposition of metals on low energy surface substrate such as carbon, is dominated by surface diffusion, aggregation and coalescence of nanoscale crystals. They also found that the morphology of the deposits depends strongly on the "balance between nucleation, self-limiting growth, cluster surface diffusion, and coalescence" (which in turn, are greatly affected by the type of materials and deposition potential).

2.1.5 Deposition and characterization of nanostructures using cyclic voltammetry

2.1.5.1 Kinetics involved in cyclic voltammetry

As discussed above (section 2.1.4), chronoamperomtery (CA) is one of the most applied electrochemical techniques to fabricate nanoparticles. Besides CA, cyclic voltammetry (CV) is widely used for fabricating and investigating nanostructures. By measuring the current as a function of potential, such as the current vs. potential profile shown in Figure 2.7(b), information on a reaction is obtained by relating the features of the curve to specific processes. Here, we first discuss the dynamics involved in cyclic voltammetry, and then present some examples demonstrating the use of this technique to characterize deposition, oxidation and other featured processes of metal nanoparticles.

Let's consider a reversible reaction containing a redox couple in the solution such as:

$$O + ne \rightleftarrows R$$

Where O and R represent oxidized species and reduced species, respectively.

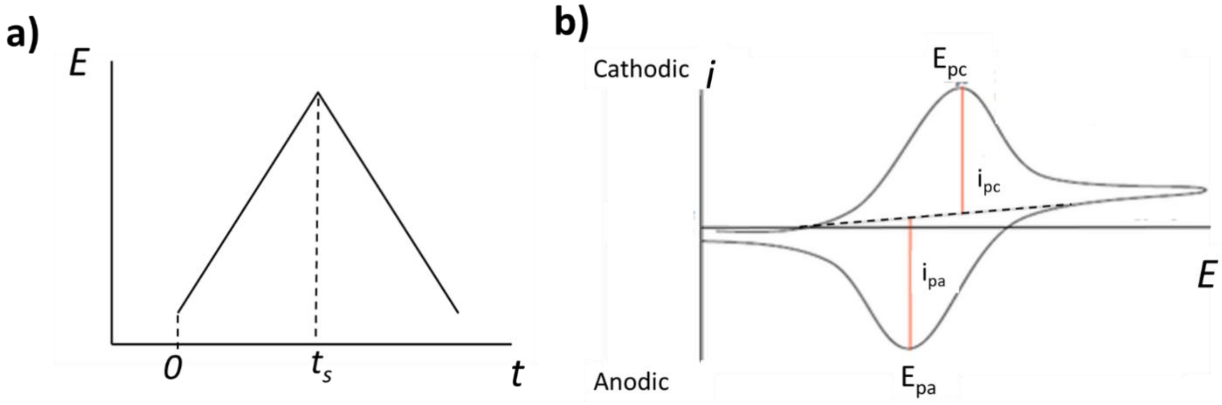

Figure 2.7. Typical cyclic voltammetry on a reversible reaction containing redox species. (a): Single cycle of potential applied to an electrochemical system; (b): Cyclic voltammogram showing the current in response to the potential in (a). The maximum anodic and cathodic currents are referred as the anodic peak current (i_{pa}) and peak cathodic current (i_{pc}), respectively. The potentials at i_{pa} and i_{pc} are called E_{pa} and $E_{pc.}$

As shown in Figure 2.7(a), the potential is applied from an initial voltage where no electrode reaction occurs, and then swept linearly towards negative potentials at the scan rate of v (V/s), the potential can be written as:

$$E(t) = E - vt \tag{2.1.27}$$

As the potential increases towards negative values (the cathodic scan) the concentration of O species on the electrode surface decreases, leading to flux of O (hence a current) to the electrode/electrolyte interface. Since this is a charge transfer limited process, the Faradaic current increases exponentially with the potential, as indicated by Bulter-Volmer equation in (2.1.7). As more O species are reduced by the negatively increasing potential, the concentration of O on the electrode surface decreases to zero, at this point, the diffusion rate of O reaches its maximum value. Therefore, there is a cathodic peak current i_{pc} which indicates the depletion of O at the electrode/electrolyte surface, as shown in

Figure 2.1.7 (b). After this, the following cathodic scan initiates a diffusion limited process. When the scan is reversed (the anodic scan), i.e. the potential is increased towards positive values, the concentration of O species at the electrode-electrolyte interface begins to increase, resulting in further decrease of the anodic current due to a decreased concentration gradient. When the potential passes over the open circuit potential, a similar process for R species occurs as that for O. The anodic peak current i_{pa} indicates the maximum mass transfer rate of R, as shown in Figure 2.1.7(b).

In an electrochemical system with reversible reduction-oxidation reactions of free diffusing redox species, the peak potentials (where the cathodic and anodic currents reach their maximum values) are independent of the scan rate v, whereas the peak current i_p ($i_{pc}= i_{pa}= i_p$) is dependent on the scan rate v and is given by *Randles-Sevcik equation*:

$$i_p = 0.446\, zFAC_o^*(\frac{zFvD_0}{RT})^{1/2} \tag{2.1.28}$$

Where A is the area of electrode surface (usually refers to the *geometrical area*), D_0 is the diffusion coefficient of O species (e.g., metal ions), and C_o* is the bulk concentration of O species.

At 25 °C, for A in the unit of cm^2, D_o in cm^2/s, C_o* in mol/cm^3, and v in V/s, i_p in ampere is given by:

$$i_p = (2.69 \times 10^5)z^{3/2}AD_O^{1/2}C_O^*v^{1/2} \tag{2.1.29}$$

As seen from (2.1.29), the current is dependent on the scan rate and bulk concentration of O in solution. The scan rate controls how fast the applied potential is scanned. Under a high scan rate, the thickness of the diffusion layer decreases at the electrode/electrolyte interface, resulting in higher currents.

2.1.5.2 Characterization of nanoparticles using CV

Figure 2.8 shows a typical cyclic voltammetry profile for poly palladium electrode in an acidic solution. Besides the reduction and oxidation of palladium and the hydrogen evolution[9]peaks, there are symmetric peaks observed at negative potentials between those corresponding to the hydrogen evolution and palladium oxides (PdOx) reduction. These peaks reflect the electro-adsorption/absorption and desorption process which is characteristic of Pt group metals only[48]. There have been extensive studies on the hydrogen adsorption and absorption in metallic electrodes in both theory and applications including hydrogen fuel cells and corrosion sciences[48].

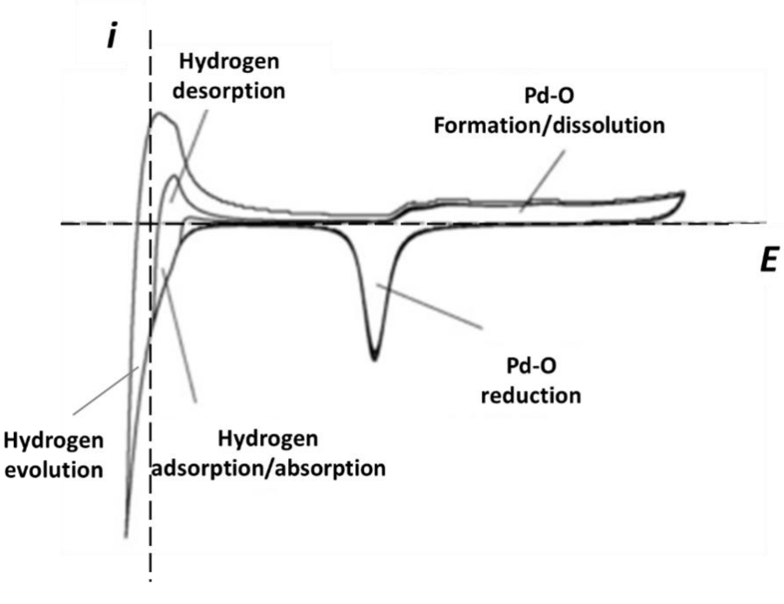

Figure 2.8. Cyclic voltammogram (i-E profile) for (poly) Palladium electrode in H_2SO_4. Figure adapted from reference[49]

---

[9] Hydrogen evolution reaction (HER) refers to the generation of hydrogen through: $2H^+ + 2e^- \rightarrow H^2$.

If a CV is performed on palladium nanoparticles instead of bulk palladium electrode, the CV profile will be different in terms of the shape of the hydrogen adsorption/absorption and desorption peaks as well as the peak potentials. Furthermore, these peaks are dependent on the size and morphology of the nanoparticles. Zalineeva *et al*[50] have compared the CV profiles of palladium nanoparticles with different distribution and morphologies, and identified their unique features in distinct potential ranges. They have shown that, at the *nano-scale*, the three processes including hydrogen adsorption, absorption and evolution occur at different potential ranges. Such effects are not observed for bulk Pd electrodes. Hsu *et al*[51] have also used CV to examine and compare the electrochemical activities of Au-Pd core shell nanoparticles with different sizes used as electrocatalysts in formic acid fuel cells. Thus, CV is an efficient technique to investigate structural/dimensional change of Pt group metal/metal alloy nanoparticles by analyzing the shift of specific peaks and for identifying intermediate products at different potentials.

In general, CV is a powerful analytical technique to investigate the dynamic processes of an electrochemical system and there have been many studies that use CV to investigate the chemical activities of nanomaterials in various fields of applications such as catalysis and energy conversion.

2.1.6 Mechanism of morphology formation in nanostructures

In electrodeposition, it is important to understand the *structural formation mechanism* of nanomaterials to control their structural parameters. In addition to electrochemical methods, this is carried out by microscopy to obtain direct morphological information.

Figure 2.9 shows typical morphologies of gold nanostructures fabricated by electrodeposition. As discussed in the previous section, the growth process can be under charge transfer, mass transport or a mixed kinetic control. Studies have shown that charge transfer limited deposition shows more controllability on the shape of final structures with large grains, whereas mass transport, or mixed kinetics, help to build up three-dimensional structures in nanoscale[4]. Dendrites are typically formed under relatively high *overpotential*s, with charge transfer control over a protrusion and diffusion control over the rest[5] resulting in highly ordered structures and well-defined branches. Needle-like structures are grown under relatively low *overpotential* and under charge transfer control at the tip, and a combination of charge and diffusion control in the rest of the parts[6,7]. Cauliflower-like or globular structures composed of individual nanoscale grains[8] are formed under a spherical diffusion control and generate protrusions, based on which the next generation of protrusions grow inside the diffusion layer of the pre-formed ones[9]. The solution pH affects the size and the structure and roughness of the deposits[10–13]. Organic additives can be incorporated into the deposits or inhibit new growth centers and cause growth along the edge of the crystals. High temperature also results in increased grain sizes.

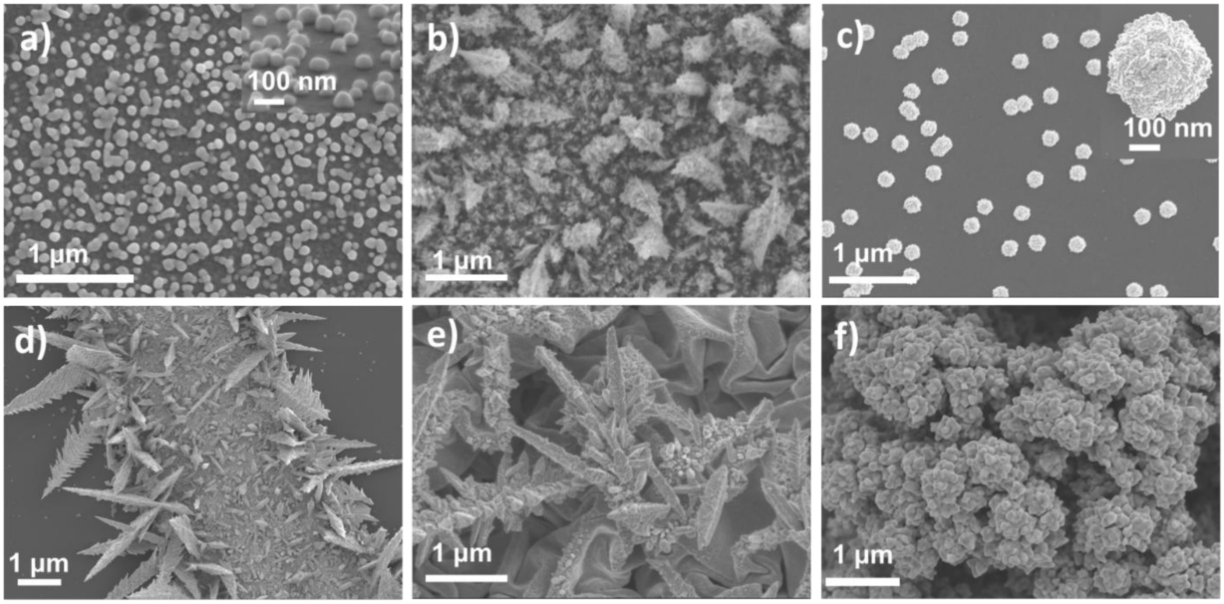

Figure 2.9. Morphology of gold nanostructures on different substrates fabricated by electrodeposition under different electrochemical conditions: (a): smooth semispherical particles on carbon substrate; (b): spiky structures on carbon substrate; (c): spherical structures on carbon electrode; (d) dendrites along the edge of silver electrode; (e): needle-like structures on wrinkled gold structures; and, (f): cauliflower-like structures on carbon electrode.

Studies of electrodeposition should consider the overall effect of experimental conditions. For example, studies have shown that the maximum number of nuclei is determined by the *overpotential*, concentration of the electroactive species, adsorption/desorption processes of inhibiting molecules, and initial metallurgical state of the electrode[1]. It has also been found that a low concentration of metal ions and a high concentration of supporting electrolyte at low temperature without stirring produce dendrites[52]. The nucleation occurs preferentially at surface defects, such as dislocations and steps, and it does not occur simultaneously over the entire electrode. Moreover, there is competition between nucleation and growth, and the nucleation density and arrangement greatly influence the structure of the crystals. For example, large number of grains are formed when there is a high nucleation rate. Therefore, a high nucleation rate combined with a low growth rate normally results in fine grained structure.

2.2 *In situ* TEM

Previous section introduced electrochemical methods to study the mechanism of electrodeposition. As mentioned earlier (Section 2.1.5), another powerful tool to characterize this process is microscopy. The traditional approach has been to carry out the electrochemical analyses and microscopy separately. However, as discussed in Chapter 1, there is a need to combine these two methods to provide an advanced technique to study dynamic processes in real time and at the nanoscale.

The *in situ* TEM analyses used in this thesis enable the real time observations of individual nanoparticles or specific areas during electrochemical/biomineralization processes. The objective here is to collect information on the mechanisms and the intermediate products that are formed during these dynamic processes. As mentioned in Chapter 1, the main challenge here is to design the *in situ* liquid cell and understand the electron beam effects involved (reviewed in later sections). Below, we present a brief summary of the design and challenges of the *in situ* liquid cell.

2.2.1 *In situ* liquid cell

There are different ways to maintain liquid inside the TEM chamber, including using open cells in *environmental TEM* and enclosed cells in standard TEM, as introduced in Chapter 1. Here we focus on the enclosed liquid cell figuration.

The enclosed cell varies in the type of materials used for fabricating the membrane and the spacers. In addition, the sealing method can also be a distinctive factor. The material used for thin films must be electron transparent with weak scattering and have enough mechanical strength to maintain sufficient pressure gradient. *Carbon film*[53], *graphene sheet*[54,55] and *silicon nitride (SiNx)* on silicon support have been used in different liquid cell architectures. The *graphene capsule* provides spatial resolution down to the atomic level[54], and is compatible with conventional TEM sample holders.. However, it is impossible to conduct *in situ* study on electrochemical or heating processes using these capsules in liquid-flow conditions. The *SiNx* membrane on silicon support is the most applied membrane for liquid cells. Although it worsens the resolution due to the increased liquid thickness by adding spacers, as well as the membrane thickness, it greatly extends the *in situ* capability by integrating microelectrodes to realize multiple functions such as heating and electrochemistry. Such cell can fit either in the conventional TEM holder, or the custom-design holder. Some of these cells are also built with a circulation system so that *in situ* studies in fluidic flow can be performed. Here we introduce some typical designs of liquid cell with *SiNx* membranes.

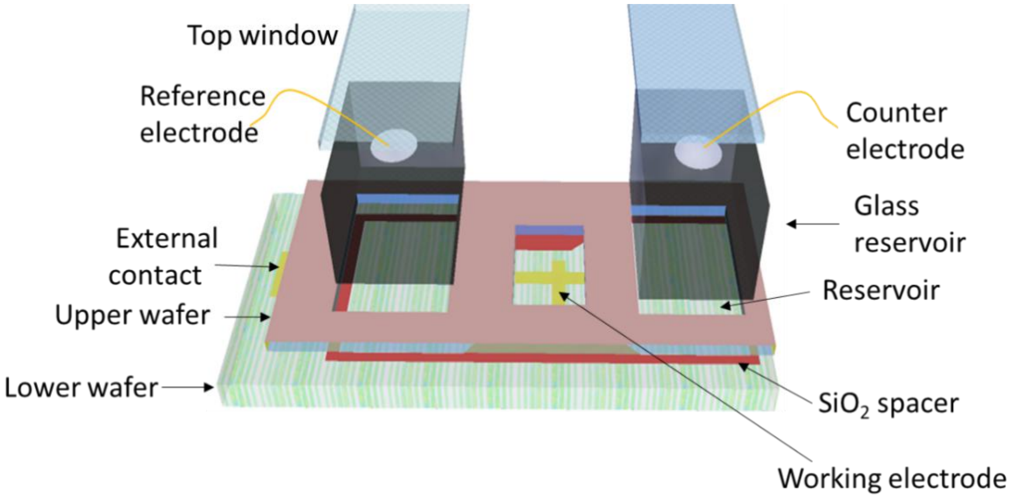

Figure 2.10. Schematic drawing of the liquid cell. The liquid cell has a 100 *nm* thick Si3N$_4$ membrane and a 100×100 µm Si$_3$N$_4$ viewing window. SiO$_2$ (red ring) patterned onto the lower wafer maintains a distance of 0.5-1 µm between the wafers. The upper wafer includes two reservoirs capped with 1mm glass spacers. Liquid flows between the viewing windows using a syringe pump. The cell is then sealed by gluing sapphire lids over the holes in the spacers. Counter and reference electrodes are placed in the two reservoirs, separately. Figure adapted from reference[56]

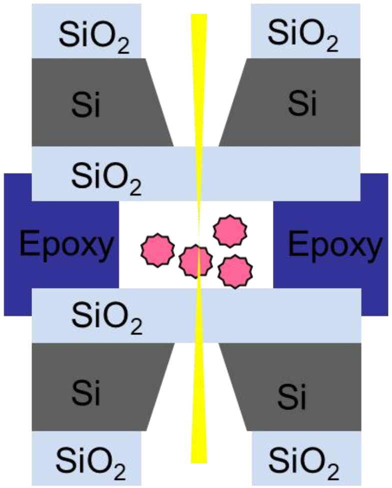

Figure 2.11. Cross-*Section* schematics of the K-kit with living organisms, It is composed of 9 *nm* SiO$_2$ membranes and epoxy as spacers and sealing material. Figure adapted from reference[57].

Williamson *et al*. and Radisic *et al*. used epoxy to seal two 100 *nm* *SiNx* membranes with silicon oxide of 0.5 to 1 μm as spacers[56,58–60] as shown in Figure 2.10. This type of cell fits in a special TEM holder and was used for a series of studies of electrodeposition of copper on metal substrates. Zheng *et al*[61,62] improved this design by decreasing the distance between the two membranes to achieve a resolution of sub-nanometer and refined the dimension to fit into a standard TEM holder. They introduced 200 *nm* indium spacers on thin *SiNx* membrane, between which *in situ* nanoparticle growth and diffusion were studied. Liu *et al*[57] developed a disposable microchip (K-kit) to image live cells and biological processes *in situ*, as shown in Figure 2.11. The kit is fabricated through standard semiconductor processing and fits the conventional TEM. Huang *et al*[63] improved the alignment of two *SiNx* membranes by fitting a protruded wafer into the socket of the other, so they are easily set into position. White *et al*[64] integrated platinum wires on one of the *SiNx* membrane to generate bubbles by Joule heating in the liquid cell and studied the bubble formation process *in situ*. They used gold and palladium as spacers and sealed the cell with epoxy. The aforementioned design of cells all share the same sealing methods of using epoxy. The epoxy may introduce contamination to the liquid and it is hard to control the precise liquid thickness by the amount of epoxy used. In addition, it is difficult to open the cell or reuse it for *post situ* characterization.

Grogan *et al*[65,66] designed the "nanoaquarium" which was sealed through activated plasma wafer bonding resulting in a thin liquid layer ranging from tens of nanometers to a few micrometers depending on the silicon oxide spacers. Electrodes can be integrated on the membrane for functions such as sensing. The cell is mounted on a custom-made titanium holder. Using this system, they conducted real-time imaging of oriented assembly of colloidal crystals, diffusion limited aggregation of nanoparticles, and electrochemical processes.

Similarly, Chen *et al*[67] fabricated two thin film nickel electrodes on *SiNx* membranes and connected micro-wires from the metal electrodes to an external electrochemistry station to observe electrodeposition and electropolishing of nickel nanoparticles. Gu *et al*[68] integrated lithium and single silicon nanowire electrodes into the liquid cell to study the lithiation/delithiation process in liquid electrolytes used in batteries.

Besides these lab-developed liquid cells, there are also commercially-available TEM holders to contain the liquid cell. De Jonge *et al*[5,69–71] fitted their lab-designed liquid cell into a customer designed holder from Hummingbird Scientific, which integrated fluid in and out lines to enable flow inside the cell. They used it in STEM to observe nanoparticle motion and fibroblast cells labeled with gold nanoparticles. *In situ* liquid TEM holders are also developed by Protochips Inc[72–74], these commercial liquid cells are integrated with functions such as Joule heating, electric circuitry and fluid circulation. They are also compatible with analytical techniques such as electron diffraction, electron energy loss spectroscopy (EELS)[75] and Energy-dispersive X-ray spectroscopy (EDS) to provide multiple *in situ* characterizations.

In summary, the materials for spacers should be inert so they do not interact with the liquid samples (until now silicon oxide, noble metals and polymers have been used as spacers). The liquid cell can be sealed by epoxy, wafer bonding or O-rings. Epoxy is the most widely-used method for lab-fabricated cells but easily introduces contamination; the wafer bounding method makes it easy for batch fabrication, but both of the abovementioned sealing methods make the *post situ* characterization difficult. Sealing the cell by O-rings in a specially designed TEM holder solved the above issues and is robust and easy to control.

2.2.2 Imaging mode and resolution

As discussed in Chapter 1, due to the scattering of electrons through the *SiNx* thin film and liquid, it is challenging to maintain high resolution. Some attempts have been made in terms of the liquid cell design. In addition to this, the conditions of the microscope can also be tuned to achieve high quality imaging.

First, the theoretical limit for resolution of different imaging modes should be considered. In TEM mode, a parallel continuous flux of electrons is delivered over an extended area of the sample. In scanning TEM (STEM) mode, a focused electron beam scans across the sample and forms the image by serially integrating the scattered signals to pixel intensity[76]. TEM provides the highest resolution for the object at the electron beam exit side of the *in situ* chip, whereas STEM gives the highest resolution for an object at the electron entrance side[71,77]. The resolution discussed below refers to the highest value for TEM and STEM modes.

It has been calculated that in 1 μm thick water, the resolution of a typical 200 keV TEM, with objective semi-angle of 10 mrad and chromatic aberration coefficient of 2 mm, the resolution is 4 *nm*[77]. For STEM with opening semi-angle of the detector at 70 mrad, the resolution reaches 1 *nm* on top of a 5 μm water layer using probe current of 0.5 nA and a pixel dwell time of 10 μs. If we consider the particles inside the water other than on the top layer (the best resolution), even inside the 1 μm thickness the resolution of below 10 *nm*[69] can be achieved, depending how deep the samples are in the liquid. Related *in situ* studies showed good agreement with these theoretical values[5,69,71].

The temporal resolution of conventional TEM where acquisition is done on a 2D CCD detector is on the orders of 30 ms[78], and the dwell time needed to form each pixel in a STEM image is typically in the range of 1-60 μs[77]. Therefore, for images of 512 by 512 pixels, the acquisition time per frame is from hundreds of milliseconds to a few seconds.

Both TEM and STEM imaging modes are widely applied in *in situ* studies. Comparing the two imaging modes, TEM provides higher temporal resolution and STEM provides enhanced contrast and enables nanometer resolution on thick liquid layers. In general, however, the in situ TEM/STEM provides a combination of high spatial and temporal resolution over the other *in situ* techniques as discussed in Chapter 1.

There are several factors that can improve the resolution of *in situ* imaging. For example, decreasing the liquid thickness or using static liquid instead of flowing will increase the resolution. However astatic thin liquid layer exhibits a series of physical and chemical changes in addition to the processes. The reason for these phenomena (also called *beam effect*) is that besides the imaging source, the electron beam can also heat/charge the liquid or generate radiolysis products, which interact with active species in the liquid as discussed below.

2.2.3 Electron Beam effect on aqueous solutions

It has been reported that the reliability of the *in situ* system is strongly affected by the electron beam[79]. Different phenomena have been observed when exposing aqueous solutions to the electron beam, depending on the composition of the liquid and the number of electrons penetrating the liquid. Such modifications due to the electron beam are called, in broad terms, beam effects. The interactions between the electron beam and the solution and the electron beam and the substrate cause physical and chemical change of the samples in liquid. Here we discuss the electron beam dose, the physical modifications of the environment due to heating and charging, chemical change through radiolysis of liquid, and review the phenomena caused by the electron beam. Furthermore, we discuss experimental procedures to decrease these effects.

2.2.3.1 Electron Beam dose

The electron beam dose rate and dose accumulation are important to quantitatively analyze the electron beam effect. The electron dose rate is defined as the flux of incident electrons through the sample[80]. In TEM mode, the beam dose rate in the unit of electrons per frame per second is calculated by dividing the calibrated beam current by the illumination area and multiplied by exposure time. The electron beam current refers to how many electrons are delivered to the sample per second, and the illumination area is dependent on the magnification. For example, low magnification results in large illumination area. In STEM mode, the beam dose rate is calculated by multiplying beam current with frame time and divided by viewing area. The frame time is dependent on the pixel time and the number of pixels of the image, and the viewing area is determined by the pixel size (varies under different magnification) and number of pixels. In this case, the beam dose rate can be tuned by changing parameters such as probe size, pixel time, and magnification. STEM imaging is considered to provide more controllable, short and localized electron beam illumination, compared with the global irradiation in TEM mode[76]. Both TEM and STEM modes are used in *in situ* studies. For the *in situ* studies in this research, STEM mode has been applied. Cumulative dose indicates how many electrons interact with the sample for a certain period of time. This is calculated by multiplying the beam dose rate by the total exposure time. The beam dose rate is usually used to set up and compare imaging conditions while cumulative dose is applied for quantitative analysis of *in situ* results.

The following content introduces the effects and phenomena caused by the electron beam, and the experimental procedures for decreasing the beam effect.

2.2.3.2 Physical effects

(1) Heating

During the interaction between the electrons and the sample, most of the energy transferred by inelastic scattering ends up as heat within the sample, resulting in a local temperature rise [81]. It has been reported that the thermal effect brought by electron beam is negligible and not likely to bring the local area of solution to the boiling point due to the high heat capacity of water[64,82,83].

(2) Charging

While electrons pass through thin films, secondary and Auger electrons are generated and transmitted through the them[81]. If the material is nonconductive, for example, the *SiNx* membrane, and without any path to be grounded, the transmitted electrons across *SiNx* and the liquid[84] will mostly anticipate in reactions in the liquid instead of recombining the holes generated in the *SiNx* membrane. Therefore, the *SiNx* is positively charged, and it is quite possible that the some metal nanoparticles get charged as well.

The positively charged *SiNx* window, the nanoparticles and the escaped electrons in the solution cause several phenomena, such as the repulsion of existing particles from the viewing area. The direction of the repulsion is almost perpendicular to the membrane into the solution[79,85,86]. This is consistent with previous calculations of electric field distribution,[87] which shows that the direction of the electric field on the membrane is from the beam illumination area to the surrounding uncharged area. The repulsion of nanoparticles is observed under high beam dose rate and relatively high magnification. There are other studies on the mobility [86],surface diffusion, and chain self-assembly of nanoparticles[88], which show that there are physical-chemical processes initiated by the charging of the membrane.

2.2.3.3 Chemical changes

The above sections discuss the physical changes caused by electron beam. In this section, we discuss the chemical changes occurring during the interaction between the electron beam and the liquid. The electron beam effect mostly comes from chemical changes resulting from radiolysis of the solution.

The primary reaction in aqueous solution irradiated by the electron beam is through the radiolysis of water, which is described as follows[89] and illustrated in Figure 2.12.

$$H_2O \rightarrow e^-_{aq},\ H^{\cdot},\ OH^{\cdot}, H_2,\ OH^-,\ H_2O_2, HO_{2,}\ H_3O^+$$

Among the generated radicals, $OH\cdot$ and H_2O_2 are oxidizing species and hydrated electrons, $H\cdot$ and H_2 are reducing species. Hydrated electrons, hydrogen radicals, hydroxide radicals, are the most highly yield radicals compared to all the others[84]. It has been reported that approximately 0.75 mmol/J of radicals are produced through radiolysis of water in the pH range from 3 to 11 under energies between 0.1 to 1000KeV[84]. The stable-state concentration, diffusion coefficient, and lifetime of these radicals determine how they interfere with reactions.

Schneider *et al*[90] conducted studies on radiolysis of water by electron beam and characterized the features of the radicals and the changes caused by radiolysis species. Their studies showed that when irradiation initiated, the amount of radicals rapidly increased and achieved steady state values within about 1 *ms*. For longer time, there were reverse reactions which convert these radicals back to water, maintaining the steady state concentration[90]. There are several factors influencing the concentration or the ratio of reducing to oxidizing species in solution, such as the electron beam dose, solution pH, and the presence of molecular scavengers[91].

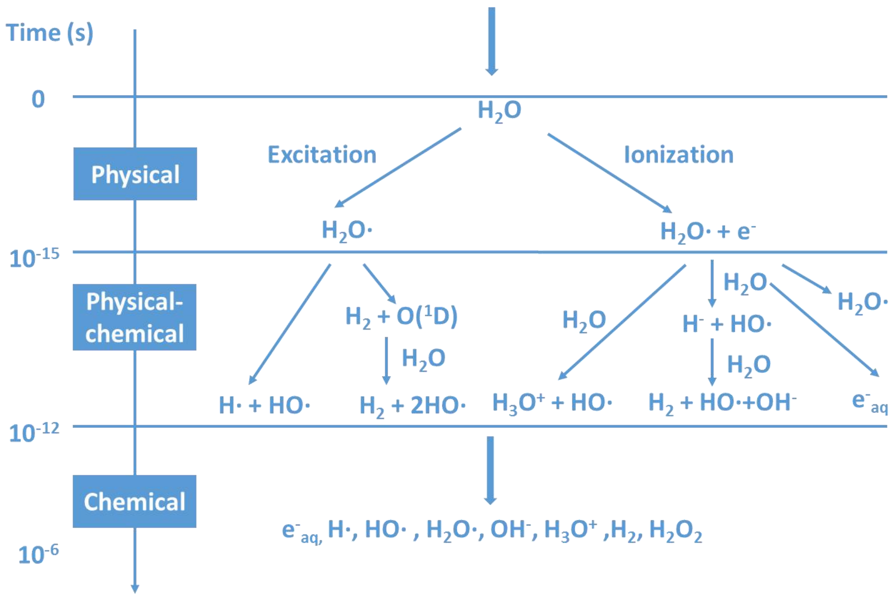

Figure 2.12. Illustration on radiolysis process of water. Figure adapted from reference[84]

For example, the ratio of hydrated electrons over hydroxide radicals decreases when the solution pH decreases, indicating a more oxidizing environment. In water with pH of 0.5, the concentration of hydrated electrons is almost zero, due to rapid recombination of the electrons with hydrogen ions[90]. It is also reported that in pH between 3 and 11, there are almost equal amounts of reducing and oxidizing species generated[84]. Besides pH, beam dose rate is an important factor to determine the steady state concentration and the time that it takes to reach steady state. For example, higher dose rate results in higher concentration of the radicals and the ratio of reducing to oxidizing species also increased with increasing electron dose rate for pure DI water[90]. For certain additives existing in solution, the concentration of the radicals may be reduced. For example, by breaking down some organic molecules through additives, the formed residuals can scavenge $OH\cdot$ radicals and the existing O_2 in liquid can also act as a scavenger of hydrated electrons[90].

The lifetime of each radical and its diffusion coefficient determine how far it interacts with the liquid. Strong reducing species, hydrated electrons and H·, have lifetimes of around 1 microsecond, whereas other species have relatively short lifetime. For example, the life time of highly oxidizing OH· is on the order of ns[92]. A previous study has shown that the hydrated electrons, H· and OH· exist mostly within the radiated area and are rapidly consumed by chemical reactions when they diffuse away. However, there are studies indicating that the diffusion of radicals and solutes in solution can lead to indirect electron beam interactions in areas (about half micron away) not illuminated by the electron beam[76,93,94].

2.2.3.4 Phenomena generated by electron beam

Having defined the possible physical and chemical phenomena generated by the electron beam, we describe here the resulting effects on the operation of the liquid cell, the dynamics of nanoparticles, and the electrochemical studies. The phenomena caused by the electron beam include bubble generation[64,82,86], nucleation and growth of nanocrystals[61,83,95–98], motion of nanoparticles[62,99] including aggregation and repulsion from the viewing area, dissolution of nanostructures[100], and interference with electrochemical[101] and biological processes[102]. Although there are some studies that take advantage of the electron beam to induce controllable growth of desired nanostructures, the abovementioned phenomena are often considered “disruptive” for electrochemical and biological studies. It is also noticeable that the resolution changes due to electron-liquid interaction[77]. The beam-induced effects can be classified in five main categories as follows.

(1) Growth and dissolution of crystals from solution

Both hydrogen radicals and aqueous electrons are strong reducing species that react with aqueous cations to form crystals. There are *in situ* studies on beam induced growth of metals and metal compound such as gold[5,103], platinum[61], palladium[96], silver[80], lead sulfide (PbS)[95], zinc oxide (ZnO)[104], Fe_3Pt[105], and palladium at gold coreshell particles[97]. In these studies, the electron beam was utilized as reducing agent to produce different morphologies of metallic crystals or to build up "shaped" structures by controlling the beam dose rate or solution composition.

On the other hand, high enough cumulative beam dose can cause dissolution of nanoparticles. Jonge *et a*[69,83]*l* studied different behaviors of gold nanoparticles including stable state, coalescence and dissolution by controlling the beam dose rate, solution composition and solution pH.

In our initial stages of work, experiments showed the qualitative changes in the growth and evolution of particles in electrolyte solutions. Figure 2.2.4 shows an example of electron beam induced palladium growth and subsequent damage in a palladium solution of H_2PdCl_4 in STEM mode. Below a given beam dose, there was no visible change in the solution while, as the beam dose rate is increased, the electron beam induces the formation of palladium crystals of increasing size as shown in the Figure 2.13 from (a) to (d) respectively. When the beam dose rate increases even further, the palladium particles started to disappear, as shown in Figure 2.13 from (e) to (h).

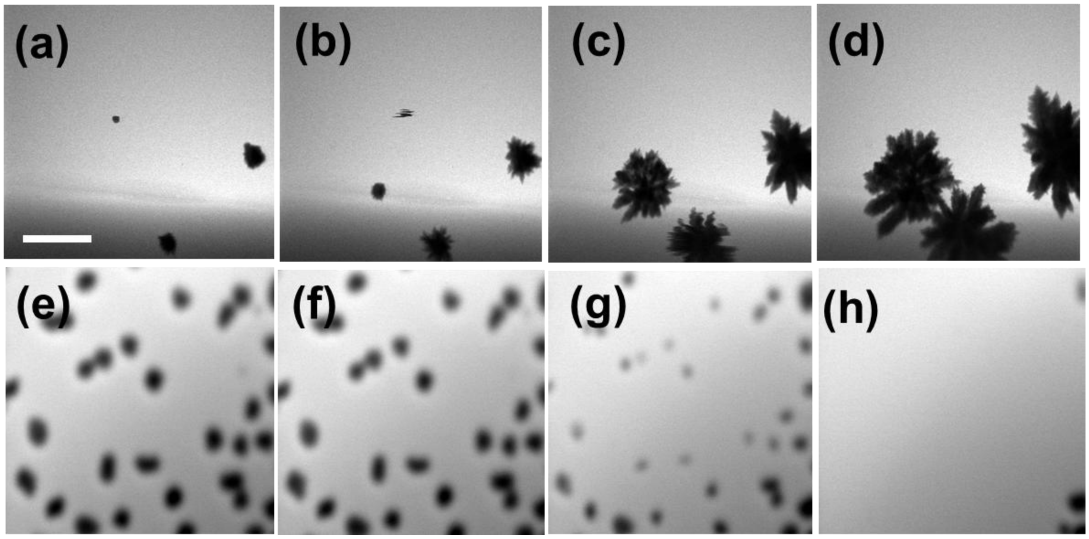

Figure 2.13. *In situ* BF-STEM images showing beam induced growth and damage of palladium crystals from H_2PdCl_4 from (a) to (d) under beam dose rate of 32 electrons/frame.*nm*^{2} and from (e) to (f) under 479 electrons/frame.*nm*^{2} with exposure time from 1s, 10s, 60s and 150s. Scale bar represents 1µm.

Most of literature studies and our work demonstrate that there is a threshold[47,60–62] for electron beam dose rate to initiate the growth of crystals. Below this threshold, no nucleation and growth occurs due to the low concentration of species. Above this threshold (while still at relatively low dose rates), growth of crystals is observed. The value of the threshold varies in different systems and a proper beam dose rate has to be identified for the specific electrochemical system under study.

For example, Woehl *et al*[94] reported that the threshold for the detection of 7 *nm* silver grown from a 1 mM $AgNO_3$ aqueous solution is 50 electrons/(s·nm^2) in STEM mode;. Mehdi *et al*[108] found the threshold of 30 electrons/nm^2·s (in STEM mode) below which no growth of precipitates from the electrolyte of $LiPF_6$/PC was found for their study on Lithium battery cycling. For the in situ studies in this thesis work, the beam does rate was always calibrated first for each system under study. We have found that the beam dose rate of 21 electrons/nm$^{2\cdot}$ frame (38 electrons/nm$^{2\cdot}$ s) in STEM mode is a proper value in general for the systems under study, including 1 mM , 5 mM H_2PdCl_4 (in 15 mM HCl) and 9.5 mM Na_2HPO_4 and 1.7 mM $CaCl_2$ in 125 mM NaCl and 50 mM Tris. By exposing these solutions directly to the electron beam under this dose, no beam-induced growth was observed. However, the beam-induced growth also depends on the conditions of the *in situ* electrochemical cell, which will be discussed in section 2.2.3.5.

(2) Bubble generation

The generation of bubbles has been reported in both TEM [5,79,82] and STEM mode[64]. In TEM mode, bubbles are generated under high beam dose rate and they displace the liquid between the *SiNx* membranes. In STEM mode, increasing beam dose rate generate bubbles, whereas a low beam dose rate cause the bubbles to shrink and collapse. For example, for the liquid cell used in this study, in dilute noble metal salt solutions (a few mill molar) in STEM mode, the beam dose rate of 1900 electrons/nm$^{2\cdot}$s induced bubble generation, and the beam dose rate below 73 electrons/nm$^{2\cdot}$s caused the bubble to shrink and collapse. There are three different origins of for the bubble generation: one mechanism is due to the slow evaporation of the liquid which is heated by the electron beam[109]; the second mechanism is based on the radiolysis of the liquid with bubbles being the mixture of hydrogen and oxygen gas[110]; the third mechanism is based on the bulging of *SiNx* windows, which reduces the pressure in the liquid cell and degases the water[111].

Figure 2.14 shows an example from our work demonstrating a 5 μm bubble generated in water after exposure under beam current of 2.08 nA for about 10 s.

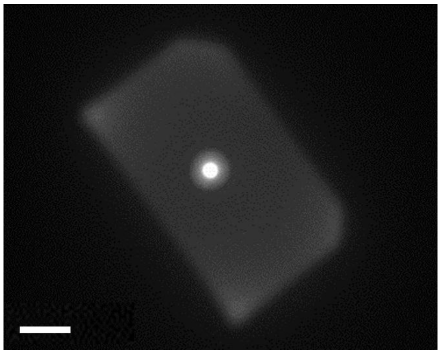

Figure 2.14. Bright field TEM image showing a bubble (bright spot) generated by electron beam with beam current of 2.08 nA in water, the gray square is the overlapping area of *SiNx* window on two silicon chips. Scale bar represents 20 μm.

(3) pH change of the solution

H_3O^+ radicals alter the pH of the solution under beam irradiation. Schneider's study[90] shows that under a low beam dose rate (1000 Gy/s[10], or 0.02 electrons/nm^2·s, for deaerated water) at an initial value of low pH(<3), the pH remains stable, while an increase of beam dose rate causes change of the pH, shifting it towards an acidic regime. This effect is stronger if the initial solution is more alkaline (initially in the 13~14 range).

(4) Diffusion and self-assembling of nanoparticles

Diffusion of nanoparticles under electron beam in liquid has been shown in several studies[19,44,45,52,64,65]. There are several explanations for the mechanism but, in general, it is believed to be a physical-chemical process.

---

[10] The conversion of dose rate in Gy/s (units commonly used in radiation chemistry): multiplying dose rate in electron/m^{2}s by the density normalized stopping power of water (2.798E5 eV m2/kg per electron at 200 kV) and by 1.6E-19 to convert electron-volts to joules.

Schneider gave two hypotheses[90] in his study. The first is that the Debye screening length is reduced due to the increased concentration of ions in solution through beam irradiation, which makes particles lose their repulsive forces between the particles. The second hypothesis is that the colloid particles lose their surface charge due to the change of pH induced by the electron beam.

Woehl and Prozorov[88] observed highly branched chains of gold nanoparticles through aggregation under the electron beam and explained the aggregation as follows Both *SiNx* membranes and the surface of nanoparticles become charged through beam irradiation, and the nanoparticles self-assembled via diffusion-limited aggregation towards the silicon membrane. The difference between the dimension of the chains results from the mobility of the nanoparticles.

(5) Contamination

Exposing water to the electron beam over a short period of time (tens of seconds), results in by-products within the illuminated area on the *SiNx* membrane. The exact chemistry of these by-products is unknown but Woehl *et al*[94] suggested they are carbon contaminants and proposed the formation process as follows. Some organic compounds on the *SiNx* membrane are polymerized by the electron beam and form several nuclei on the membrane, and then additional organic species adsorb to the nuclei's surface to grow into organic structures.

2.2.3.5 Methods to decrease beam effects

I*n situ* studies that use the electron beam for imaging must control the beam to reduce interference effects. The correct interpretation of the results relies on minimizing the beam effects to negligible levels. Based on the phenomena described in the previous section, the primary beam effect are through the radiolysis of the solution. As discussed in previous sections, higher beam dose rate produces more radiolysis species, and there is a threshold below which no reactions happen. Therefore, a moderate beam dose rate is needed to avoid beam induced reactions and while maintaining the imaging resolution.

To decrease the cumulative electron dose, for slowly evolving processes, for example, biological reactions, the beam can be blanked between acquisitions of images. Besides tuning the dose rate, there are some methods to optimize the operating conditions of liquid cells to decrease the beam effect. Conductive materials, for example graphene or carbon film, could be used as membranes to decrease the charging effects observed in SiNx membranes. For the liquid under irradiation, since oxygen causes high yield of radicals at low dose rate[90], removal of oxygen from the solution before *in situ* experiments is of great importance. Also, supporting electrolyte or radical scavengers[91] could be added to react with the electron-beam induced active species in solution. However, this strategy is system dependent and there are no set recipes in using this approach.

There is another effective way to physically remove radicals from liquids by using a flowing solution instead of a static one[111]. A continuous flow of liquid takes away not only the radicals but also the accumulated charge on *SiNx* membrane and the heat generated by electron beam[79].

2.3. Applications of *in situ* STEM/TEM

From the discussions so far we have developed a basic understanding of the electrodeposition process (as well as other dynamic electronic processes) and the liquid cell design. Here we review few prospects in applying these techniques in different fields, such as the life sciences and the material sciences.

2.3.1 Life sciences

One major application of *in situ* (S)TEM techniques in life sciences is in investigating cellular and bacterial activities. De Jonge *et al*[71] showed the capability of the enclosed *in situ* STEM liquid cell to image labelled proteins in whole eukaryotic cells. Several *in situ* studies were conducted by him and his collaborators on the observation of various intracellular components in yeast cells[114] and Mammalian cells, either labeled by gold nanoperticles[115] or quantum dots[116]. The authors also observed *in situ* processes such as the attachment of E. coli bacteria to membrane proteins of Mammalian cells[111] and intracellular uptake of 30 *nm* diameter gold nanoparticles[117]. There are other studies including *in situ* imaging of bacteria[118–121]. Recently Jonge and Peckys[102] proposed that the *in situ* (S)TEM on live cells cannot reflect the actual biological process due to the beam damage to the cell[102], and the better alternative is correlative light and electron microscopy, which was also applied in *in situ* observation of cells[116,121]

2.3.2 Materials sciences

In situ applications in materials science include beam induced growth or dissolution of crystals, motion of nanoparticles, nanobubble generation, and electrochemistry. Here we summarize recent studies in beam induced growth, phase transition, dissolution and motion of nanostructures. The electron beam can initiate nanoparticle nucleation and growth in a liquid, or dissolve them, depending on beam dose rate. *In situ* studies include beam-induced growth of platinum[61], gold[98,107], silver[80], lead sulfide [95], palladium on gold coreshells[97]; beam controlled development of desired nanocrystals or nanostructures[18,105,122]; beam induced structural transition of polymeric nanomaterials[123] and metal complex heating[44,124]; dissolution of nanoparticles under high beam dose rate and high magnification[69,83]; and beam induced motion of nanoparticles including repulsion, aggregation and self-assembly of nanoparticles[37, 42,54,55,65].

The *in situ* studies of electrochemical processes include metal plating[59,67,125–129], corrosion[130], catalyst cycling[131,132], and charging and discharging of energy storage devices[19,133–135].

There is an increasing interest in *in situ* analysis of energy storage devices, especially Li ion batteries, which are the most advanced and prevailing batteries used today. The observation of materials during the charging and discharging processes at high spatial resolution is of great importance in understanding the mechanism of battery operation[13]. Such electrochemical *in situ* studies include: the degradation and stability of electrolytes [67,69]; the structural evolution of electrodes (single silicon nanowires[138,139], silicon nanoparticles[140] and SnO_2 nanowires[19]) during lithiation and delithiation; electrochemical processes at the electrode/electrolyte interface (dendrite growth and stripping [133,141]), and observation of solid electrolyte interphase (SEI) formation and evolution[137,138,141] .

There are also *in situ* studies of degradation of catalytic materials with aging. For the broadly used proton-exchange membrane fuel cells, different materials have been used as catalysts. Yu *et al*[131] observed the migration and coalescence of Pt_3Co assisted by catalyst support corrosion. Zhu *et al.* [132] studied the structural evolution of platinum iron and stabilization of the carbon support. I*n situ* studies provide insight into the slowdown of degradation of materials, such as the stabilization of catalyst support, minimization of nanoparticle movement, or reduced loading[131].

2.3.3 *In situ* Microscopy of Electrodeposition

Nucleation and growth of nanoparticles via electrodeposition is critical in determining the morphology and distribution of the deposits. Quantitative analysis of nucleation and growth is becoming a central goal in research work, as electrochemical techniques are increasingly applied in nanotechnology[60]. As discussed in Section 2.1, there are models describing the growth of electrodeposition, but there are discrepancies between the growth kinetics obtained from experimental data and the predictions of models[42,43,142,143]. Such discrepancies require modification or improvement to conventional models to develop a more quantitative control of nanostructured materials formed by electrodeposition.

Williamson *et al*[56] were the first to observe the *in situ* growth of individual copper clusters on a20 *nm* thick gold electrode from an acidic copper sulphate solution. They proved that the miniaturized liquid cell was able to mimic the electrochemical process in standard electrochemical cells. They also proved, by quantitative analysis of the change of cluster density, the deposited film thickness and analysis of cluster radius with time that the deposition fits the model of progressive nucleation and diffusion limited 3D growth. By tracking the structural evolution of individual clusters, they found that the nucleation was a homogeneous process with equivalent active sites, and the cluster growth was dependent on the diffusion of available copper ions over the cluster surface areas. Later more detailed *in situ* studies on this copper-gold system were performed by Radisic at al[58–60]. By calculating the growth rate of copper clusters, they proved that there are two growth processes occurring in parallel during the early stage of growth. The first is the reduction of copper ions onto existing clusters and the second is adsorption of ions onto the electrode surface, followed by surface diffusion and nucleation. The second process explained the differences in size and densities of the deposits obtained from *in situ* measurements and predictions from growth models. This latter point is a dominant factor for the early stage of deposition, and for long time deposition it was under linear diffusion control. By performing *in situ* deposition at various potentials, the nucleation and growth showed a gradual transition from faceted plates to circular islands due to the surface reaction mechanism.

Chen *et al*[67] performed *in situ* electrodeposition and electropolishing of nickel from aqueous nickel chloride electrolyte. Both growth and dissolution of nickel on nickel substrate were observed, based on which a new deposition mode was proposed. Nickel ions were adsorbed and nucleated on the electrode ahead of the growth front, without subsequent coarsening. This effect resulted in the formation of a thin nickel film across the surface of the electrode, while the dissolution of the film happened uniformly until a certain thickness. Beyond this thickness, de-wetting appeared, followed by coarsening, and cracking of the films. White *et al*[129] observed the electrodeposition and stripping of lead on gold electrodes under various potential waveforms in a lead nitrate solution. By relating the measured concentration of lead ions and the rate of deposition with the current transients, the dynamics involved in lead dendrite growth was studied. There are other studies of electrodeposition of gold on gold[144] and copper on gold[128,145]. The main conclusions of these studies were that the direct measurements obtained from *in situ* observation of electrodeposition provide information on the nucleation and growth rate, nucleus density, nucleation/clusters distribution, and dimension of the deposits. This information can be used to study and improve (or modify) the existing models. In combination with electrochemistry methods, important parameters such as the diffusion coefficient, and the critical nucleus size can be determined and compared with those derived from other techniques.

There is potential in using the *in situ* TEM technique in corrosion, growth of patterned substrates, deposition of metal alloys, effect of additives on growth, and liquid-crystal switching.

Conclusion

In summary, the present chapter introduced relevant background on the mechanism of nanostructure evolution during electrodeposition. To gain a fundamental understanding of the mechanistic of electrodeposition, we discussed nucleation and growth modes, introduced relevant terminologies such as *overpotential*/*underpotential*, and discussed charge transfer mechanisms (e.g., Faradaic vs. non-Faradaic process). We further reviewed the relevant mathematical models (S-H Model, S-M model, M-N Model and surface-diffusion model) to provide the background necessary to understand the experiments presented in the results chapters of the thesis. We also discussed *in situ* (S)TEM methods, focusing on the design principles, challenges, and applications to diverse fields ranging from life sciences to materials science.

Chapter 3 In-liquid Observation and Quantification of Nucleation and Growth of Gold Nanostructures Using *In situ* Transmission Electron Microscopy

Chapter Introduction (Objectives (1), (2)):

In order to study the mechanism of nanomaterial growth through electrodeposition, direct experimental proof is needed to develop a detailed understanding of the nucleation, growth and coalescence process. As mentioned in chapter 2, the *in situ* TEM system provides advanced characterization methods to perform quantitative analysis over the traditional *post situ* or other real-time high-resolution imaging techniques. The evaluation of electron beam effect and optimization of the experimental conditions are essential in separating the beam induced process from the electrochemical process. This chapter studies the beam induced and electrochemical growth processes and proposes an effective method to bring the electron beam interference down to a non-observable level (Objective (1)). Under this condition, *in situ* observation of electrodeposition of gold nanoparticles was conducted and quantitative analysis was performed and compared with physical growth models (Objective (2)). The growth rate, cluster density and the transferred charge were calculated based on the *in situ* images and compared with the results obtained from current time transients. By fitting the most widely used Scharifker-Hills model, it was found that the model only accurately describes the diffusion-limited three-dimensional multiple nucleation growth process after electrodeposition duration of 3s. It was also found that gold nanoparticles grown by electrodeposition and by electron beam exhibited obvious differences in dimension and morphology. We further demonstrated that beam induced growth can be adjusted to a negligible level by controlling the liquid layer thickness of the liquid cell. Finally the electrodeposition process was studied by the combination of *in situ* and *post situ* characterizations. The total transferred charge calculated from *post situ* SEM image shows good consistency with that calculated from *in situ* current transients. However, based on the SEM image, the distribution of the deposited gold shows an enhanced deposition along the electrode edge, which explains the discrepancy of the amount of deposits obtained from *in situ* observation and current transient measurement.

Authors: Jie Yang, Carmen M. Andrei, Gianluigi A. Botton and Leyla Soleymani

Publication: The Journal of Physical Chemistry C, 121 (13): 7435–7441

Publication Date: March 13, 2017

3.1 Abstract

In situ liquid transmission electron microscopy (TEM) is a powerful technique for observing nanoscale processes in their native liquid environment and in real time. However, the imaging electron beam can have major interference with the processes under study, altering the experimental outcome. Here, we use *in situ* liquid TEM to understand the differences between beam-induced and electrodeposition processes that result in nucleation and growth of gold crystallites. Through this study, we find that beam-induced and electrodeposition processes result in crystallites that deposit at different locations within the liquid cell and differ significantly in morphology. Furthermore, we develop a strategy based on increasing the liquid layer thickness for reducing the amount of beam-induced crystallites to negligible levels. Through this optimized system, we study the electrodeposition of gold on carbon electrodes by correlating current transients and their corresponding time-resolved scanning TEM images. This analysis demonstrates that even when the electron-beam plays a negligible role in gold deposition under optical conditions, there is a large discrepancy between the amount of deposits observed and the amount measured using the current transients. This finding sheds light on the heterogeneity of the deposition process and provides insights into designing a new class of *in situ* liquid TEM systems.

3.2 Introduction

Over the past few decades, there is increasing evidence that tuning the properties of nanostructured materials and their controllable assembly into more complex materials systems is critical for creating application-specific materials[146,147]. As a result, there is significant interest in the synthesis of structurally-tunable materials over a wide range of lengthscales (from the atomic scale to the macroscale) for applications ranging from biomedical engineering to energy. There is compelling evidence that tunability at the *nanoscale* is critical in biomedical materials systems, such as biointerfaces and biosensors, which are designed to interact with biomolecules in this lengthscale.[148,149] To address the needs of this field, among other fields relying on materials tunability at the nanoscale, much effort has been dedicated to better understanding and modelling of bottom-up nanomaterials synthesis systems.[150,151] While these studies have improved the understanding of the structural evolution of nanomaterials, they are widely based on ex-situ studies, where structural characterization follows the interruption of the synthesis process. This is especially inaccurate for processes where mass transport plays a significant role in structure growth, since it is not possible to restore the system's previous thermodynamic state when resuming the synthesis process.

In situ transmission electron microscopy in liquids is a recently developed technique, which is designed for observing the structural evolution of nanomaterials in real-time and inside their native synthesis or operating environments[56]. This technique has also been integrated with electrical circuitry to enable the in-operando study of electrochemical processes such as electrodeposition[59,67,125–129], corrosion[132], electropolishing[67], and battery charge/discharge processes[133–135]. A major challenge in these studies has been related to controlling the rate of electron beam-induced processes to reduce their interference with the processes under investigation[94]. As a result, a number of studies have solely focused on better understanding the beam-induced processes such as nucleation and growth of nanoparticles[80,95,98,103,152,153] and oxidative dissolution of nanocrystals[154], which occur as a result of the interaction between the imaging electron beam probe and the solution present in the *in situ* liquid TEM systems. Another class of studies have focused on adopting strategies such as reducing the beam dose and the concentration of reagents in solution to reduce the beam-induced effects to negligible levels[94] for observing the electrochemical processes under investigation.

Our vision here is to study the structural evolution of electrodeposited and beam-induced gold crystallites in the same system and to develop strategies for de-coupling these processes. In this study, we carefully examined the structural differences between beam-induced and electrodeposited structures created in the *in situ* liquid cell. We discovered that increasing the thickness of the imaging liquid resulted in a decrease in the amount of beam-induced crystallites present on the top electron transparent window of the system. Using this strategy, we reduced the concentration of beam-induced crystallites to negligible levels to study the nucleation and growth of electrodeposited gold crystallites. This allowed us to investigate the validity of the existing electrodeposition nucleation and growth models and perform quantitative analysis to compare the data obtained from electrochemical current transients and the corresponding *in situ* TEM images.

3.3 Experimental

3.3.1 Reagents

All chemicals were obtained in the highest available purity and used without further purification. Gold (III) chloride solution (99.99% trace metals basis, 30 wt. % in dilute HCl) was purchased from Sigma-Aldrich, Saint Louis, MO, USA. Chloroauric acid solution was made by adding Gold (III) Chloride solution ($HAuCl4$) (6.9 µL, 1 mM) in 10 mL Milli-Q water and bubbled for 20 min to remove dissolved oxygen for *in situ* electrodeposition of Gold.

3.3.2 *In situ* system

The *in situ* electrochemical liquid TEM system (Poseidon 500, Protochips Inc., Raleigh, NC, USA) used in this study was composed of a liquid cell placed at the tip of a TEM holder. The TEM holder included electrical and fluidic circuitry for interfacing the liquid cell with a potentiostat (Gamry Reference 600, Gamry Instruments Inc., Warminster, PA, USA) for electrochemical control and a syringe pump (Harvard 11 Elite standard infuse only syringe pump, Harvard Apparatus Inc., Holliston, MA, USA) for fluidic control. The liquid cell was composed of two microfabricated chips that contained electron transparent silicon nitride windows back-etched on a silicon substrate. In addition to the electron transparent windows, one, or both of the chips contained a spacer for controlling the liquid thickness, the top chip included patterned silicon nitride structures for guiding the liquid flow, and the bottom chip integrated three electrodes for creating a miniaturized electrochemical cell. The commercially available bottom chips (ECT24-CO, Protochips

Inc., Raleigh, NC, USA) used in this work integrated carbon working electrodes, platinum reference electrodes, and platinum counter electrodes on silicon/silicon nitride chips and contained 500 nm spacers. Two types of top chips with 150 nm (EPB-55F , Protochips Inc., Raleigh, NC, USA), and no spacer (EPB-55A, Protochips Inc., Raleigh, NC, USA) were also used in this study. The working electrode exposed to electrolyte has a width of 20 μm and a length of 130 μm. The imaged area is 512 x 512 pixels, where the pixel size depends on magnification. For the *in situ* bight field STEM mode imaging, the area exposed to the beam is 16.36 μm^2 at a magnification of 20 KX.

3.3.3 *In situ* electrodeposition

In situ electrodeposition of gold under the influence of electron beam was performed in a solution containing 1 mM chloroauric acid at a fixed applied potential of -0.2 V with respect to Ag/AgCl reference electrode, flow rate of 5 μL/min. Assuming a constant cross sectional area for the fluid having a width of 600 μm and a minimum thickness of 0.5 μm (imposed by the spacer dimension), we estimate the upper bound for the linear flow velocity to be 278 mm/s. The beam dose was calculated as of 21 electrons/(frame. nm^2) considering, beam current: 0.1 nA, spot size, 0.5 nm, pixel dwell time, 2 μs, frame time: 0.55 s, magnification, 20KX, pixel size, 7.9 nm X 7.9 nm. The current transients were obtained using DC chronoamperometry. The imaging was performed using a JEOL 2010FTEM) operated at 200 kV. Bright-field scanning transmission electron microscope (BF-STEM) images were acquired using a DigiScan II (Gatan, model 788) unit with a Gatan BF detector. The image time resolution was 0.555 s/frame and the series were taken every 4 seconds. For the beam off experiments, the STEM probe was blanked and the column valve was closed.

3.3.4 *Post situ* analysis

The *post situ* characterization of the deposits was performed using the JEOL 7000 field emission SEM. The chips were rinsed in DI water and air dried prior to analysis.

3.3.5 Quantification of electrodeposited gold

The amount of charge involved during electrodeposition was extracted from the acquired *in situ* STEM or *post situ* SEM images by estimating the gold crystallites as hemispheres having the projected diameters obtained from the images. The transferred charge was calculated using Faraday's law ($\mathrm{Q} = \frac{zF}{SV_m}\sum_{i=1}^{N} V_i$).

The amount of charge involved during electrodeposition was also calculated by integrating the current transient obtained by DC chronoamperometry.

3.3.6 Quantification of beam-induced gold

The amount of gold deposited through beam-induced nucleation and growth on the top silicon nitride membrane was measured by post-analysis of Figure 3.2(b). The size of each gold crystallite was measured and the total charge was calculated using Faraday's Law assuming the beam-induced crystallites to be spherical.

3.4 Results and Discussion

3.4.1 Bimodal deposition of gold nanostructures via beam-induced and electrochemical processes

We sought to use the *in situ* electrochemical liquid TEM technique to study the electrodeposition of gold due to its capability in providing current transients coupled to transmission electron microscopy images. The *in situ* electrochemical liquid TEM system used in this study was composed of a liquid cell placed at the tip of a TEM holder integrated with fluidic and electrical circuitry (details available in the experimental section). The liquid cell was composed of two microfabricated chips that contained electron transparent silicon nitride windows back-etched on a silicon substrate (Figure 3.1(a)). In addition to the electron transparent windows, one, or both of the chips contained a spacer for controlling the liquid thickness; the top chip included patterned silicon nitride structures for guiding the liquid flow; and the bottom chip integrated three electrodes for creating a miniaturized electrochemical cell.

We performed *in situ* electrodeposition experiments in a solution of $HAuCl_4$ by using chronoamperometry to apply a fixed DC potential to the working electrode for the duration of 60 s. Bright-field scanning transmission electron microscopy (BF-STEM) images demonstrate two classes of crystallites in the region that was under the direct beam exposure during electrodeposition (Figure 3.1(b)). The first class of crystallites was larger (diameter: 100nm ~200nm) and confined to the area of the carbon electrode, while the second class of crystallites was smaller (diameter <100nm) and spread across the entire field of view. The two classes of crystallites are positioned in different planes of focus indicating that the smaller crystallites (in focus) are confined to the silicon nitride window of the top chip and the larger crystallites are confined to the carbon electrode of the bottom chip. In the area that was not irradiated during electrodeposition and underwent a shorter imaging exposure (~ 9 s), we observed a single class of crystallites, which were confined to the surface of the carbon electrode with a higher density of particles at the electrode edge (Figure 3.1(c)). The increase in particle density at the electrode edge is in line with previous ex-situ reports[155] and will be discussed in more details in the following section.

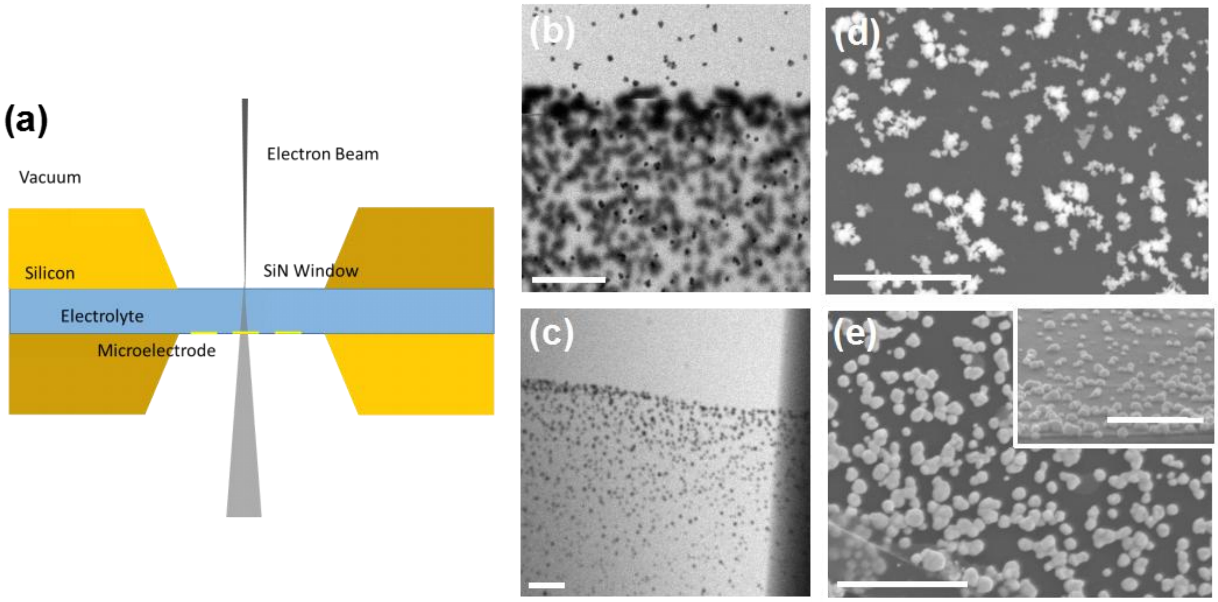

Figure 3.1. *In situ* electrodeposition of gold on a carbon electrode. (a) Schematic drawing of the liquid cell with the holder inserted inside the microscope. Both chips contain a silicon nitride membrane, and the bottom chip contains a three-electrode (working, reference counter) electrochemistry setup. (b) *In situ* BF-STEM image of two classes of crystallites confined onto the two chips under direct electron beam exposure (c) *In situ* BF-STEM image of Au deposited on carbon electrode outside of the area irradiated during electrodeposition. (d) *Post situ* SEM image of Au crystallites formed on the membrane of the top chip in a region under direct beam exposure. Scale bar: 0.4 µm. (e) *Post situ* SEM image of Au deposited on carbon electrode on the bottom chip. The inset represents the tilted SEM image of the structures shown in (e). The *in situ*

experiments were performed under an electron beam current of 0.1 nA, a beam dose of 21 electrons/frame nm^2 and a flow rate is 5 μL/min. Scale bar: 1 μm.

The deposition on both chips was further investigated by taking scanning electron microscopy (SEM) images following the *in situ* experiment (Figure 3.1 (d)-(e)). It is evident from these images that the crystallites deposited on the bottom and top chips differ significantly in morphology. The crystallites confined to the carbon electrode of the bottom chip have a circular 2D projection (Figure 3.1(e)), and a 3D hemispherical shape (Figure 3.1(e)-inset). This hemispherical morphology is in line with structures deposited under a mixed kinetics/diffusion control, where both mass transport and surface reactions play a critical role in establishing the deposition rates [156]. The gold crystallites deposited on the top window were confined to the area irradiated during electrodeposition, and demonstrated an acicular morphology, which is characteristic of diffusion-limited aggregation. Such structures have been previously demonstrated under electron beam-induced nucleation and growth conditions[103,153]. The localized nature of the electron-beam induced particles in the area exposed to the electron beam is expected due to the short lifetime (10^{-9} s) of the beam-induced hydrated electrons. The observation that the beam-induced crystallites were present on the *top* silicon nitride window of the irradiated area can be explained by considering two different possibilities. In the first case, gold ions are reduced locally at the silicon nitride windows due to the presence of an increased concentration of secondary electrons and the resulting hydrated electrons. Since the electron beam experiences broadening as it passes through the liquid sample, there will be a larger local surface density of secondary electrons at the top silicon nitride window compared to the bottom window, making it possible to achieve the supersaturation required for forming visible crystallites on the top window. Another possibility is that gold particles are nucleated away from the surface and in the bulk solution and driven to the top silicon nitride window by electrostatic forces. The electrostatic forces can be induced by the differences in the charge density between the top and bottom chips. These differences can be due to the (1) presence of electrical circuitry on the bottom chip, (2) increased primary electron density on the top chip, and (3) increased secondary electron density on the top chip. Given that we observe a similar behavior on non-biased chips and in areas that do not contain the electrical circuitry (Supplementary Figure 3.1), we suspect points (2) and (3) to be the most probable explanations for the observed behavior. This would require for the gold particles to contain some surface charge. The surface charge and the related zeta potential of the beam-induced nanoparticles depend on the balance between the charges induced on the objects by the electron beam, concentration of ionic species (for e.g. $[AuCl_4]^-$ in the electrodeposition bath, and solution pH. [157,158] The starting pH of the electrodeposition solution was in the acidic range (~3) , and previous studies have demonstrated that the effect of radiolysis products on the solution pH is negligible for this starting pH[90,157]. The reported observation that zeta potential becomes more positive in acidic solutions[30] is consistent with our findings that the beam-induced gold nanoparticles accumulate on the top silicon nitride membrane having a larger surface density of primary and secondary electrons compared to the bottom membrane.

In addition to the differences in morphology, the two structures were deposited at different amounts on the top and bottom surfaces, with the growth on the lower chip (on the electrode) demonstrating a considerably larger amount (~ two orders-of-magnitude) of gold crystallites. We calculated the amount of charge transferred during deposition on each chip by: (1) measuring the size of the deposited structures, (2) calculating their volume by assuming spherical structures on the top chip and hemispherical structures on the bottom chip, and (3) using Faraday's law (Equation 1) to determine the amount of charge transferred in the deposition of the crystallites on each surface. This calculation demonstrated that the reduction process under the abovementioned experimental conditions (beam dose, applied potential and bath composition) is dominated by electrodeposition ($1.55\text{x}10^{-6}$ C) compared to beam-induced nucleation and growth ($3.58\text{x}10^{-8}$ C). The slower average deposition rate of beam-induced particle can be partly explained by the presence of an induction time before Au(III) can be reduced to Au(0)[103].

3.4.2 Single mode *in situ* electrodeposition of gold on carbon electrodes

Although electron beam-induced nucleation and growth contributes to an average gold ion reduction rate that is about two orders of magnitude lower compared to electrodeposition, accurate study of electrodeposition processes requires the contribution of beam-induced processes to be further minimized. Here, we sought to achieve this by increasing the liquid layer thickness of the cell by increasing the spacer thickness and choosing a liquid cell region that experienced larger bulging. This has allowed us to increase the liquid layer thickness from about 550 nm in the experiments shown in Figure

3.1 to about 800 nm in the experiments demonstrated below as measured by electron energy loss spectroscopy (data not shown).

In situ deposition of gold on carbon was performed again under the same beam (beam dose of 21 electrons/frame.nm^2, current of 0.1 nA) and electrodeposition conditions. The current transient obtained during the *in situ* electrodeposition is shown in Figure 3.2(a) and the series of corresponding *in situ* images, acquired every 4 s is displayed in Figure 3.2(b). It is evident from the images that increasing the liquid thickness has reduced the beam-induced processes to negligible levels to a point where there are no *observable* beam-induced crystallites. Previous studies have demonstrated that even in the absence of beam-induced crystallites, electrodeposition processes, under specific bath and electron beam conditions, can be influenced by the electron beam.[125] To investigate this possible effect under our experimental conditions, we performed electrodeposition experiments inside the *in situ* liquid cell with and without electron beam exposure (Figure 3.2 (a)-inset). The chronocoulometry curves obtained for the two cases demonstrate insignificant differences between the electrodeposition processes with and without electron beam exposure, and further confirms the reduction of electron beam processes to negligible levels. The observation that beam-induced crystallites were no longer present on the top silicon nitride window when a thicker liquid sample was imaged can be explained by considering the two different possibilities discussed above for justifying the accumulation of gold crystallites on the top window: local supersaturation at the top window due to the high concentration of secondary electrons, or transport of the solution-borne nuclei to the top surface due to electrostatic forces. While the secondary electron argument should not vary with liquid thickness, the second possibility is more likely to be thickness related. If we assume the gold crystallites are nucleated in the solution first and transported to the top window by electrostatic forces, increasing the liquid thickness will have consequences on the generation of gold crystallites in solution and their transport. Regarding generation, previous theoretical studies indicated that the concentration of hydrated electrons reduces abruptly outside the solution volume exposed to the electron beam.[90] If we compare the beam broadening occurring in 550 nm and 800 nm solution thicknesses using Monte Carlo simulations[159], we observe that a 1 nm probe broadens to 6 nm and 18 nm in thinner and thicker solutions respectively. This means that the volume concentration of primary electrons and the resultant hydrated electrons could be significantly reduced in thicker solutions. This indicates that it would be more difficult to reach the threshold concentration needed for homogenous nucleation of gold nanoparticles in the thicker solution. Another possibility has to do with the transport of the generated particles in the presence of fluidic flow. In thicker liquids, the transverse electric-field between the two windows may not be strong enough to transport the nuclei to the window, and these nuclei are removed by the fluidic flow to the non-irradiated region of the sample before they can grow to observable sizes.

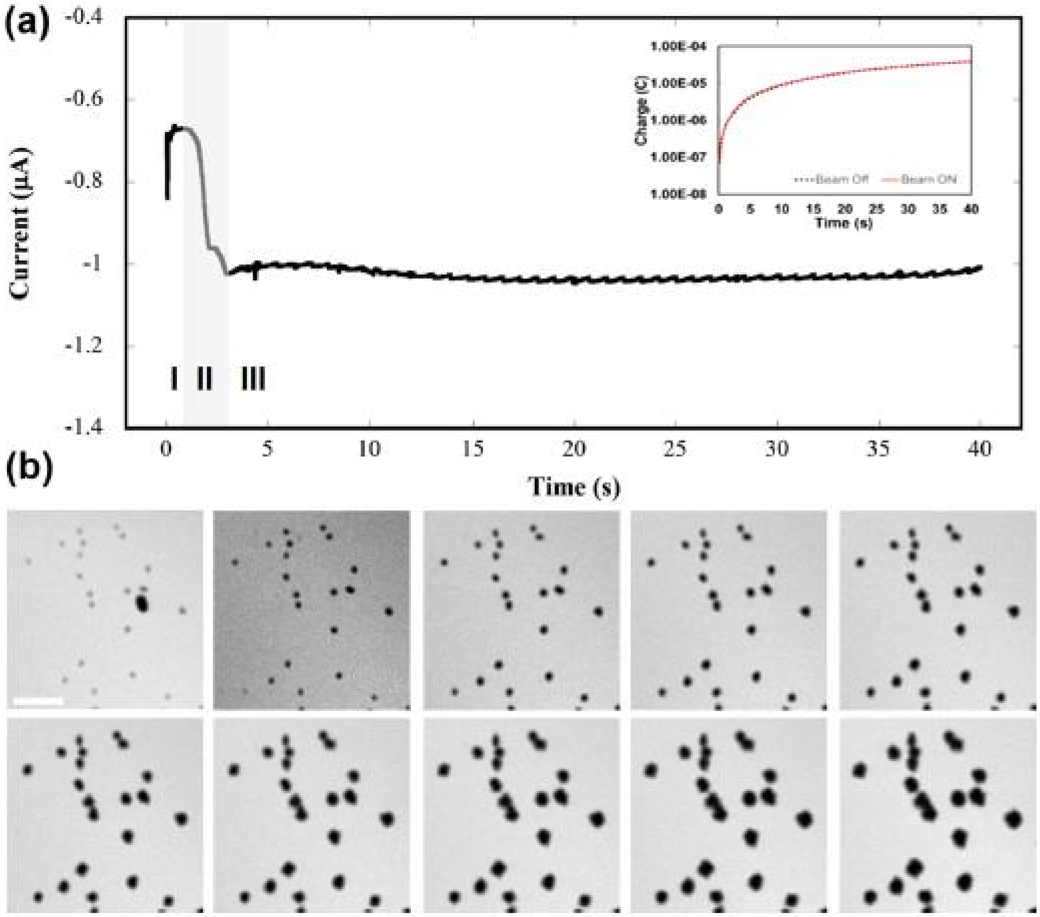

Figure 3.2. *In situ* electrodeposition of Au on a carbon working electrode in 1 mM $HAuCl_4$. (a) Current transient acquired from the *in situ* deposition under a fixed potential of -0.2 V (vs. Ag/AgCl reference electrode). In the inset are shown the chronocoulometry curves with and without the beam. (b) Series of BF-STEM images corresponding to the current transient curve in (a) acquired at every four second, starting at 2 s after the potential was applied. The electron beam dose is 21 electrons/frame.nm^2 and the flow rate is 5 μL/min. The scale bar represents 1 μm.

Three different regimes are evident from the current transient of Figure 3.1(a): initially, there is a decrease in the current magnitude (regime I, < 1 s), which is followed by a current increase (regime II, ~1-3 s) and a current plateau (regime III, > 3 s). These three different regimes have been previously observed in standard electrodeposition experiments and are attributed to the adsorption of ionic species on the electrode surface

(I), nucleation and growth (II), and growth stages (III) respectively[160]. Regime II demonstrates a current rise, which indicates a rapid increase in the electroactive area as new nuclei are created and the existing ones grow[161]. The plateau in regime III is indicative of a condition where the depletion zones surrounding the nuclei begin to overlap, reducing the diffusive flux as hemispherical diffusion is replaced by linear diffusion. Although the radial transport of depositing specifies to the nuclei is hindered in this regime, growth continues due to the mass transfer of species that reach the electrode vertically due to semi-infinite linear diffusion. [162]

Performing electrodeposition experiments *in situ* enables the comparison of current transients with images taken at the corresponding time points. All *in situ* images taken during the electrodeposition experiment, with the first one taken 2 s after the start of electrodeposition and the last one taken 38 s after the start of electrodeposition, demonstrate a fixed number of crystallites. However, all crystallites demonstrate a steady growth during the electrodeposition period (Figure S3.4). The fixed number of nuclei observed here is in line with previous ex-situ experiments, and is the result of (1) exhausting the number of nucleation sites available at the specific *overpotential* and/or (2) the attenuation of the *overpotential* at the equipotential surface of the substrate and crystallites caused by analyte depletion.[161] It was not possible to capture images within the first 2 s of the electrodeposition experiment due to technical and software limitations of our imaging system.

In order to determine the validity of the widely-used Scharifker-Hill (SH)[162] model to the data obtained here, we performed the following analysis. First, we plotted the cluster radius versus time in a log-log scale (Figure S3.4), and determined the slope of these curves for each particle extracted from the *in situ* STEM images of Figure 3.2(b) (Figure S3.5). Given that the SH model assumes that each nucleus grows independently, we divided the data between particles that overlapped during the course of the experiment, and those that grew independently. If we look at non-overlapping particles, we observe a slope of 0.406±0.047 (Figure S3.5), which is lower than the slope of 0.506±0.049 expected for diffusion-limited growth. However, if we looked at longer times (> 14 s), where the current transient reaches steady state, we observe a slope of 0.5 (Figure S3.5). This indicates that diffusion-limited growth dominates at longer times, whereas other processes such as adsorption could be responsible for the reduction of slope in early deposition times. This also implies that the fluidic flow at the current flow velocity does not significantly enhance mass transport to the electrode surface. This is expected as flow in microfluidic systems is often effective in replenishing the bulk concentration, but is ineffective in replenishing the solution near channel walls.[163] Second, we calculated the nucleation density using the *in situ* STEM images and compared those with the values obtained from the SH model (see supplementary information). The nucleation density from the images was calculated to be $1.15 \times 10^8\ cm^{-2}$, which is in very good agreement with the value ($6.93 \times 10^7\ cm^{-2}$) obtained from the SH model. A different result was obtained when performing *in situ* electrodeposition of copper, where the images resulted in a nucleation density that was 3 orders of magnitude larger than the results from the SH model.[60] This could be due to the differences in the depositing species, for example, adsorption and two dimensional diffusion could play a significant role in copper electrodeposition in contrast to gold. This could also be due to the heterogeneity of electrodeposition throughout the working electrode. Lastly, we fit the data of Figure 3.2 (a) to the analytical models for progressive and instantaneous models developed by Scharifker and Hill.[162] These results (Figure S3.7), demonstrate that at longer times ($t/t_{max} > 1$), our results, fit the instantaneous S-H model; however at earlier times, they fit the progressive S-H model. This indicates that the S-H model, based on three dimensional multiple nucleation with diffusion-limited growth, accurately describes the particle growth at longer diffusion times, while it might be less accurate at shorter times.

In order to further compare the growth kinetics derived from the current transients and the *in situ* STEM images, we used the radii measured from the images at each time point along with the Faraday's law (Equation 1) to estimate the amount of charge transferred during the electrodeposition process. According to Faraday's law, the total charge Q transferred for the formation of N hemispherical islands is [59]:

$$Q = \frac{zF}{SV_m} \sum_{i=1}^{N} V_i \qquad (1)$$

where z is the charge of the ion participating in the electrodeposition process, F is Faraday's constant, V_m is the molar volume of gold, S is the area of the STEM image by excluding the area of the frame that included incomplete images of crystallites, and $V_i = \frac{1}{2} \times \frac{4}{3} \pi R^3$ is volume of one hemispherical island in STEM image. For this analysis, we assumed the crystallites were hemispherical having a radius extracted from *in situ* images. Figure 3.3 demonstrates the charge transferred during the electrodeposition process as extracted from current transients and *in situ* images. Although we expected the two curves to be very similar, it is evident that the transferred charge calculated from the current transient has a value (-4.04×10^{-5} C) that is an order of magnitude (~26 times) higher than the charge derived from the *in situ* images (-1.54×10^{-6} C). However, it should be noted that the two curves display the same trend if they are expressed in a normalized manner (Figure 3.3), demonstrating that the two curves and the two analysis modes (imaging and current transients) agree on predicting the electrodeposition rates and mechanism. The large deviation between the transferred charge derived from the two analysis modes can be explained by observing the low-magnification SEM image of the carbon electrode after the electrodeposition experiment (Figure 3.3-inset). This image demonstrates a large variation between the particle density and size between central and edge regions of the carbon electrode. As a result, the images taken at the central region of the electrode (Figure 3.2(b)) underestimates the volume of the electrodeposited gold compared to current transients, which are not localized to a specific electrode region. To validate this hypothesis, we used the low magnification SEM image of the electrode after electrodeposition (Figure 3.3-inset) to estimate the volume of the electrodeposit and the charge transferred during the process. Using this method, we calculated the charge transferred to be -4.31×10^{-5} C, which is in excellent agreement with the value obtained from the current transients. The increased electrodeposition rate at working electrode edges have been previously reported and studied. Enhanced mass transport rates and enhanced local electric fields at the electrode tips and contours have been identified as the source of these increased rates [155]. Given the low concentration (1 mM) of ions in the solution and the previous models of electric field distribution for *in situ* electrochemical systems demonstrating enhanced electric field at the regions with larger electrodeposition rates[164], we suspect both of these mechanisms to be important for the observed edge-enhanced electrodeposition rates. In order to obtain imaging results that can be directly compared with current transients, patterned electrodes with conductive regions having a similar size to the field of view would be useful in future *in situ* experiments.

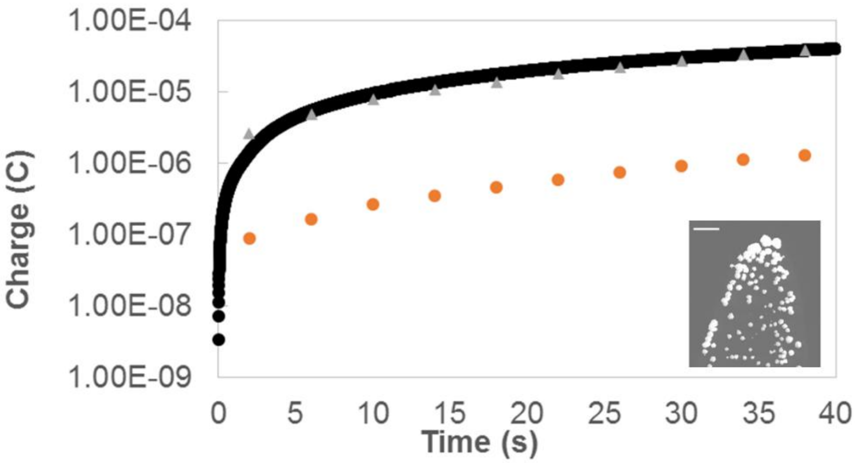

Figure 3.3. The total charge transferred during the *in situ* electrodeposition shown in Figure 3.2. The black line represents the integrated charge versus time obtained from Figure 3.2(a), the circles represents the amount of charge calculated according to equation 1 based on the radius of structures measured from each image in Figure 3.2(b). The triangles represent the same data points as the circles, normalized to the highest value of the black curve for comparison purposes (see text for details). The inset presents the SEM image after the electrodeposition experiment showing the distribution of gold structure on the carbon electrode. Scale bar represents 2 μm.

3.5 Conclusions

In this paper, we demonstrated *in situ* synthesis of gold nanostructures in liquid using two processes: beam-induced nucleation and growth and electrodeposition. The electrodeposited and beam-induced crystallites demonstrated very different morphologies. Under the experimental conditions used here, we observed that beam-induced processes resulted in structures having the morphology of diffusion-limited aggregates, while the electrodeposition process resulted in structures exhibiting mixed kinetics/diffusion regime. We further showed that increasing the liquid layer thickness decreased the appearance of beam-induced processes to negligible levels. Using this optimized system, we were able to observe the current transients and the corresponding growth of gold crystallites. While the growth curves obtained from current transients and *in situ* TEM images exhibited similar trends, the imaging results showed gold deposition amounts that were more than one order-of-magnitude lower compared to current transient results. This discrepancy results from the heterogeneity in electrodeposition rates, with slower deposition at the central imaging area compared to the electrode edges. More precise experiments are planned using chips that enable spatial confinement of electrodeposition to the imaging area.

3.6 Acknowledgements

We acknowledge financial support from NSERC. The electron microscopy was carried out at the Canadian Centre for Electron Microscopy (CCEM), a national facility supported by the Canada Foundation for Innovation under the MSI program, NSERC and McMaster University. We also acknowledge Dr. Glynis de Silveira, Dr. Andreas Korinek, and Andy Duft for assistance with experimental establishment and discussions regarding image analysis.

3.7 Supplementary Information

In Liquid Observation and Quantification of Nucleation and Growth of Gold

Nanostructures Using In Situ Transmission Electron Microscopy

Jie Yang,[1] Carmen M. Andrei,[2] Gianluigi A. Botton* [2,3] and Leyla Soleymani* [1,4]

1. School of Biomedical Engineering, McMaster University, Hamilton, Ontario L8S 4K1, Canada
2. Canadian Centre for Electron Microscopy, McMaster University, Hamilton, Ontario L8S 4M1, Canada
3. Department of Materials Science and Engineering, McMaster University, Hamilton, Ontario L8S 4K1, Canada
4. Department of Engineering Physics, McMaster University, Hamilton, Ontario L8S 4K1, Canada

1. Effect of electron beam on *in situ* electrodeposition

The control experiment was conducted by exposing the in situ electrochemical cell containing the gold plating solution with an electron beam dose of 21 electrons/frame.nm2, keeping all the conditions the same as the in situ deposition experiment displayed in Figure 3.1(b), except that no electrochemical signal was applied. The bright-field images were captured at 30 s, 60 s and 120 s. The dark area represents the edges of silicon nitride window.

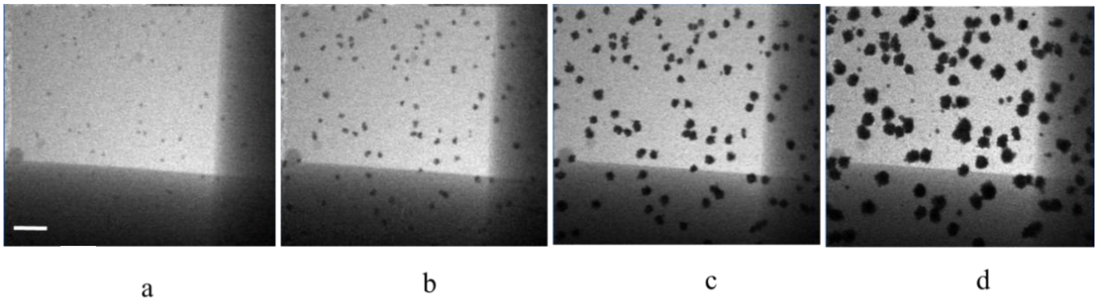

Figure S3.1. *In situ* electron beam-induced gold crystallite growth under beam dose of 21 electrons/(frame.nm2), without applied potential imaged (a) immediately after the beam was turned on, and after (b) 30 s, (c) 60 s, and 120 s of taking the first image. The scale bar represents 0.5 μm.

2. Analysis of the growth process of gold clusters

For the time-resolved images displayed in Figure 3.2 of the main text, the cluster size, cluster volume, and the total charge transferred were determined for every time point as follows. The projected circles representing the electrodeposited gold clusters were extracted and labeled for each time resolved image as demonstrated in Figure S3.2. The cluster radius was calculated as the radius of a circle having the same area as the projected cluster. The clusters were assumed to be hemispherical, and their volume was calculated as . $V = \frac{2}{3}\pi r^3$.

Figure S3.3 shows the volume versus electrodeposition time for the 21 clusters labeled in figure S3.2, plotted in log scale. Figure S3.4 shows the radius versus electrodeposition time for the 21 clusters labelled in Figure S3.2 in log-log scale. Figure S3.5 summarizes the slope of the curves displayed in Figure S3.4, excluding the first data point at t=2s. The first data point was excluded in calculating the slope, since the cluster had not entered the diffusion-limited nucleation and growth regimes (regimes II and III in Figure 3.2(a)) during the first 2 s of deposition, and adsorption was an important consideration in this regime (regime I).

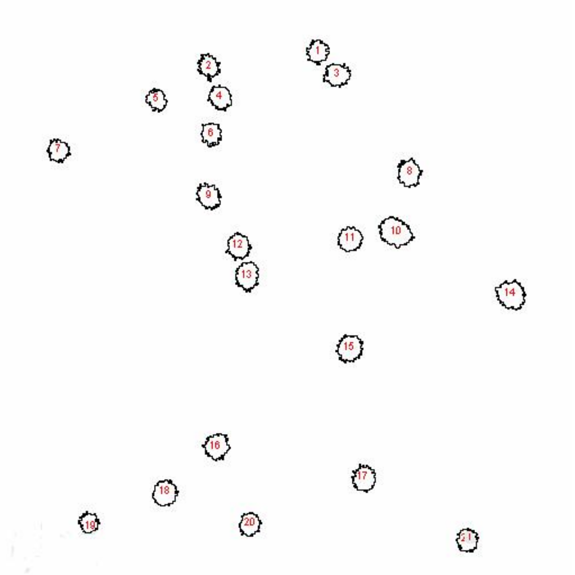

Figure S3.2. Clusters identified and extracted from one of the *in situ* STEM images during *in situ* electrodeposition of Au on carbon

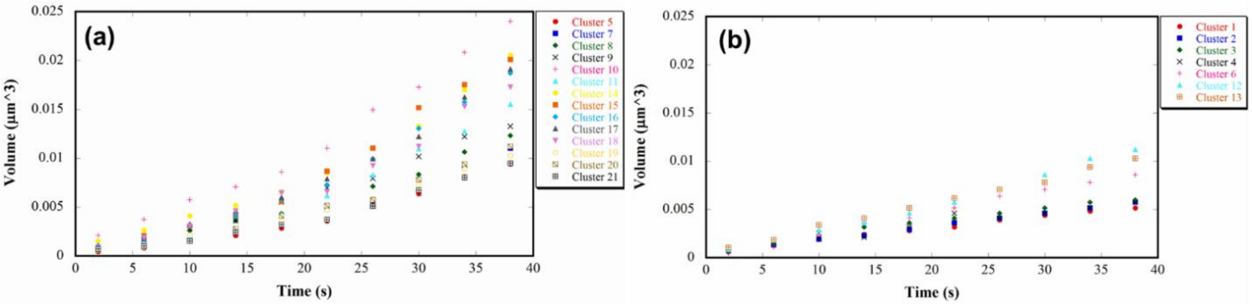

Figure S3.3. Cluster volume versus time extracted from the time-resolved in situ STEM images demonstrating clusters that (a) do not overlap or (b) overlap at some point during the deposition.

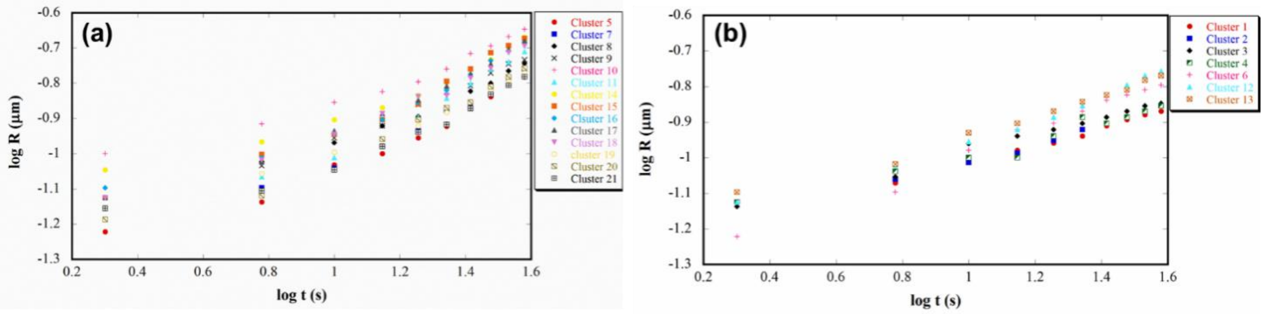

Figure S3.4. Cluster radius versus time in a log-log graph demonstrating clusters that (a) do not overlap or (b) overlap at some point during the deposition.

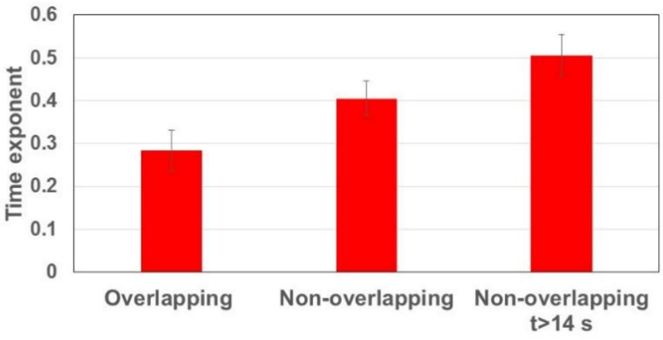

Figure S3.5. The average time exponent of the overlapping and non-overlapping clusters extracted from the slope of the log (r) versus log (t) curves presented in Figure S3.4 for 2 s to 38 s, or for times longer than 14s. The error bars represent standard deviation.

3. Calculation of total charge transferred during *in situ* deposition by *post situ* SEM

images

In order to further compare the total charge transferred during the *in situ* deposition with the calculated charge from current transient, amount of charge transferred was calculated based on the *post situ* SEM image shown in Figure 3.3--inset of the main text. According to Faraday's law, the total charge Q transferred for the formation of N hemispherical islands is [59]:

$$Q = \frac{zF}{SV_m}\sum_{i=1}^{N} V_i$$

where z is the charge of the ion participating in the electrodeposition process, F is Faraday's constant, V_m is the molar volume of gold, S is the area of the STEM image by excluding the area of the frame that included incomplete images of crystallites, and $V_i = \frac{1}{2} \times 4/3\ \pi R^3$ is volume of one hemispherical island in STEM image.

Figure S3.5 summarizes the cluster diameters extracted from the SEM image.

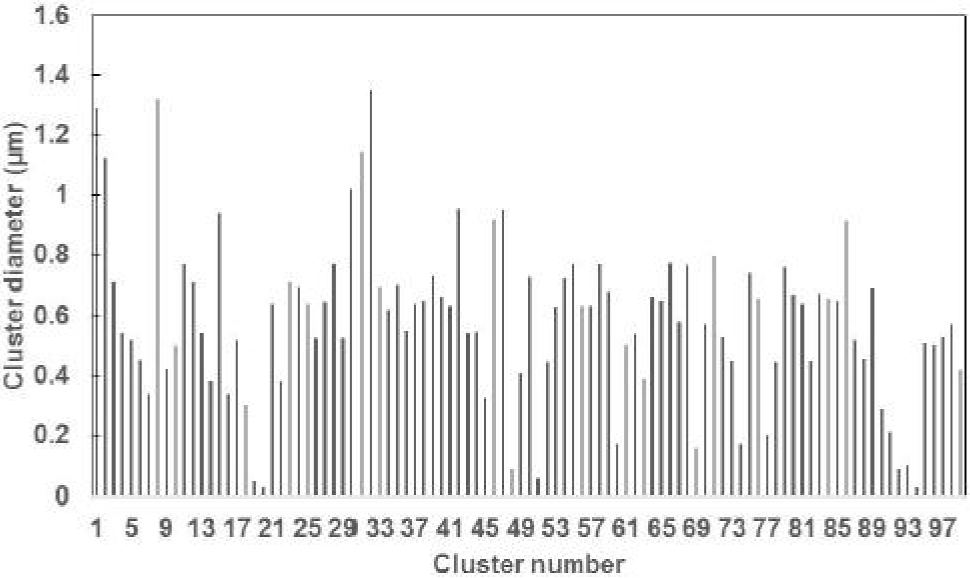

Figure S3.6. The diameter of clusters as extracted from the SEM image in Figure 3.3-inset of the main text.

4. Fitting to existing nucleation and growth model

The early stage of in-situ current transient was fitted into two instantaneous and progressive nucleation and growth models by Scharifker and Hill[162] (S-H model) as shown in figure S3.7. The maximum current i_{max} and the corresponding time t_{max} were extracted from the curve in Figure 2 of the main text, and was plotted in i/i_{max} vs t/t_{max}.

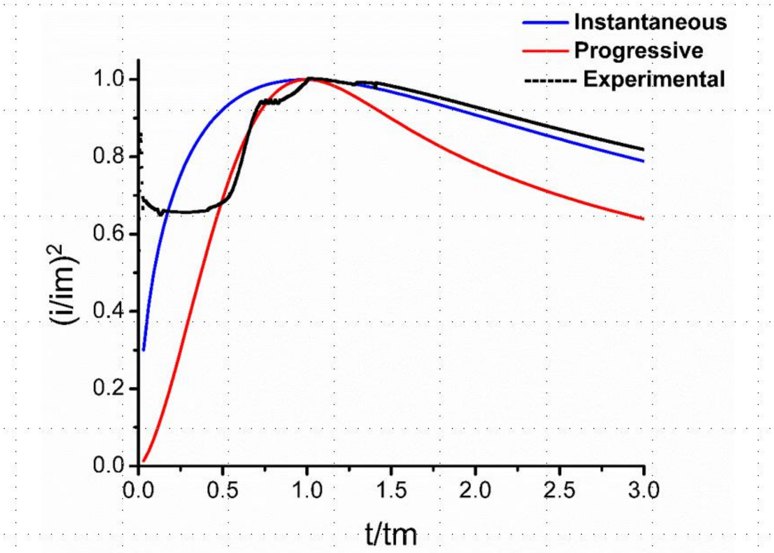

Figure S3.7. Experimental data (black) fitted to the instantaneous (blue) and progressive (red) S-H models.

5. Calculation of the nucleation density

Based on the in-situ STEM images presented in Figure 2(a), the nucleation density is constant and is equal to $N(t) = N_0 = 1.15 \times 10^8\ cm^{-2}$.

According to S-H model, and assuming instantaneous nucleation:

$k = (8\pi c V_m)^{1/2} = 0.01602$,

Where c is the bulk concentration of the depositing species (1 x 10^{-6}mol/ cm^3), and Vm is the molar volume of the depositing materials (10.21 cm^3/mol for gold)

$$N = \frac{1.2564}{\pi D k t_{max}} = 6.93 \times 10^{7}\ cm^{-2},$$

Where D is the diffusion coefficient of gold ions in water (1.2 x10 $^{-7}$ cm^2/s), and t_{max} is 3 s.

Chapter 4 *In situ* study of the role of electrolyte on palladium nucleation and growth in an electrochemical cell using liquid transmission electron microscopy

Chapter Introduction (Objectives (1), (2) and (3))

Palladium nanoparticles are widely used as substrates for biosensors and catalyst for fuel cells. It has been reported that palladium nanostructured materials with different morphologies demonstrate significantly different sensitivity when they are applied in bio-sensing. Moreover, structures with various morphologies can be grown through electrodeposition by varying the concentration of the supporting electrolyte and the type and magnitude of the applied electrical stimulus. There is great interest in being able to understand the effect of these parameters on the morphological evolution of nanostructures and to use this understanding to create specific structures. This chapter focuses on analyzing the effect of supporting electrolyte on palladium structural formation and applying proper growth models to describe the growth process (objective (2) and (3)). As discussed in chapter 2 and chapter 3, during in situ observation, the electron beam plays an important role in the formation of nanostructures. This chapter studies the electron beam induced growth and electrochemical deposition process and de-couples the beam effect from the electrodeposition process using *in situ* TEM and *post situ* SEM imaging (objective (1)). Furthermore, the growth mechanism in palladium salt solution with and without HCl as supporting electrolyte were studied separately. Different growth models were used to describe the growth process and a new growth mode which considers self-limiting growth, surface diffusion and coalescence/aggregation on low energy surfaces was found to provide valid explanation of deposition in solution with and without HCl. It was found that the morphology of the deposited palladium was greatly affected by adding the supporting electrolyte. Aggregations of palladium clusters with aspherical morphology formed in the electrodeposition solution with HCl, compared with the palladium particles with a circular projection from solution without HCl. Moreover, the role of HCl in electron beam-induced growth process that occur in parallel with electrodeposition process was investigated. It was found that HCl reduced beam-induced nucleation and growth processes on the non-conductive silicon nitride substrate by creating a more oxidative environment in the liquid electrochemical cell.

Authors: Jie Yang, Carmen M. Andrei, Yuting Chan, B. Layla Mehdi, Nigel D. Browning, Leyla Soleymani and Gianluigi A. Botton

4.1 Abstract

Electrodeposition is widely used for fabricating tunable nanostructured materials in applications ranging from biosensing to energy conversion. A model based on 3D island growth is widely accepted in explaining the initial stages of nucleation and growth in electrodeposition. However, there are regions in the electrodeposition parameter space where this model becomes inapplicable. We use liquid cell transmission electron microscopy along with post-situ scanning and transmission electron microscopy to investigate electrodeposition in this parameter space, and to shed light on the early-stage nucleation and growth of palladium. Using a collection of electron microscopy images and current time transients recorded during electrodeposition, we discover that electrochemical aggregative growth, rather than 3D island growth, best describes the electrodeposition process. We then use this model to explain the change in morphology of palladium electrodeposits from spherical to open clusters with non-spherical morphology when HCl is added to the electrolyte solution. The enhanced understanding of the early stages of palladium nucleation and growth and the role of electrolyte in this process provides a systematic route towards the electrochemical fabrication of nanostructured materials.

4.2 Introduction

Electrodeposition is a versatile method for fabricating coatings on conductive substrates. While traditionally this method has been used for creating aesthetic and/or anti-corrosion coatings in various manufacturing sectors, recently, there has been a rising interest in using electrodeposition for creating structures that are tunable over multiple length scales.

The ability to create tunable nano and microscale structures and assemble them into three dimensional hierarchical architectures has proven to be critical in tuning the mechanical[164,165], electronic/electrochemical[2,166,167], optical[160,168,169], and surface properties[7] of materials. Consequently, simulations and experimental studies are being intensely performed in order to design structures that have ideal morphologies and length scales for use in applications ranging from tissue engineering to energy conversion. Manufacturing such structures containing micro and/or nanoscale components is often achieved using top-down or bottom-up processes, or their combination. Among these, electrodeposition is ideally suited for the large volume and low-cost fabrication of structures with simple (nanowires[172], nanosheets[173], hemispheres[174]) and complex (dendritic[175,176], fractal[177], acicular[178], globular assemblies[179]) architectures.

Due to its nobility, catalytic activity, and hydrogen reactivity, palladium is heavily investigated for use in emerging devices such as biosensors[2,180], biofuel cells[181], and hydrogen fuel cells[3,182]. Overpotential electrodeposition – deposition at potentials more negative than the equilibrium potential – of palladium is an effective strategy for developing 3D structures with tunable morphologies suitable for the abovementioned applications.[183] Structural tunability is achieved by varying the applied potential/current waveform and the composition of the electrodeposition bath. Hydrochloric acid (HCl) is used as an electrolyte for tuning the structure of various materials (platinum[184], palladium[185], copper[186,187], zinc oxide[188], nickel[189], etc.) in electrodeposition. The role of HCl in structural differentiation of metallic electrodeposits is attributed to the preferential adsorption of chloride on specific crystalline planes during deposition[190,191], the influence of bath pH on the equilibrium concentration of metallic ions in the solution[192], and the impact of HCl concentration on the overall deposition rate[193]. In spite of existing studies on HCl-mediated *structural differentiation*, there is a need for additional studies on *structural evolution* of these electrodeposits to better understand how HCl contributes to structural differentiation. In order to focus on structural evolution, we used liquid cell transmission electron microscopy (TEM) to study the electrodeposition of palladium *in-operando* and in its native environment.

Liquid cell TEM has been used for studying the electrodeposition of copper[58–60,101,125,126], gold[101,127], and lead[129]. However, many of these studies are focused on correlating the *in situ* images and the measured current time transients to the traditional electrodeposition models based on Volmer-Weber 3D island growth[162]. More recently, a generalized electrochemical aggregative growth mechanism has been proposed for the overpotential electrodeposition of platinum, palladium, and silver, which considers self-limited nanocluster growth, nanocluster surface diffusion, and coalescence as the processes involved in structural differentiation of electrodeposits[26,27,47]. Here we develop an integrated approach combining liquid cell TEM, *post-situ* TEM, *post-situ* scanning electron microscopy (SEM), and electrochemical analysis to study the overpotential deposition of palladium under conditions where the traditional nucleation and growth models are not applicable. This approach allows us to explain the mechanistic role of HCl in structural differentiation in the context of the aggregative electrodeposition growth model.

4.3 Experimental

4.3.1 Reagents

All chemicals were obtained in the highest available purity and used without further purification. Palladium (II) chloride powder (≥99.9%) and Hydrochloric acid (ACS reagent, 37%) was purchased from Sigma-Aldrich, Saint Louis, MO, USA. 0.1 M Hydrogenchloropalladate (H_2PdCl_4) stock solution with was made by mixing 177.33 mg palladium chloride powder and 2 mL 1M HCl into 7.956 mL Milli-Q water, dissolved as a clear brown solution after two-hour sonication. Palladium solutions were bubbled by nitrogen gas for 20 min to remove dissolved oxygen before in situ electrodeposition.

4.3.2 *In situ* system

The *in situ* electrochemical liquid TEM system (Poseidon 500, Protochips Inc., Raleigh, NC, USA) used in this study was composed of a liquid cell at the tip of a TEM holder. The TEM holder included electrical and fluidic circuitry for interfacing the liquid cell with a potentiostat (Gamry Reference 600, Gamry Instruments Inc., Warminster, PA, USA) for electrochemical control and a syringe pump (Harvard 11 Elite standard infuse only syringe pump, Harvard Apparatus Inc., Holliston, MA, USA) for fluidic control. Two microfabricated chips with 50 nm silicon nitride membranes were sealed inside the liquid cell and in situ imaging was performed by electrons passing through the overlapped membranes. Electrolyte was flown in between and the thickness of the electrolyte was determined mainly by the spacers on both chips plus bulging under vacuum, one of the chips was integrated with three electrodes as a miniaturized electrochemical cell. The commercially available bottom large chip (ECT24-CO, Protochips Inc., Raleigh, NC, USA) was used as a miniaturized electrochemical cell with carbon working electrode on SiN membrane, Pt reference electrode, and Pt counter electrode and had 500 nm spacers, and the top chip only contained SiN windows (EPB-52DF, Protochips Inc., Raleigh, NC, USA) with 150 nm spacers.

4.3.3 *In situ* and *ex situ* Chronoamperometry

In situ chronoamperometry was performed in 5 mM H_2PdCl_4 with 0.015 M HCl and without HCl with solution flow rate of 5 μL/min. The current transients were obtained using the Gamry potentiostat. Real-time imaging was performed using a JEOL 2010FTEM operated at 200 kV. Bright-filed scanning transmission electron microscope (BF-STEM) mode was performed under a beam dose of 21 electrons/frame. nm^2. In situ images were acquired using a DigiScan II (Gatan, model 788) unit with a Gatan BF detector with time resolution of 0.555 s/frame. The whole *in situ* process was recorded frame by frame directly as a video and *in situ* images were extracted from the *in situ* videos.

4.3.4 Simulation and particle analysis

Simulation on electric field distribution was conducted using COMSOL Multiphysics 4.3b (COSMOL Inc., Stockholm, Sweden). Measurement on the diameter and size distribution of palladium particles was performed using ImageJ.

4.3.5 *Post situ* analysis

The *post situ* characterization of the structures grown on the carbon microelectrode was performed using the JEOL 7000 field emission SEM. The chips were rinsed in DI water and air dried prior to analysis.

4.4 Results and discussion

The *in situ* study of palladium electrodeposition was performed using chronoamperometry, where a fixed DC potential was applied to the working electrode inside a LEC-TEM setup. As shown in Figure 4.1, the system contained a miniaturized electrochemistry cell at the tip of a TEM holder, and was integrated with microfluidic and electrical circuitry. Using the microfluidic system, the electrolyte was flown between two silicon nitride membranes, which permitted observation of the electrochemical reactions on the working electrode in *real-time*.

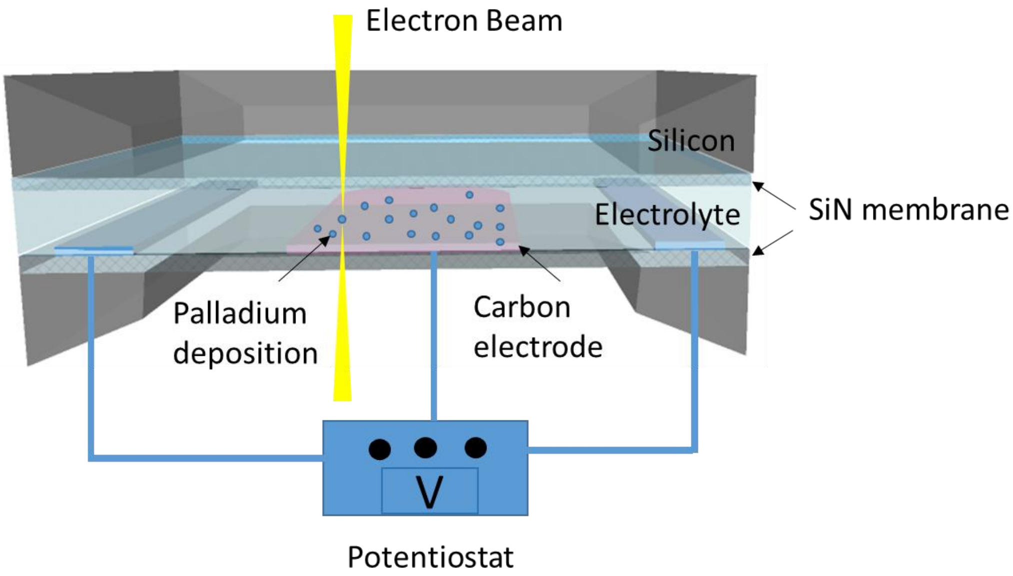

Figure 4.1. Schematic of an *in situ* liquid electrochemical cell TEM used for electrodeposition of palladium from 5 mM H_2PdCl_4 electrolyte in the presence and absence of HCl. Both silicon chips have a silicon nitride membrane, with the bottom chip containing three-electrodes (working, reference and counter) as an electrochemical setup. Palladium nanostructures are formed on the carbon-working electrode by applying a fixed potential.

To understand the effect of HCl on the structural evolution of palladium crystallites during electrodeposition, two different experiments were conducted. The first experiment was focused on the *in situ* electrodeposition of palladium on a carbon microelectrode from a solution of hydrogen chloropalladate (H_2PdCl_4), and the second one was performed by adding HCl to the H_2PdCl_4 precursor solution. The time-resolved bright-field scanning transmission electron microscopy (BF-STEM) micrographs, along with the current time transients (CTTs) obtained during these experiments are demonstrated in Figure 4.2. In the case without HCl (Figure 4.2(a)), nucleation and growth were observed, initially (0-10 s), along the electrode edge. At deposition times of 30 s or larger, nuclei started to appear on the inner electrode area. After 30 s of electrodeposition, palladium structures started to appear beyond the electrode edge. In the case with HCl, initially (0-10 s of deposition), the large majority of crystallites appeared along the edge of the electrode, and these edge-bound nuclei finally grew into microscale clusters at 150 s. At longer times ($t \geq 10$ s), palladium deposits appeared in the inner area of the electrode; however, the amount of palladium (evaluated based on cluster size and surface density) electrodeposited in this area was significantly smaller than the amount present at the electrode edge at every time point. This behavior was also seen in the experiment without HCl; however, the enhanced deposition at the electrode edge is more pronounced in the case with HCl. Previous reports have indicated that the adsorption of chloride ions on the electrode surface retards the palladium electrodeposition process. However, this effect is dependent on the electrodeposition overpotential: at high overpotentials, the chloride concentration at the electrode surface tends to decrease, diminishing the chloride-related retardation process.[193] According to the electric field simulations performed on the miniaturized electrochemistry setup, we observe electric field enhancement at the electrode edges (Supplementary Figure S4.1). In both cases, with and without HCl, this field enhancement increases the deposition rate at the electrode edges. However, in the case with HCl, this field enhancement is expected to play an additional role, it overcomes the potential barrier caused by the adsorption of chloride ions at the electrode edge. This results in a considerable difference in the amount of deposits present at the electrode edge and the inner electrode area.

Comparing the regions of the chip that were illuminated (Figure 4.2, 150s) and were not illuminated (Figure 4.2, 150 s-no beam) by the electron beam during electrodeposition, we obtain interesting insights on the interplay between electrodeposition and electron beam-induced nucleation and growth. Under the influence of electron beam, the structures present at the electrode edge had a dendritic structure that is observed in diffusion-limited growth. This is consistent with other reports suggesting that electron beam can affect the electrochemical process, requiring the electron beam dose to be controlled to avoid local depletion of palladium ions.[135,194] Another observation that is solely relevant to the case without HCl is that under the direct influence of electron beam, deposits were present on the silicon nitride window beyond the boundary of the carbon electron. This suggests that adding HCl to the electrodeposition bath reduces the rate of beam-induced nucleation and growth.

We believe that the electron beam impacts the electrodeposition process differently in solutions with and without HCl due to the differences in solution pH and chloride ion concentration. The interaction of the electron beam with aqueous solutions results in the generation of highly reactive oxidizing ($OH\cdot$ and H_2O_2) and reducing (hydrated electrons, H and H_2) species[94]. Previous studies have shown that the ratio of hydrated electrons to hydroxide radicals decreases as the solution pH is decreased due to the rapid combination of hydrated electrons with hydrogen ions[90]. This suggests a decrease in beam-induced nucleation (*i.e.* beam-induced reduction of metallic ions) in solutions with a lower pH. Furthermore, in solutions with a high concentration of chloride ions, the primary radical $OH\cdot$ reacts with chloride ions resulting in the generation of Cl_2^- (equations (1) and (2)), which is an oxidizing agent[195].

$$OH\cdot + Cl^- + H^+ \rightarrow H_2O + Cl \qquad (1)$$

$$Cl + Cl^- \rightarrow Cl_2^- \qquad (2)$$

Consequently, we expect the solution containing HCl to result in an environment that is more oxidizing under the electron beam compared to the solution lacking HCl, making it more difficult for the beam induced reduction of metallic ions to occur.

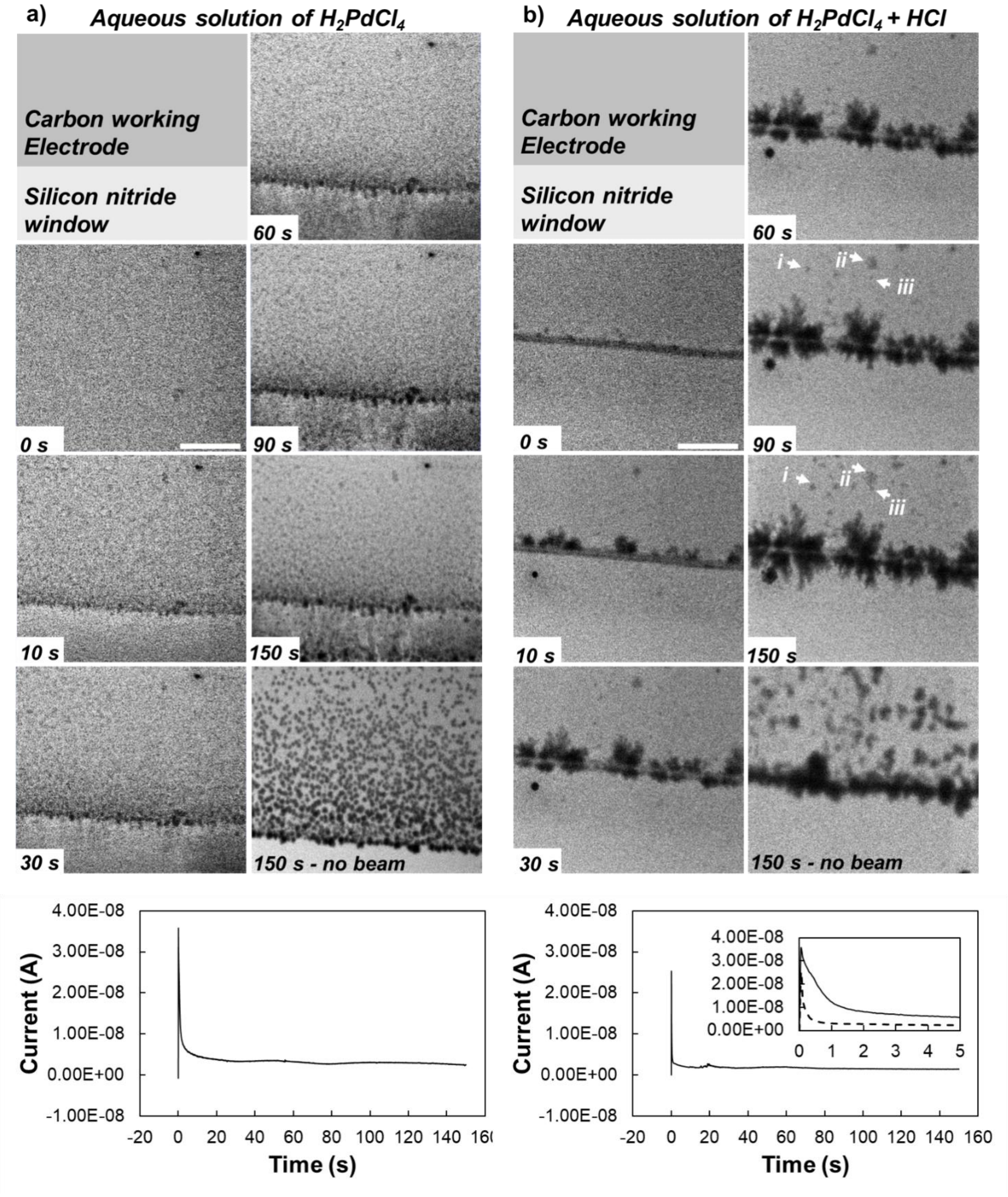
a)
Aqueous solution of H_2PdCl_4
Carbon working Electrode
Silicon nitride window
0 s
10 s
30 s
60 s
90 s
150 s
150 s - no beam
b)
Aqueous solution of H_2PdCl_4 + HCl
Carbon working Electrode
Silicon nitride window
0 s
10 s
30 s
60 s
90 s
150 s
150 s - no beam
i
ii
iii
Current (A)
Time (s)
4.00E-08
3.00E-08
2.00E-08
1.00E-08
0.00E+00
-1.00E-08
-20
0
20
40
60
80
100
120
140
160
0
1
2
3
4
5

Figure 4.2. Electrodeposition of palladium in the *in situ* liquid electrochemical cell TEM with and without the addition of HCl. The top row schematic represents the orientation of microchips as seen in the images in this Figure. BF-STEM micrographs acquired at 0 s, 10 s, 30 s, 60 s, 90 s, and 150 s of deposition on a carbon electrode in a 5 mM M H_2PdCl_4 bath without (a) and with 0.015 M HCl (b) under an applied potential of -0.2 V versus Ag/AgCl, flow rate of 5 μL/min, and a beam dose of 21 electrons/frame. nm^2. The micrograph labeled as 150 s-no beam represents an image of the chip following 150 s of electrodeposition, acquired after turning off the electrical bias and replacing the electrodeposition bath with water. The bottom row represents the current time transients obtained during the *in situ* LEC experiment. The inset in the current time transients represents the 'with' and 'without' HCl curves overplayed and zoomed in to show the first five seconds of deposition. Scale bar represents 1 μm.

To understand the cause of morphological differences induced by adding HCl, we compared the CTTs obtained during the *in situ* experiments of Figure 4.2. In both electrolytes, we observed a current decrease following the application of the potential step (-0.2 versus Ag/AgCl). In potential step experiments, this type of current decrease is often attributed to the double layer capacitive charging; however capacitive currents have time constants that are typically in the order of microseconds[196] rather than milliseconds or seconds. We sought to explain these results using the models developed by Scharifker and Hills (SH model). The most significant feature of the SH model is that it predicts a current increase following the capacitive discharge. This current increase is caused by the increase in the electroactive surface area as the number of nuclei increases and/or the nuclei grow in size[162]. Since this behaviour was not observed in the CTTs measured here, we turned to an alternative model based on electrochemical aggregative growth, which is applicable to CTTs with monotonically decreasing currents.[26] In electrochemical aggregative growth, electrodeposits are formed by self-limited growth of nanoclusters, overpotential-dependent nanocluster surface diffusion, and nanocluster coalescence/recrystallization[26,27,47]. This differs from the conventional electrochemical nucleation and growth theories in that, while primary nuclei grow by direct adatom attachment, beyond a critical diameter, they grow by nanocluster aggregation and coalescence.

To evaluate the suitability of this model for explaining the measured CTTs, we imaged the microchips used in the liquid cell TEM experiments using scanning electron microscopy (SEM) after the electrodeposition process. The *post situ* SEM images (Figure 4.3) confirm the observations obtained from liquid cell TEM (Figure 4.2). The amount of deposits increased at the electrode edge compared to the inner electrode area, and adding HCl to the electrodeposition bath changed the structures from spherical to non-spherical deposits. Additionally, SEM micrographs demonstrate that the deposited areas, in the case with and without HCl, contained small circular clusters (Supplementary Figure S4.2) even at long deposition times (150 s). We expect these clusters to be the building blocks of the larger spherical or aspherical particles observed without and with HCl respectively. In addition to this observation, reverting back to the BF-STEM images obtained during the *in situ* experiment (Figure 4.2), we see surface diffusion of nanoscale cluster on the electrode surface (particles *i*, *ii*), as well as coalescence of nanoscale clusters (particles *ii* and *iii*). The observation of nanoscale building blocks on the electrode surface, in addition to the monotonically decreasing current in the CTT curves support the electrochemical aggregative growth model.

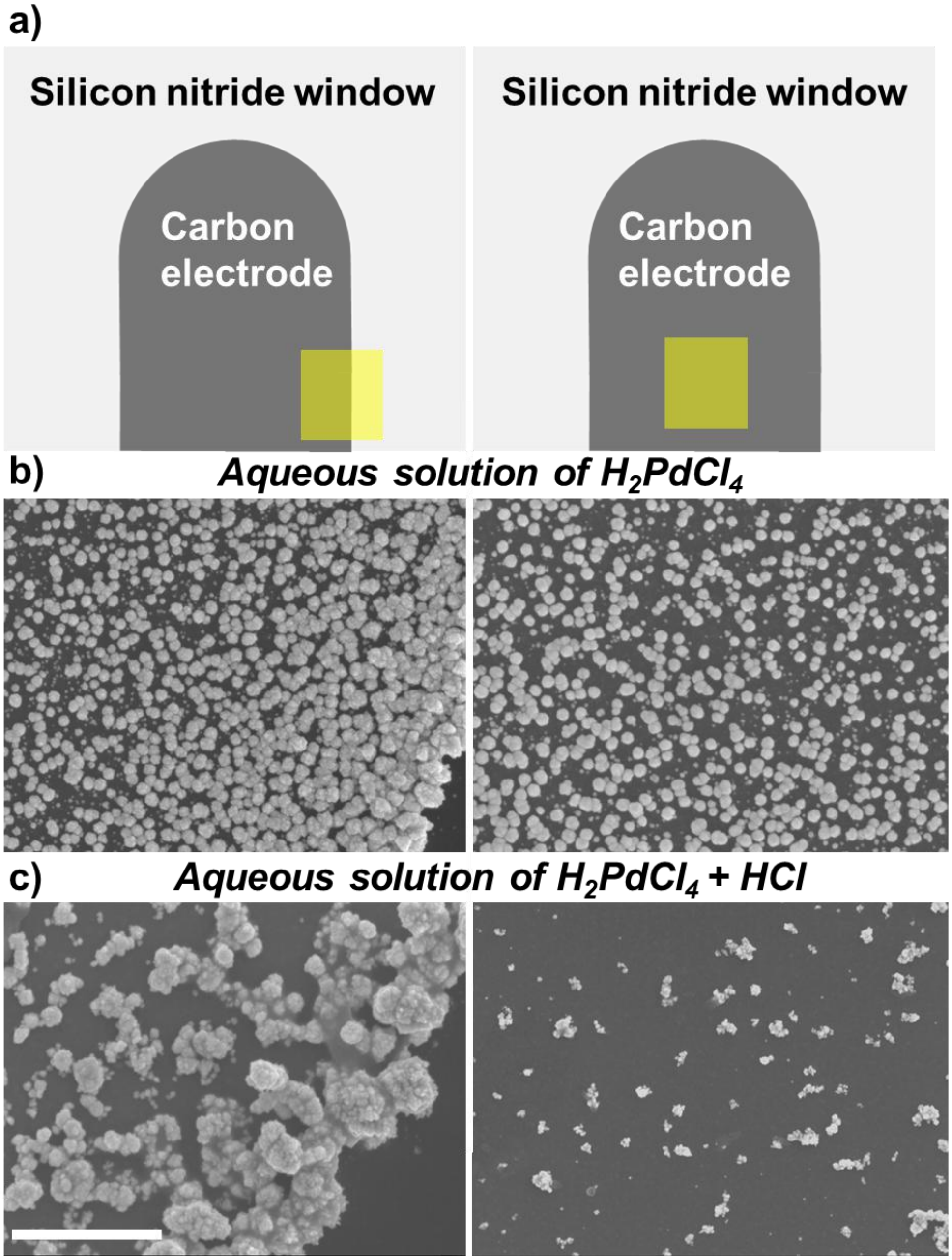

Figure 4.3. *Post situ* imaging of the electrochemical chip used in the *in situ* LEC-TEM experiment of Figure 4.2. The schematic drawing in (a) demonstrates the area imaged in (b) and (c). *Post situ* SEM micrographs of the chip used in the *in situ* LEC experiment of electrodeposition in Figure 4.2 without HCl in (b) and with HCl in (c). The images on the left demonstrate an area of the chip that contain the edge of the carbon electrode, while the images on the right show the middle part of the carbon electrode.

After selecting a suitable theory for explaining the nucleation and growth of palladium clusters, we used this model to explain the role of HCl on the morphological development of the clusters. Previous studies suggest that recrystallization and coalescence kinetics, to a large extent, dictate the morphology of the final electrodeposits.[26] Without HCl, we observed spherical clusters that were less porous and smoother than with HCl. Including HCl in solution, resulted in aspherical clusters that had a porous and open morphology. This suggests that recrystallization and direct addition of palladium are less dominant in the case with HCl. We present two hypotheses for explaining the role of HCl in impeding the recrystallization and direct addition processes.

1. It is known that at pH < 5, $PdCl_4^{2-}$ is the dominant Pd (II) species. The concentration of this complex ion decays sharply in the 6-10 pH range, with a parallel increase in the concentration of hydroxide-containing Pd (II) species.[192] The dissociation of $PdCl_4^{2-}$ results in the generation of adsorbed $PdCl_2$ species, which favours chloride ion adsorption at the electrode[193]. We expect this to result in the retardation of direct palladium addition in the presence of HCl.
2. We performed electrodeposition at a potential (-200 mV versus Ag/AgCl) close to the hydrogen adsorption/desorption potential (supplementary Figure S4.3). In this potential range, there is competition between the adsorption of hydrogen species and the direct attachment of palladium atoms.[197] We expect this competition to be enhanced in the electrolyte with a lower pH, and to decrease the direct addition of palladium atoms in the HCl-containing solution.

4.5 Conclusions

We studied the role of HCl in the structural evolution of palladium electrodeposits using liquid cell TEM and *post situ* TEM and SEM analyses. We found that aggregative electrochemical growth, based on self-limiting growth, surface diffusion, and recrystallization, best explained the current time transients and the electron microscopy images obtained here. The addition of HCl in the electrodeposition bath transformed the morphology of palladium electrodeposits from non-porous and closed clusters with a circular projection to porous and open clusters with an aspherical morphology. It is evident that HCl hinders the recrystallization of aggregated nanoclusters. We hypothesize this to be related to the adsorption of chloride ions and/or the competition between palladium adatom addition and hydrogen adsorption in the presence of HCl. It is evident that combining *in situ* and the *post situ* analyses provides invaluable insight on the complex phenomena that occur during electrodeposition.

4.6 Acknowledgements

We acknowledge financial support from NSERC supporting this work. We also acknowledge Dr. Glynis de Silveira, Dr. Andreas Korinek, and Andy Duft for assistance with experimental establishment and discussions with image analysis. L.S. is the Canada Research Chair in Miniaturized Biomedical Devices, and G.A.B. is the Canada Research Chair in Microscopy of Nanoscale Materials. Both Chairs are supported by the Canada Research Chairs Program. The microscopy work was carried out at the Canadian Centre for Electron Microscopy, a facility supported by the Canada Foundation for Innovation under the Major Science Initiative program, NSERC and McMaster University.

4.7 Supplementary Information

Lists of Contents

Figure S4.1 shows simulation on electric potential and electric field distribution of the carbon working electrode during in situ electrodeposition.

Figure S4.2 shows the size distribution of deposited palladium particles on carbon electrode after in situ electrodeposition in solution with and without HCl.

Figure S4.3 shows the *in situ* cyclic voltammetry of carbon electrode in solution with and without HCl.

1. Electric field distribution on carbon electrode during electrodeposition

The simulation on electric potential and electric field distribution on carbon electrode was performed using COMSOL Multiphysics 4.3b (COSMOL Inc., Stockholm, Sweden), the results are shown in Figure S4.1.

Both top view (Figure S4.1 (a)) and front view (Figure S4.1 (b)) show an enhanced electric potential and electric field at the tip and along the edge of the carbon electrode, compared with inner flat area.

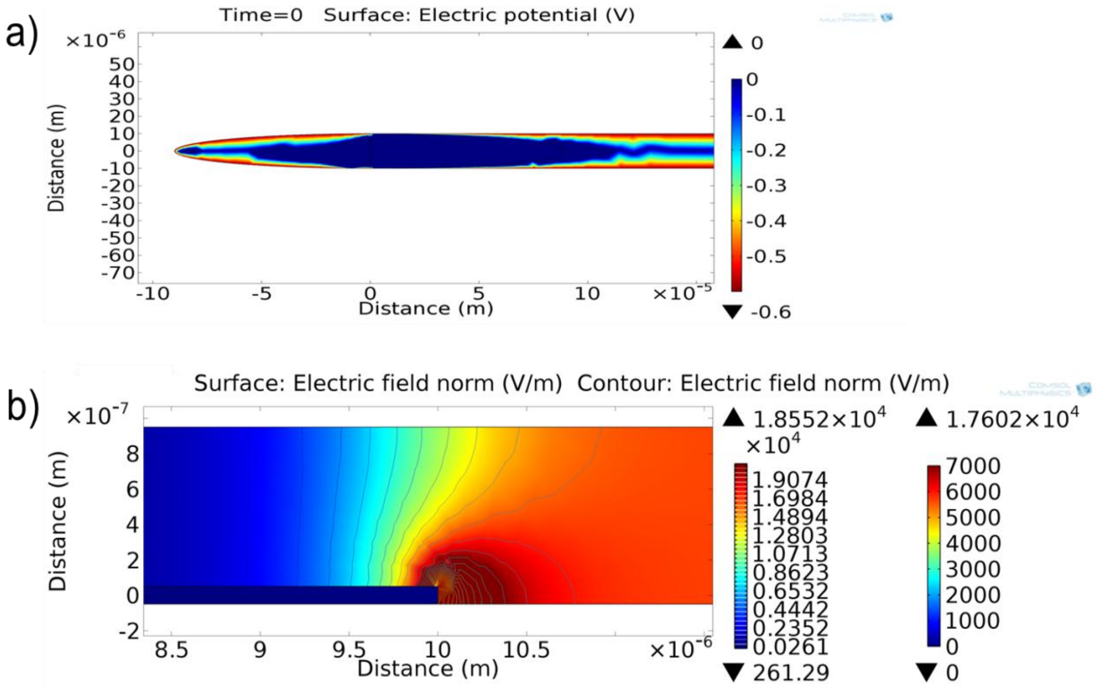

Figure S4.1.Simulation on Electric potential and electric field distribution on carbon electrode during in situ deposition of palladium. (a): top view of electric potential on carbon working electrode in electrolyte; (b): zoomed-in cross section of the carbon working electrode showing electric field distribution at the edge and inner flat area of the electrode in electrolyte.

2. Analysis of the size distribution of deposited palladium particles

The size of the palladium particles grown from in situ electrodeposition in solution with and without HCl was measured based on Figure 4.5(b) and 4.5(d) from the main text. Projected circles of the palladium particles were extracted, segmented and labeled by excluding those incomplete particles shown along the edge of the SEM images using *ImageJ*. The size of each palladium particle was described as the diameter of a circle having the same area as the projected particle area. Figure S4.2 summarizes the cluster diameter distribution of the deposited palladium from solution without HCl (a) and with HCl (b) extracted from the SEM images from Figure 4.5(d) and (d).

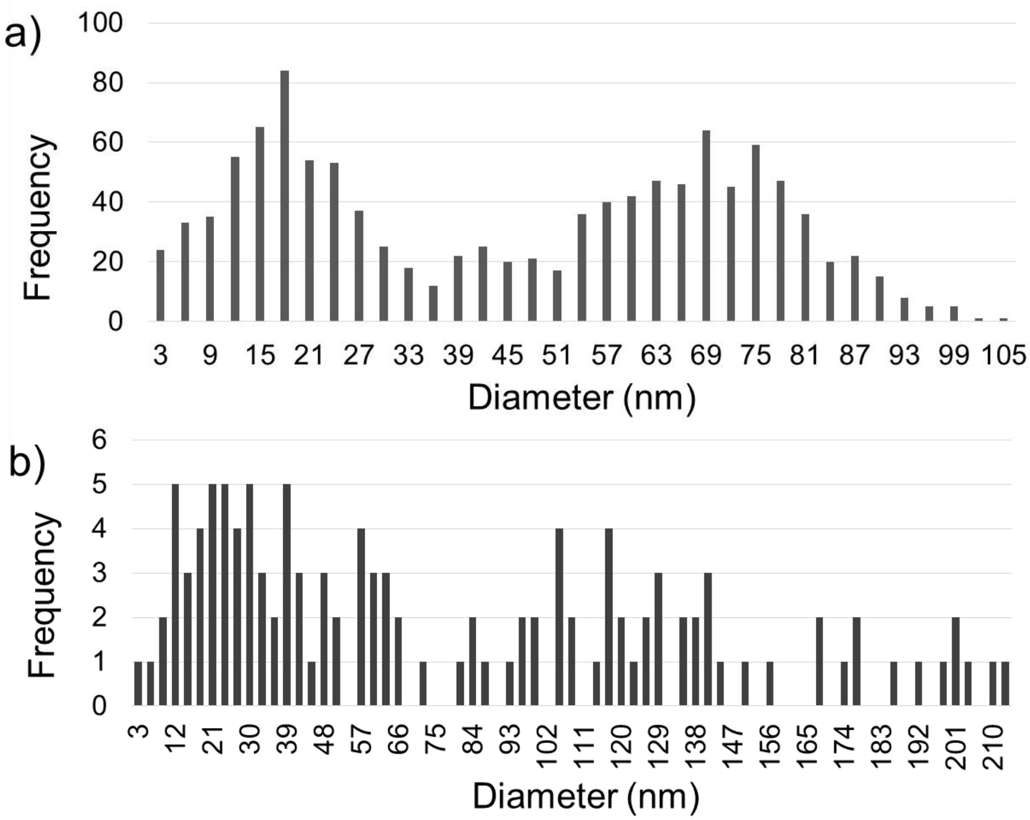

Figure S4.2. Histogram showing size distribution of palladium particles deposited on carbon electrode in solution without HCl (a) and with HCl (b), 3 nm binned.

3. In situ cyclic voltammetry of carbon electrode in H_2PdCl_4 with and without HCl

Cyclic voltammetry was performed on the carbon electrode in the same solution as that used for in situ electrodeposition from Figure 4.2 and Figure 4.3, with an electron beam dose of 21 electrons/frame.nm^2 under scan rate of 100 mV/s. Figure 4.3S shows the recorded current versus potential from a single scan.

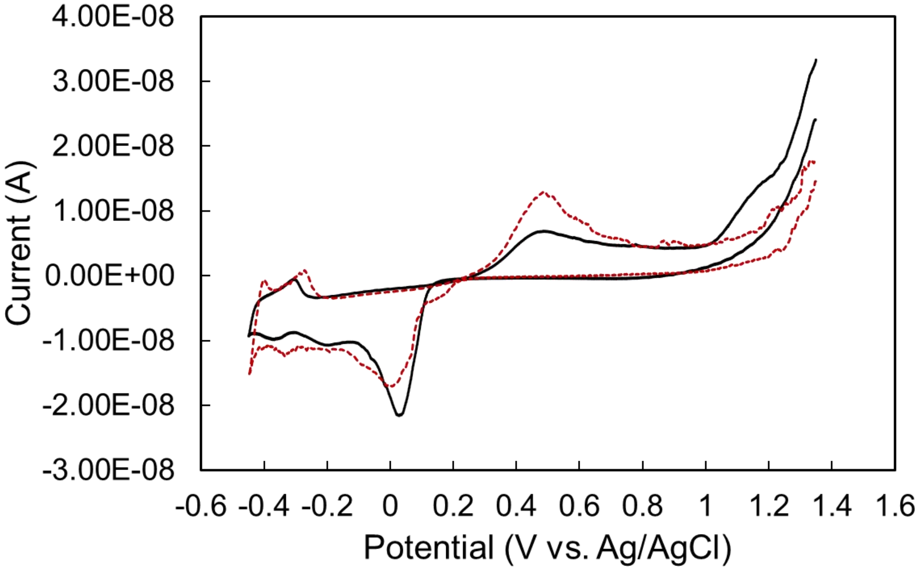

Figure S4.3. The current versus potential recorded from in situ cyclic voltammetry in solution without (solid black) and with HCl (dotted red).

Chapter 5 Imaging the structural evolution of palladium nanostructures under electrochemical cycling using *in situ* TEM

Chapter Introduction (Objectives (1), (3) and (4))

Palladium nanoparticles, when used as a catalyst, reduce, oxidize, and interact with hydrogen during electrochemical cycling. In order to study the structural evolution of palladium during electrochemical cycling, this chapter focuses on applying cyclic voltammetry to develop and characterize palladium nanostructures in palladium salt solutions (Objective (1), (4)). The effect of HCl, as supporting electrolyte, on the formation, dissolution, and hydrogen co-deposition and hydrogen desorption process was studied (Objective (3)). In both solutions (palladium salt electrolyte with and without HCl), we observed: (1) rapid growth during reduction process; (2) Movements of palladium particles along the electrode edge during hydrogen desorption process. However, in palladium salt solution with HCl, we observed some unique behaviours of the palladium clusters including (1) Dissolution of palladium clusters during the oxidation process and (2) Aggregation and formation of irregular structure clusters during hydrogen adsorption/absorption/evolution and desorption process. Finally, the morphology of the formed palladium nanoparticles are compared from solutions with and without HCl using *post situ* scanning electron microscopy. It was found that HCl caused the formation of chain-like and irregular palladium clusters. This coarsening behaviour of the palladium nanoparticles through dissolution, migration and coalescence resulted in the decrease of the total active surface area, which was considered as the main reason that caused efficiency loss as catalyst in fuel cells.

Authors: Jie Yang, Gianluigi A. Botton and Leyla Soleymani

5.1 Abstract

Palladium nanoparticles show excellent catalytic properties which find application in various electrochemical reactions. However, the mechanism and kinetics involved in the electrochemical processes are traditionally studied using ex situ methods and lack direct experimental proof. In this study, we use *in situ* liquid cell transmission electron microscopy to investigate the mechanism of palladium nanoparticles evolution under electrochemical cycling. The electrocrystallization, oxidation and dissolution, as well as the co-deposition with hydrogen absorption and desorption, were studied in real time by running cyclic voltammetry in palladium solutions with different compositions. We observed crystal growth during the reduction process and movement of the deposits during the hydrogen desorption process in the palladium salt solution. On the other hand, after adding HCl as the supporting electrolyte, we found an obvious dissolution of palladium nanoparticles during the oxidation process, as well as the enhanced movement and aggregation of these particles during the hydrogen reaction process. We propose that the existing stable palladium chloride compounds contribute to the dissolution of palladium from the solution with HCl. We also consider that the aggregation of palladium nanoparticles in the solution with HCl was caused by the enhanced hydrogen interfacial transfer through the palladium crystals, which resulted in different morphologies as compared to those formed from the solution without HCl. Besides the *in situ* characterization, *post situ* imaging demonstrates that the electron beam did not cause observable changes to the morphology of the formed palladium nanostructures in both solutions. These findings provide detailed descriptions of the palladium structural

evolution under electrochemical cycling and demonstrate the capability of the *in situ* system in studies on dynamic processes involving nanostructures.

5.2 Introduction

Palladium nanoparticles have been under research and investigations in fields such as hydrogen fuel cells[3,182] and biofuel cells[181]. Besides its nobility, palladium exhibits a unique ability to adsorb and absorb hydrogen, and form compact and stable surface oxides, which has been an topic of interest in numerous studies[49,7–15]. Among the fabrication and characterization methods used on palladium nanoparticles, electrochemical methods[206–210] are extensively used since palladium nanoparticles exhibit high catalytic activity towards several electrochemical processes, such as hydrogen absorption and hydrogen evolution[49].

It is known that the electrocatalytic properties of palladium particles, and the mechanism of the related reactions, are strongly affected by their morphology, dimension and the composition of electrolyte[50,199,211]. One prevailing topic is the interaction between the supporting electrolyte of HCl and palladium (ions) co-existing in palladium salts, which have been investigated in previous studies and is summarized as below: first, there are different kinds of palladium chloride compounds existing in palladium salt solution, depending on the conditions of the electrolyte, such as pH, concentration of HCl, etc[192]. The stability of these compounds determines the direction of the Pd/Pd^{2+} reaction. Second, the adsorption of chloride ions on specific crystalline planes forms blocking sites, which hinder the growth of palladium[190,191]. Lastly, since palladium is an excellent host for absorbed hydrogen, this results in the formation of palladium-hydrogen alloys during hydrogen absorption/evolution process. This causes brittle fracture during long deposition time[212]. Thus, there is a great need for direct experimental proof on the structural evolution of palladium to better understand the effect of HCl. However, traditional studies have relied on the electrochemical and microscopy characterization being performed separately, which may miss some fast transitions occurring on the sample, or induce extra reactions or contaminations during the sample transfer procedure.

In situ liquid cell transmission electron microscopy, a recent developed technique, has overcome the above limitations. With this technique, it is possible to realize real time observation on the structural evolution of nanomaterials in their native environments[70]. Various electrochemical studies have been performed using this technique, such as corrosion[132], electropolishing[67], electrodeposition[59,67,106,125,126,128,129], battery charge/discharge processes[128,135,213] and degradation of catalytic materials[214]. Although there are still some challenges for applying this technique, such as decreasing beam effect and increasing the resolution[94], in situ liquid cell TEM is becoming a powerful tool to provide direct experimental results to support, prove or modify existing theories, and give insights into developing hypotheses on mechanisms of different dynamic processes.

In this work, we sought to apply an *in situ* liquid cell TEM system to study the structural evolution of palladium nanoparticles by performing cyclic voltammetry in palladium salt solution with and without HCl. The growth, dissolution and movements of palladium nanostructures were captured at different potential ranges and the role of HCl was studied. This work allowed us to study the dynamics of nanoparticles during electrochemical cycling and investigate the effect of HCl on the structural development process.

Furthermore, combined with the *post situ* imaging, we demonstrated that the electron beam was brought down to non-detectable levels.

5.3 Experimental

5.3.1 Reagents

All chemicals were obtained in the highest available purity and used without further purification. Palladium (II) chloride powder (⩾ 99.9%) and Hydrochloric acid (ACS reagent, 37%) was purchased from Sigma-Aldrich, Saint Louis, MO, USA. 1 M HCl solution was made by adding 3.083 mL HCl into 100 mL Milli-Q water; 0.1 M Hydrogenchloropalladate (H_2PdCl_4) stock solution with was made by mixing 177.33 mg palladium chloride powder and 2 mL 1M HCl into 7.956 mL Milli-Q water, dissolved as a clear brown solution after four-hour sonication. 5 mM H2PdCl4 was made by diluting the 0.25 mL stock solution by adding 4.75mL milli-Q water. And 5 mM H2PdCl4 in 0.015 M HCl was made by diluting 0.25 mL stock solution by adding 75 mL of 1 M HCl and 4.675 mL milli-Q water. Both palladium solutions were bubbled with nitrogen for 20 min to remove dissolved oxygen before *in situ* voltammetry cycling.

5.3.2 *In situ* system

The *in situ* liquid cell TEM system (Poseidon 500, Protochips Inc., Raleigh, NC, USA) used in this study included a special designed TEM holder containing a liquid electrochemical cell at the tip. This holder is also integrated with electrical and fluidic circuitry for interfacing the electrochemical cell with a potentiostat (Gamry Reference 600, Gamry Instruments Inc., Warminster, PA, USA) for electrochemical control and a syringe pump (Harvard 11 Elite standard infuse only syringe pump, Harvard Apparatus Inc., Holliston, MA, USA) for fluidic control. The liquid cell was composed of two micro-fabricated silicon chips which seal the electrolyte in between. Both chips contained electron transparent silicon nitride windows (back-etched on a silicon substrate) for *in situ* observation, and spacers for controlling the liquid thickness. The top chip included patterned silicon nitride structures for guiding the liquid flow, and the bottom chip contained three micro-electrodes for creating a miniaturized electrochemical cell. The commercially available bottom chips (ECT24-CO, Protochips Inc., Raleigh, NC, USA) used in this work integrated carbon working electrodes, Pt reference electrodes, and Pt counter electrodes on silicon/silicon nitride chips and contained 500 nm spacers. The top chips with 150 nm (EPB-55DF, Protochips Inc., Raleigh, NC, USA) was used in this study.

5.3.3 *In situ* Cyclic Voltammetry

In situ cyclic voltammetry on carbon electrode in 3μL/min fluidic solution of 5mM H_2PdCl_4 with and without 0.015 M HCl was performed under the potential window of -0.8 V~1V vs. Pt reference electrode, with the scan rate of 100mV/s. During the *in situ* CV scans, the applied potential voltage started from open circuit potential, firstly went towards negative values and then towards positive values and finally back to the open circuit potential, which was considered as one single cycle in this study. The real time imaging was performed using bright field scanning TEM (BF-STEM) with beam dose of 21 electrons/frame. nm^2. The imaging was performed using a JEOL 2010F TEM operated at 200 kV. Bright-filed scanning transmission electron microscope (BF-STEM) imaging was acquired using a DigiScan II (Gatan, model 788) unit with a BF Gatan detector with time resolution of 0.555 s/frame. The whole *in situ* process was recorded in STEM mode and *in situ* images were extracted from the *in situ* videos.

5.3.4 *Post situ* analysis

The *post situ* characterization on the palladium structures formed on the carbon electrode was performed using the JEOL 7000 field emission SEM. The chips were rinsed in DI water and air dried prior to analysis.

5.4 Results and Discussions

5.4.1 *In situ* cyclic voltammetry on carbon electrode in supporting electrolyte

We sought to use *in situ* liquid cell transmission electron microscopy (LC-TEM) to better understand the structural evolution of palladium nanostructures under electrochemical cycling. For this purpose, we performed an integrated imaging/electrochemical study inside a miniaturized electrochemical cell placed at the tip of an *in situ* LC-TEM holder. Two silicon chips, having electron-transparent silicon nitride membranes, formed the electrochemical cell. One of the chips was used for applying the electrochemical stimuli, and contained three microelectrodes with the working electrode positioned on the silicon nitride window, while the other membrane confined the liquid inside the cell. Furthermore, this holder was integrated with electrical circuity and fluidic circulation for conducting electrochemical experiments inside fluidic environments (Figure 5.1 (a)).

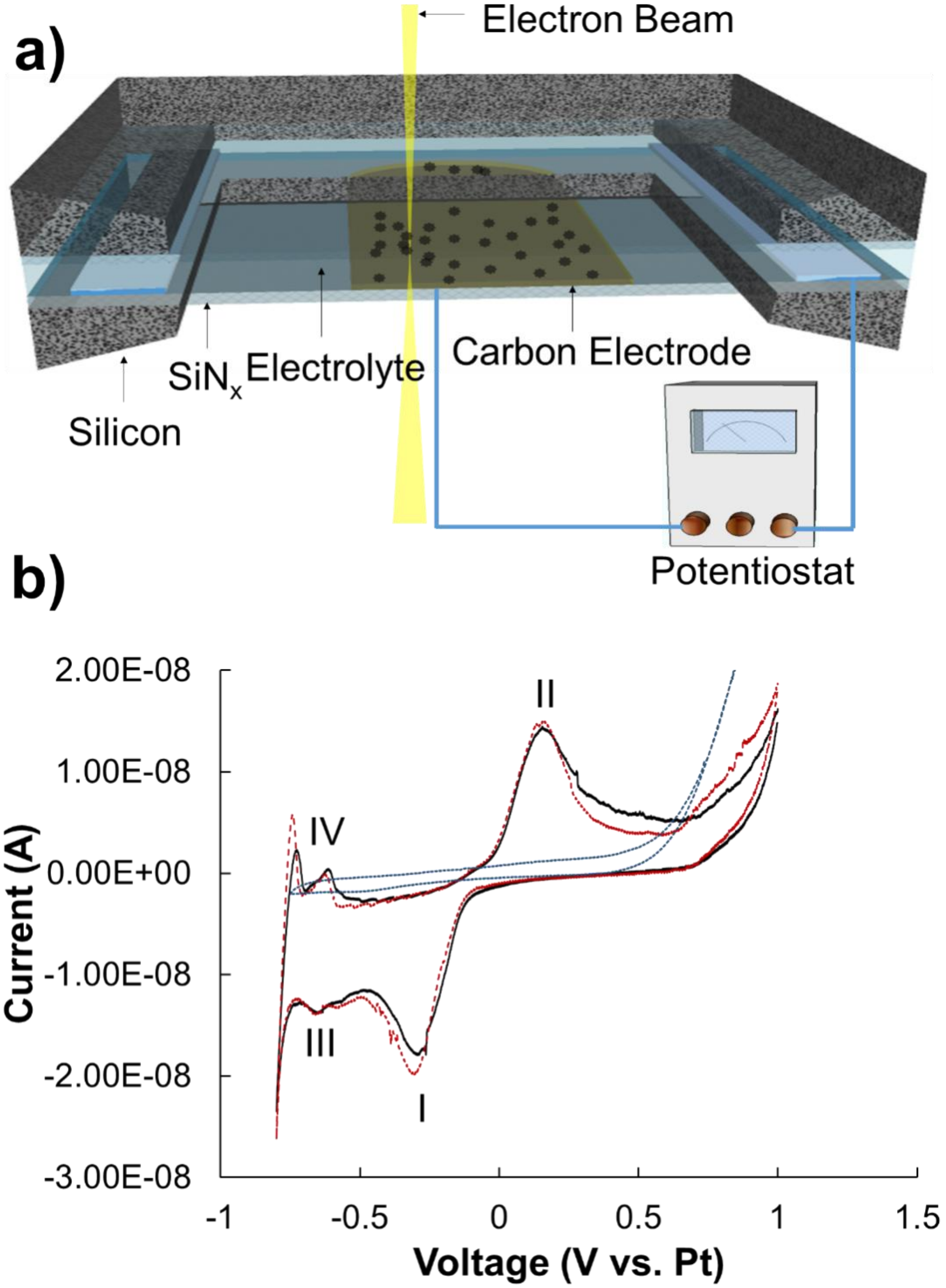

Figure 5.1. *In situ* LC-TEM for electrochemical analysis. (a): Schematic drawing showing the *in situ* LC-TEM setup used for electrochemical analysis. The bottom silicon chip contains three electrodes connected to an external potentiostat; (b): cyclic voltammogram acquired in the supporting electrolyte (HCl, blue dotted) and in the palladium salt solution (5 mM H_2PdCl_4 in 15 M HCl) with electron beam on (red dashed) and beam off (black solid).

In this study, cyclic voltammetry (CV) was performed inside the LC-TEM to investigate the structural evolution of palladium nanostructures during potential cycling (Figure 5.1(b)). The curves acquired in the presence of palladium salt demonstrated peaks that were not observed in the supporting electrolyte. These peaks were characteristic of palladium reduction (I) and oxidation (II), as well as hydrogen adsorption/absorption (III) and desorption (IV) processes. Furthermore, to investigate the effect of the electron beam on the generated electrochemical current, we performed the CV scan in the electrolyte containing palladium salt with the electron beam turned off (Figure 5.1(b)). There were no significant differences in the CV curves obtained in the presence and absence of the electron beam. This demonstrates that under the selected electron beam dose (21 electrons/frame. nm^2), fluid flow rate (3 μL/min), and solution concentration, the beam did not interfere with the potential cycling experiments.

5.4.2 *In situ* CV on carbon micro-electrode in palladium solution with/without HCl

Most of the previous studies on characterizing the deposition, dissolution, and hydrogen adsorption/desorption of palladium were based on electrochemical analysis and electron microscopy performed separately. In order to observe these processes in real time and in their native liquid environments, we used LC-TEM to acquire time-resolved bright field scanning transmission electron microscopy (STEM) images of a carbon working electrode during potential cycling in a solution containing palladium salt (5 mM H_2PdCl_4 in water). Using this system, we were able to relate the CV curves obtained during potential cycling (Figure 5.2(a)) to the electrode images obtained at different time points (Figure 5.2(b)).

To better understand the structural changes observed during potential cycling, we performed the combined imaging/electrochemical experiments for three voltammetric cycles. During the first cycle, electrochemical reduction started at -0.17 V and reached its peak value at -0.27 V. The corresponding images acquired during this time demonstrated the deposition of palladium along the edge and on the inner area (e.g., P_2, P_3, P_4) of the electrode (Figure 5.2(b), time points 1-2). As the potential was scanned towards more negative values, the reduction current decreased due to the depletion of palladium ions at the electrode surface, and the electrodeposition continued under a diffusion limited regime (Figure 5.2(a), time points 2-3). Starting at -0.63 V (Figure 5.2(a), time point 3), we observed a current increase, which represents the hydrogen adsorption/absorption process. During the forward negative scan, continuous growth of P_2, P_3, P_4 were observed (Figure 5.2(b), time points 1-3). The first anodic peak (Figure 5.2(a), time point 5) represents the hydrogen desorption peak, at which particle P_1 was "detached" from its adjacent particles (Figure 5.2(b), time point 5)[212]. As the potential was scanned towards more positive values, a second anodic peak (Figure 5.2(a), point 6) appeared, which represents the oxidation of palladium deposits. As we cycled back to the open circuit potential, we observe a reducing current in the order of a few nA from 0.2 to 0.5V, which we believe to be attributed to the reduction of Pd (IV) oxides. Previous studies have indicated that palladium oxidation during potential cycling results in the formation of a monolayer of palladium oxide[4949]. As a result, the structural changes related to palladium oxidation are not expected to be resolved using the current *in situ* method.

In addition to observing the correlation between the redox features and the structure of the deposited palladium particles within a single cycle, we also used our system to observe the structural and current changes that occurred over multiple redox cycles. It was seen from the CV curves (Figure 5.2(a)) that the palladium reduction peaks (time points 2, 8, 13) increased, and the onset for reduction moved to more positive potentials following each cycle. This, in addition to the cross over observed in the CV curves, indicated that palladium deposition on palladium was energetically preferred over palladium deposition on carbon. Comparing the images obtained at the palladium reduction peaks (Figure 5.2(b), time points 2, 8, 13), we see the growth of deposits at the electrode edge following every redox cycling. This is due to the observation that under oxidizing potentials (Figure 5.2(a), time points 6, 12), the palladium deposits remain on the electrode edge, and form the base for the following reduction cycle. Furthermore, the detachment of P_1 from its neighbors observed during the first hydrogen desorption cycle (time point 5), increases during the second and third cycles (time points 11, 16).

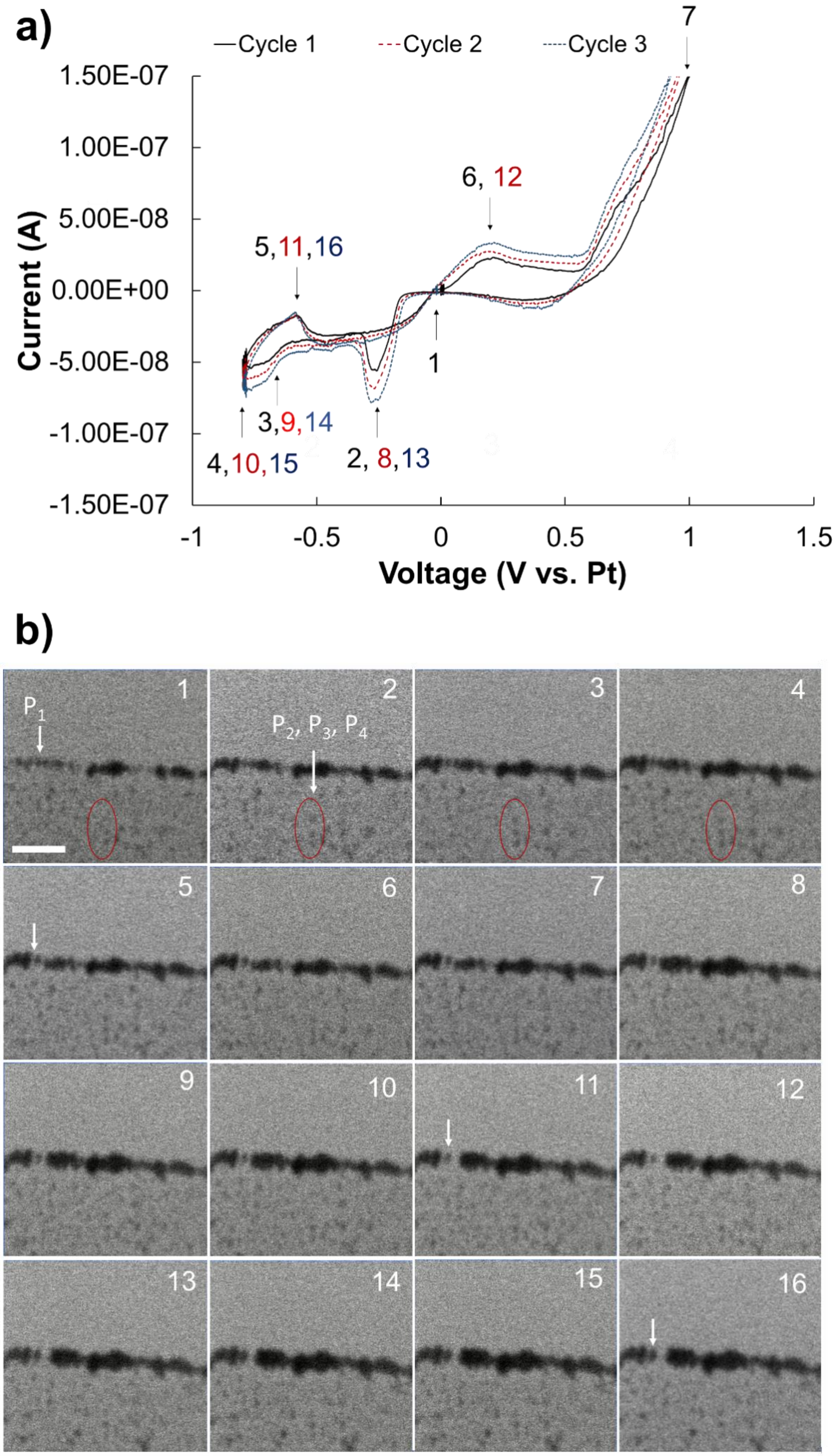
a)
Cycle 1
Cycle 2
Cycle 3
Current (A)
1.50E-07
1.00E-07
5.00E-08
0.00E+00
-5.00E-08
-1.00E-07
-1.50E-07
Voltage (V vs. Pt)
-1
-0.5
0
0.5
1
1.5
7
6, 12
5,11,16
1
3,9,14
4,10,15
2, 8,13
b)
1
2
3
4
5
6
7
8
9
10
11
12
13
14
15
16
P_1
P_2, P_3, P_4

Figure 5.2. *In situ* CV of carbon electrode in 5 mM H_2PdCl_4 with scan rate of 100mV/s. (a): The current transient acquired from *in situ* CV with respect to a platinum reference electrode; (b): BF-STEM images corresponding to the time sequence pointed in (a). Scale bar represents 0.5 μm.

Previous reports have demonstrated that the type and concertation of supporting electrolyte plays a critical role in controlling the structural evolution of metallic electrodeposits[2,185]. As a result, we performed another *in situ* CV measurement (Figure 5.3), where all conditions were kept the same as the previous experiment but HCl was added as the supporting electrolyte. During the first cycle (Figure 5.3(a)), the reduction initiated at -0.06 V (time point 1) and the reducing current reached its maximum value at -0.22 V (time point 2). As expected, the *in situ* images acquired during this time span demonstrated a rapid growth of palladium structures on the electrode surface. As we scanned through the hydrogen adsorption/absorption/evolution region (time points 3-4), there was more palladium deposited at the electrode edge, and chain like structures were observed on the flat area of the electrode, for example, clusters C_1 and C_2 (Figure 5.3(b), time point 4). When we reversed the scan, the first two anodic peaks represented the hydrogen desorption peaks (Figure 5.3(a)). Similar to what was seen in the previous *in situ* CV experiment without HCl, during this time span, we observed two "gaps" that were initiated during the hydrogen desorption region (Figure 5.3(b), time point 5). As the potential passed over the open circuit potential and the current reached its maximum value (Figure 5.3(a), time point 6), contrast loss for the deposited palladium was observed, and continued until the end of the reversed scan (Figure 5.3(b), time point 7). We expect this to be caused by the dissolution of palladium into the chloride containing solution[49].

As in the case without HCl, we also studied the current voltage characteristics and structural changes that occurred over multiple redox cycles. As shown in Figure 5.3(a), the palladium reduction and oxidation peaks increased and onset for reduction moved to more positive values during the second cycle, showing similar trend as that from solution without HCl. However, the reduction and oxidation profiles for the third cycle remained unchanged from the second cycle, indicating that a stable reversible redox reaction was established in the solution containing HCl. Comparing the images obtained at the palladium reduction peaks (time points 2, 8, 13), we see the growth of deposits following every redox cycling. (Based on the images obtained from the end of negative scan to the oxidation peak during the second cycle, we see dissolution of the palladium deposits (Figure 5.3(b), time points 11-12).) From the images acquired during the hydrogen adsorption/absorption/evolution process per each cycle (Figure 3(b), time points 4, 10, 15), we see particle coalescence and chain-like structures formation. For example, particle P_2 coalesced with the adjacent deposits as it grew, resulting in a chain-like structure (Figure 5.3(b), time points 8-10). Similar behavior were observed for Cluster C_4 in the second cycle (time point 10) and structural change for C_6 in the third cycle (time points 14-15). Comparing the images obtained during the hydrogen desorption process, the "gap" between particle P_1, P_3 and their neighbors formed in the first cycle (Figure 5.3(b), time point 5) were increased during the second cycle and third cycle (time points 11, 16). At the same time, some irregular structure aggregations formed, for example, clusters C_3, C_4 and C_5 in the second cycle (time points 10,11), and the chain-like cluster C_6 which was grown into two aggregates during the third cycle (time points 15-16). Based on the above observation, we believe that during the hydrogen adsorption/absorption/evolution and hydrogen desorption processes, the deposition of palladium was possibly through two different mechanisms: one is the direct reduction of palladium ions or attachment of palladium adatoms, the other is the aggregation of palladium particles (as they may grow at the same time).

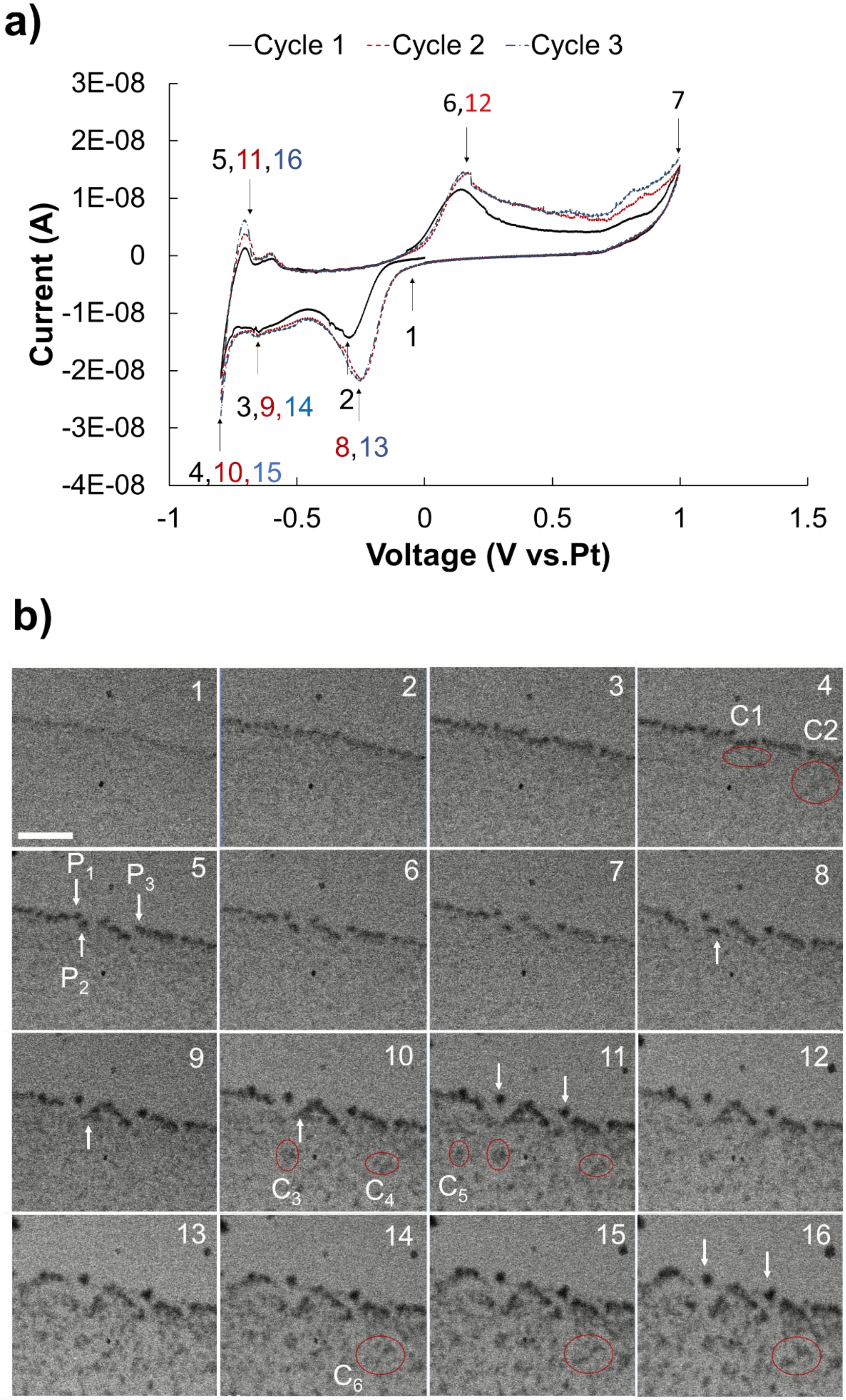
a)
—Cycle 1
---Cycle 2
-·-Cycle 3
3E-08
2E-08
1E-08
0
-1E-08
-2E-08
-3E-08
-4E-08
Current (A)
-1
-0.5
0
0.5
1
1.5
Voltage (V vs.Pt)
5,11,16
6,12
7
1
2
3,9,14
8,13
4,10,15
b)
1
2
3
4
C1
C2
5
P1
P2
P3
6
7
8
9
10
C3
C4
11
C5
12
13
14
C6
15
16

Figure 5.3. *In situ* imaging on CV of carbon electrode in 5 mM H_2PdCl_4 in 0.015 M HCl with scan rate of 100mV/s. (a): The current transient acquired from *in situ* CV with respect to a platinum reference electrode; (b): BF-STEM images corresponding to the time sequence pointed in (a). Scale bar represents 0.5 µm.

Through the *in situ* LC-TEM study performed here, we observe two major differences in the structural evolution of palladium deposits cycled in the *presence and absence* of HCl. The first difference is in the enhanced dissolution of palladium deposits during oxidative cycling in the *presence* of HCl (Figure 5.4(a)). The presence of chloride ions and the lower solution pH facilitate the formation of stable $[PdCl_4]^{2-}$ species, which inhibits the growth of palladium, and increases the dissolution rate of the loose palladium deposits in the solution containing HCl[192,215,216]. The generation of an oxidative environment caused by the interaction of the electron beam with chloride ions have been previously reported[90,195], and is expected to further enhance the dissolution rate of palladium in the solution with HCl. The second difference is in the increased mobility of palladium nanoclusters in the presence of HCl and the formation of aggregative assemblies (Figure 5.4(b)). The solution containing HCl has a higher concentration of hydrogen ions participating in hydrogen adsorption and desorption processes through their respective potential windows. The adsorption of hydrogen onto the surface of palladium nanoclusters, and its subsequent migration into the lattice have shown to induce plastic strain[217–219], while the desorption of hydrogen has resulted in significant defect formation. We expect the increased mobility of palladium nanoclusters to be related to the increase in the rate of hydrogen-related processes[219,220]. In addition, the adsorption of $[PdCl_4]^{2-}$ species on the Pd nanocluster surface, as well as their desorption during the hydrogen adsorption/desorption potential window is expected to contribute to the enhanced mobility and aggregation of palladium nanoclusters in the presence of HCl[221].

In order to compare the morphology of palladium structures formed in the presence and absence of HCl, we performed *post situ* scanning electron microscopy (SEM) on the working electrodes used in the LC-TEM experiments of Figures 2-3 (Figure 5.4(c)). Individual spherical nanoclusters are observed in the case without HCl; while chain-like aggregates are observed upon adding HCl to the electrolyte solution. In the case with HCl, nanoclusters having a diameter of 10-15 nm were observed near the growing cluster, suggesting that these nanoclusters serve as the building blocks for the aggregated assemblies. The *in situ* and *post situ* images observed in the HCl-containing electrolyte suggest that the recently-studied electrochemical aggregative growth mechanism, based on self-limited growth, surface diffusion, and aggregation, dominates palladium deposition in this experiment[26].

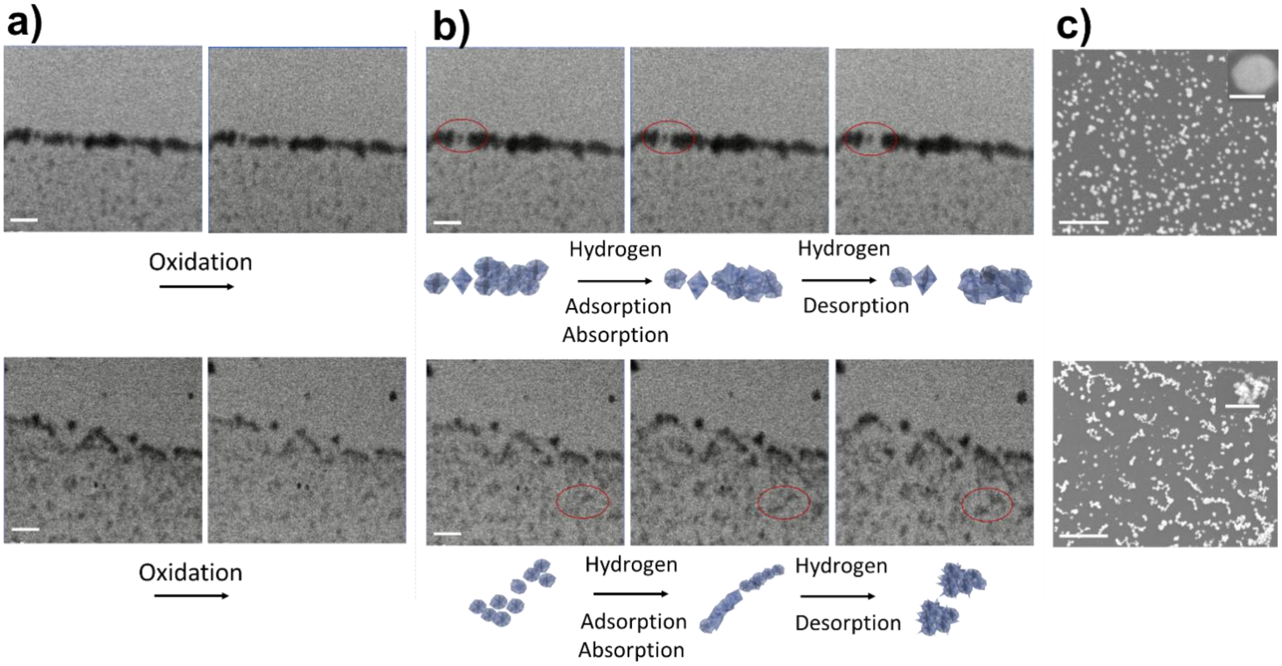

Figure 5.4. Comparison of the structural evolution of palladium nanoparticles in 5 mM H_2PdCl_4 (the first row) and 5 mM H_2PdCl_4 in 0.015 M HCl (The second row). (a): *In situ* STEM images of palladium structural change during oxidation process. Scale bars represent 0.5 µm; (b): *In situ* STEM images of palladium structural change during hydrogen adsorption/absorption/evolution and hydrogen desorption processes. The schematic drawings show the structural change of the circled clusters. Scale bars represent 0.5 µm; (c): *Post situ* SEM images of the palladium structures formed after *in situ* CVs from figure 2-3. Scale bars represent 1 µm. The inserts are the zoomed-in images of palladium particles and the scale bars represent 100 nm.

5.5 Conclusions

We have applied an *in situ* cyclic voltammetry method to observe the deposition, dissolution, migration of palladium nanostructures during reduction, oxidation and hydrogen adsorption/absorption/evolution and desorption processes. In doing so, we have studied the kinetics involved in the palladium structural evolution by combining the *in situ* imaging and electrochemical analysis.

We firstly evaluated the effects of the electron beam on the electrochemical response of the *in situ* liquid cell TEM system and identified a moderate beam dose to conduct the *in situ* cyclic voltammetry.

Using the optimized *in situ* liquid cell TEM system, we then observed palladium structural evolution by running a cyclic voltammetry in palladium solutions with and without HCl. We compared the two cases to study the effects of HCl on the dynamic processes during the *in situ* CVs, and found both similarities and differences between them. We found that both cases share some features in common in terms of the *in situ* cyclic voltrammogram and morphology formation process. Both CV profiles showed characteristics of reduction, oxidation, hydrogen adsorption/absorption/evolution and hydrogen desorption. A rapid growth of palladium was also observed at reduction peaks. However, as the cycling went through the hydrogen desorption and oxidization processes, some differences were observed in the solution with HCl. The HCl caused enhanced dissolution of palladium during the oxidation process and induced aggregations of the deposited palladium on the electrode surface during the hydrogen adsorption/absorption/evolution and hydrogen desorption process. This is assumed to be related to the involvement of large amounts of hydrogen in the palladium crystal growth process which causes defects in the Pd-H structures.

In addition to the *in situ* analyses, *post situ* SEM imaging was performed to compare the morphology and distribution of formed palladium after *in situ* CVs in the solution with HCl and that without it. Compared with the smooth spherical structures formed in the solution without HCl, the palladium structures formed in the solution with HCl showed chain-like structures and irregular structure aggregates. This was consistent with our *in situ* observation. Based on the *in situ* and ex situ results, we proposed that the formation of chain-like structures and irregular clusters in the palladium solution with HCl were dominated by the aggregation of pre-grown particles during the hydrogen sorption/evolution and desorption processes.

In summary, this *in situ* technique enables us to better understand the dynamics involved in electrochemical cycling processes, and provides direct experimental proof of the effect of HCl (the supporting electrolyte) on the structural evolution of nanoparticles. Combined with the *post situ* characterization, this technique provides insights into the study of intermediate reactions and products during various electrochemical processes.

5.6 Acknowledgements

We are grateful to NSERC for funding this work. We also acknowledge Dr. Glynis de Silveira, Dr. Gregory Jerkiewicz, Dr. Andreas Korinek and Andy Duft for assistance with experimental establishment and discussions with image analysis. L.S. is the Canada Research Chair in Miniaturized Biomedical Devices, and G.A.B. is the Canada Research Chair in Microscopy of Nanoscale Materials. Both Chairs are supported by the Canada Research Chairs Program. The microscopy work was carried out at the Canadian Centre for Electron Microscopy, a facility supported by the Canada Foundation for Innovation under the Major Science Initiative program, NSERC and McMaster University.

Chapter 6 Biomineralization of Calcium Phosphate Revealed by *in situ* Liquid-Phase Electron Microscopy

Chapter Introduction (Objectives (1), (5)):

In addition to the traditional techniques used to study biological processes, for example, Cryo-TEM, the *in situ* TEM technique also turns out to be a potential tool to investigate the dynamics during the early stage of biological processes. This chapter focuses on applying the *in situ* TEM system to study the calcium phosphate biomineralization process from simulated body fluid (Objective (5)). To decrease the electron beam interference with the biomineralization process, optimization of the *in situ* experimental conditions were carried out (Objective (1)). This includes applying silicon chips with micro-wells, control on liquid thickness and depletion, and reducing electron beam accumulation throughout *in situ* imaging. Besides the *in situ* observation, *ex-situ* control experiments *and post situ* characterizations (including electron energy loss spectroscopy and X-ray photoelectron spectrometry) were also incorporated to evaluate the electron beam effect and complete elemental analysis. It was found that the nucleation and growth of calcium phosphate structures were through attachment of pre-nucleation clusters which served as building blocks. The *in situ* study in this chapter provides direct experimental proof on the attachment-based growth model for calcium phosphate biomineralization process at the nanoscale. Furthermore, it shows the capability of the *in situ* technique to study biological processes involving more complex physiological interactions.

Authors: Xiaoyue Wang, Jie Yang, Carmen Andrei, Leyla Soleymani and Kathryn Grandfield

6.1 Abstract

Calcium phosphate (CaP) biomineralization is essential to the formation of bones and teeth, and other pathological calcifications. Unravelling the mechanism of CaP nucleation and growth contributes significantly to understanding diseases caused by pathological mineralization, and also to designing biomimetic materials with suitable properties. Recently, CaP was proposed to mineralize following a non-classical crystal growth pathway of pre-nucleation cluster aggregation. However, all observations have been based on *ex-situ* studies which are not sufficient evidence to prove the existence of this dynamic formation process. The advent of liquid-phase transmission electron microscopy (LP-TEM) allows for recording dynamic processes in liquid. Here, by using this real-time imaging technique, we present the first direct real-time evidence to demonstrate that CaP mineralization from simulated body fluid occurs by particle attachment, shown with nanoscale spatial resolution and sufficient temporal resolution. This work lays the foundation to investigating mineralization in other relevant biological systems in humans and vertebrates.

6.2 Introduction

Biominerals are diverse natural minerals formed by living organisms. Their elaborate hierarchical structure, distinctive mechanical properties and varied physiological functions have motivated decades of research on their mineralization processes.[222,223] Calcium phosphates (CaP) are one of the most highly researched classes of biominerals, for the reason that the carbonated calcium phosphate apatite crystal is the essential mineral component of both bones and teeth of vertebrates.[224] Also, CaP deposition plays an important role in several pathological calcifications (e.g. arteriosclerosis, and physical calculus).[225–227] Therefore, understanding the mineralization process of CaP will aide in unveiling biomineralization mechanisms of healthy tissues such as bone, dentin and cementum, pathological calcifications (e.g. kidney stones), and also contribute towards research in applied sciences related to human health, such as the development of biomimetic materials and realization of mineralization mechanisms toward synthetic implant systems.[226]

Currently, the mechanism of CaP nucleation and growth is not fully understood. Based on Cryo-TEM[228] and Atomic Force Microscopy (AFM) studies[229], CaP was suggested to mineralize through complex pathways involving pre-nucleation cluster aggregation, sequential morphological transformations, and finally traversing into the crystalline phase.[228–230] Amorphous calcium phosphate (ACP) has been reported as the transient phase in both *in vivo* and *in vitro* studies.[231–233] It has been proposed that the existence of ACP pre-nucleation clusters decreases the energy barrier to nucleation and enables biominerals, such as CaP, to mineralize following a non-classical crystal growth process defined as crystallization by particle attachment.[234] In this process, the pre-nucleation particles, which are regarded as building blocks, are initiated from the solvated state and aggregate with each other to form clusters with chain-like or branched morphology. These pre-nucleation particles could vary from multi-ion complexes to nano-crystals in different mineralization systems.[234] Although these chain-like or branched morphologies of the formed particles captured at defined time points provide important evidence to infer mineralization by attachment-based growth,[228,229] they alone are not sufficient evidence to prove the existence of this dynamic formation process. However, most studies on crystallization by particle attachment are still based on these *ex-situ* observations of crystals made after the pathway of initial nucleation.[230] Therefore, the need arises for a technique to render real-time observation of this dynamic process with nanoscale spatial resolution and necessary temporal resolution[234–236]. While *ex-situ* experiments based on, e.g. cryo-electron microscopy, are excellent for developing reasonable hypotheses, the *in situ* method developed here is critical in making conclusions based on direct evidence.

Liquid-phase transmission electron microscopy (LP-TEM), with the ability to record events in confined liquid between two electron-transparent membranes with nanoscale spatial resolution and real-time temporal resolution,[237,238] is a promising technique to image dynamic nucleation and growth process of CaP. This approach has been used to study the nucleation and growth of $CaCO_3$ [234,235,239] and provided direct experimental evidence for the existence of indirect formation pathways through the transformation of amorphous or crystalline precursors.[236] Also, the dynamic process of calcium ions binding to biopolymers in the formation of metastable amorphous calcium carbonate was recorded *via in situ* LP-TEM observation.[235] Looking beyond nucleation mechanisms of CaP, the functions of non-collagenous proteins (NCPs)[240] and the collagen matrix[241,242] on crystal nucleation and subsequent growth are also poorly understood. Therefore, *in situ* TEM research on CaP nucleation and growth could lay a foundation for applying LP-TEM techniques to explore these unsolved issues of bone biomineralization.

In this study, we present the first real-time imaging of CaP nucleation and growth with *in situ* LP-TEM, which provides direct evidence to demonstrate that CaP mineralization occurs by particle attachment.

6.3 Experimental

6.3.1 Mineralization solution

The CaP mineralizing solution was prepared according to Lausch and co-workers[241,243] who have demonstrated selective remineralization on demineralized murin dentin with this solution. The solution was made up of two parts: 1) a phosphate solution (9.5 mM Na_2HPO_4 (Sigma-Aldrich, USA) in 125 mM NaCl, 50 mM Tris (Sigma-Aldrich, USA), pH 7.40), and 2) a calcium solution (1.7 mM $CaCl_2$ in 125 mM NaCl, 50 mM Tris, pH 7.40). All reagents were purchased from Sigma Aldrich and dissolved in Milli-Q water. These two solutions were mixed and filtered through a 0.2 μm acrodisc syringe filter right before sealing in the liquid TEM holder for *in situ* experiments or placing in the beakers for *ex-situ* experiments at room temperature.

6.3.2 *In situ* STEM

The *in situ* TEM holder (Poseidon 500, Protochips Inc., Raleigh, NC, USA) used in this study contains a liquid cell placed at the holder tip. Two microfabricated silicon nitride microchips with 50 nm silicon nitride membranes were sealed inside the liquid cell and *in situ* imaging was performed by electrons passing through the overlapped silicon nitride membranes. A small amount (2 μL) of CaP mineralizing solution was put in between the two membranes, one of which was patterned with microwells, which assists in maintaining a relatively stable solution during the *in situ* mineralization process, and reducing beam effect interference between the individual microwells. The E-chips used in this study were commercially available bottom large chips (ETP-42A1, Protochips Inc., Raleigh, NC, USA) containing an 8 x 16 array of 10 µm x 10 µm microwell on a 400 µm x 200 µm SiN membrane and top chips of 300 µm x 90 µm SiN membrane without spacers (ECB-39A, Protochips Inc., Raleigh, NC, USA). Real-time imaging was performed using a JEOL 2010F TEM operated at 200 kV. Bright-field scanning transmission electron microscopy (BF-STEM) mode was used under beam dose of 2.198 x 10^3 e/$Å^2$·s. *In situ* images were acquired using DigiScan II (Gatan, model 788) unit with a Gatan BF detector with time resolution of 0.555 s/frame. The whole *in situ* process was recorded in STEM mode and series of *in situ* images were either extracted from the *in situ* videos or captured every 4 s by blanking the electron beam in between.

6.3.3 *Post situ* and *ex situ* TEM

To confirm mineralization products formed were similar to those formed without the interaction of any electron beam, so-called *ex situ* experiments were performed completely outside of the TEM. To confirm 1 h experiments, mineralization products were acquired by dropping dispersed mineralized solution after 1 h onto carbon-coated TEM copper grids followed by immersion in methanol to halt any further particle development. For the confirmation of products after 3 h under confinement, the same amount of CaP mineralization solution (0.2 µl) was sealed inside the *in situ* TEM liquid cell for 3 h, but not placed under the electron beam. The E-chips were then taken out, washed with methanol to terminate further mineralization, and viewed in the TEM.

After the *in situ* experiment, the E-chips were removed from the liquid TEM holder, separated and then dried for further *post situ* characterization. The *post situ* experiments were conducted sequentially, with XPS performed first (detailed below), and EELS performed after mounting the sample to a molybdenum grid to mount on a standard double-tilt holder. As for all experiments, a JEOL 2010F TEM with the accelerating voltage of 200 kV was employed to characterize the *post -situ* mineralized samples on the dried E-chips, as well as the *ex-situ* mineralized samples above in both TEM and STEM bright field imaging modes, and by STEM-EELS. Principle component analysis (PCA) was used to decrease noise in the Ca elemental distribution EELS map.

6.3.4 X-Ray Photoelectron Spectrometry (XPS)

Both *in situ* mineralized samples on the dried E-chips and *ex-situ* mineralized samples on TEM grids were characterized by an imaging and scanning X-ray photoelectron spectrometer (PHI Quantera Ⅱ, Physical Electronic, MN). The time-dependent *ex-situ* mineralized samples were prepared by spin-coating dispersed mineralized solution onto cleaned silicon wafer substrates and then immersing them in methanol to wash away NaCl. All the selected regions of interest were scanned by monochromated Al Kα (280 eV) with 5 sweeps for 200 micron beam (50 power) and 20 sweeps for 7.5 micron beam (0.8 W power). 55 eV pass energy scanning with 200 micron beam and 120 sweeps was used for the P1s high resolution spectra. Dual beam neutralization was used to prevent samples from charging. Calibration was done by calibrating to a clean piece of silver foil.

6.4 Results and Discussion

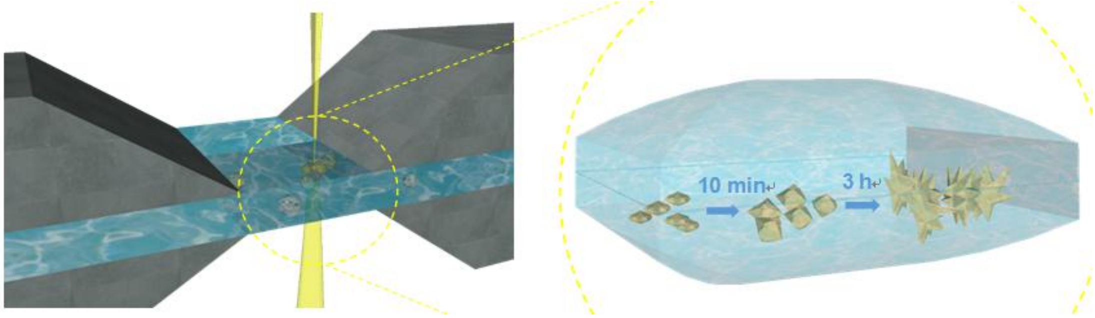

Figure 6.1. Schematic of the *in situ* liquid cell in scanning TEM and CaP mineralization process.

In order to perform real-time imaging inside the TEM, an *in situ* scanning LP-TEM system was used to visualize the mineralization process, as shown in the schematic drawing in Figure 6.1. The *in situ* system, composed of two overlapping silicon nitride membranes on silicon chips, confines a limited amount of solution to form a miniaturized cell. The *in situ* observations were conducted by scanning the focused electron beam across an area of interest where mineralization occurred in a biologically relevant buffer solution, and capturing video of these events.

The free radicals generated through radiolysis of aqueous solution, such as hydrated electrons, $H^{\cdot}$, $OH^{\cdot}$, and so on, can interact with existing active species from solution as reducing and oxidizing agents. These reactions are determined by the concentration of the generated radicals, which are further dependent on the conditions of the microscope and liquid cell, including beam dose rate, solution composition, and temporal and spatial concentration evolution by diffusion and reaction.[90] It has been reported that beam-induced species below a certain concentration result in negligible radiolysis-related reactions.[79] For the system in this study, having a solution with a stable pH of 7.4, a beam dose rate of 21 electrons/frame.nm^2 was identified to reduce the beam effect and maintain sufficient spatial resolution at the same time. Furthermore, the beam dose chosen for this *in situ* study was much lower than the threshold value of beam induced crystallization reported in previous studies[244]. In addition, the presence of a buffer solution may have contributed to the maintenance of a stable pH which helped to reduce the chemically active species interacting with calcium and phosphate ions contained in the solution to produce beam-induced crystals.

The membranes between which liquid is encapsulated have been reported to bulge[245] due to pressure difference between the liquid inside the cell and the vacuum environment in TEM, as shown encircled in Figure 6.1. This bulge contributes to the reduction of the resolution based on an increased thickness of the liquid layer and multiple scattering of the electron beam. In order to reduce the liquid layer thickness and consequently enhance the resolution, the thinnest liquid layer was used (50 nm spacers) and imaging was always preferred at the corner of a liquid cell where the bulging is minimal. In this study, the bottom chip was patterned with micro-wells (400 μm x 200 μm each well), which helped to decrease interference among each individual micro-well by confining the generated radical species to each well.[22, 245, 26] Based on the *in situ* setup shown in Figure 6.1, a series of *in situ* studies were performed and followed by characterization and analysis of the products formed.

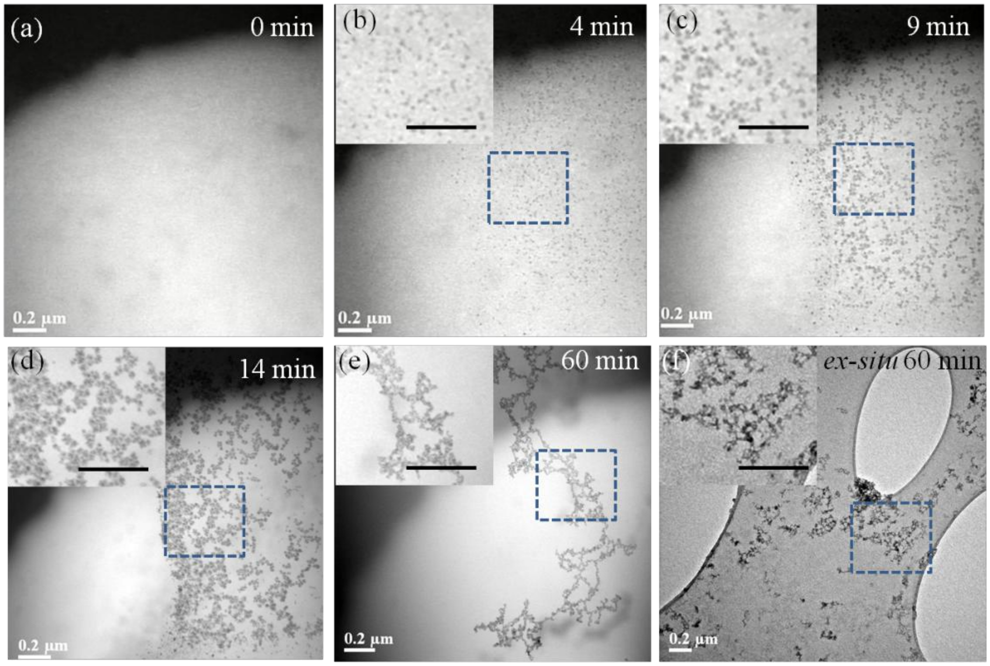

Figure 6.2. *In situ* BF-STEM images showing initial nucleation and growth of CaP over 60 min. a–d, continuous mineralization from 0–14 min, showing the nucleation and growth of CaP particles e, final branched particle morphology after 60 min f, BF-TEM image of ex-situ mineralization with similar resulting particle size and morphology after the same growth time. The scale bars in the insets represent 200 nm.

6.4.1 Real-time observation of the morphological evolution of CaP mineralization

With the help of *in situ* scanning LP-TEM, the CaP nucleation and mineralization process was recorded by bright-field (BF) scanning TEM (STEM) images with time-resolved and nanoscale spatial resolution (Figure 6.2). After a delay of around 2 min, small particles appeared and began increasing in quantity. At around 4 min (Figure 6.2b), these particles were clearly discernable and their average diameter measured 10 nm. These particles had the ability to move and aggregate with each other in solution (Supplementary Video 1). Initially, they aggregated with the nearby particles to randomly generate branched particle assemblies (Figure 6.2c). After the branched assemblies were formed, smaller particles continued to move towards the assemblies and aggregate. With increasing time, these branched assemblies increased in size, and at 14 min aggregated sphere-like particles were obvious (Figure 6.2d). The apparent stacking of the nanoparticles along an imaginary boundary in Figure 2d is a well-known phenomenon in liquid cell microscopy when gas evolution causes a bubble to form in the solution. A liquid meniscus that wets the surface remains, allowing liquid processes to still be recorded. It is clear from the supplemental video that this boundary does not drive the particle aggregation; the particles are moving in all directions. Furthermore, this is only present in one of the datasets and not in the others reported in the manuscript. In order to limit the electron beam dose exposure to the *in situ* mineralization solution, we blocked the electron beam by closing the microscope column and let the *in situ* mineralization continue without electron beam exposure. The column was then reopened, and a single image was taken at 60 minutes (Figure 6.2e), showing the final branched assemblies formed during this time period. We performed a beam-blank comparison to validate that the *in situ* morphology observations were not solely artifacts of the electron beam. A bright-field TEM image of an *ex-situ* synthesized and mineralized sample after 60 minutes is shown in Figure 6.2f with similar particle size and branched assembly morphology.

The initial morphology evolution observed *in situ* agrees well with results of cryo-TEM studies on similar CaP systems.[228,242] In those studies, pre-nucleation clusters of calcium triphosphate ions were proposed to exist as the nanometer-sized building blocks for CaP, which decreased the energy barrier for nucleation. These pre-nucleation precursors can aggregate into branched polymeric structures. However, cryo-TEM investigations can only infer the morphology evolution according to images at segregated time points and is unable to record the dynamic mineralization process. In our *in situ* study, we observed in real-time the nucleation, movement, and morphology evolution of CaP nanoparticles, which provides direct evidence to demonstrate the active mobility of CaP nucleation clusters and supports that CaP mineralizes by particle attachment. It has been suggested that the CaP pre-nucleation precursor is the initial phase formed during the bone mineralization process to be delivered into the extracellular matrix.[231,240] Here, real-time recording with sufficient temporal and spatial resolution showed the active mobility of initial CaP clusters, which also supports the possibility of their movement towards collagen fibrils in aqueous environments for their eventual mineralization. This work lays the foundation for further investigation of the mediating functions of the extracellular matrix, as well as non-collagenous proteins on CaP mineralization *in situ*. It is important to note that the reaction kinetics do match those of previous ex-situ observations, which confirms the electron beam effects are indeed minimal at the selected beam dose rate.

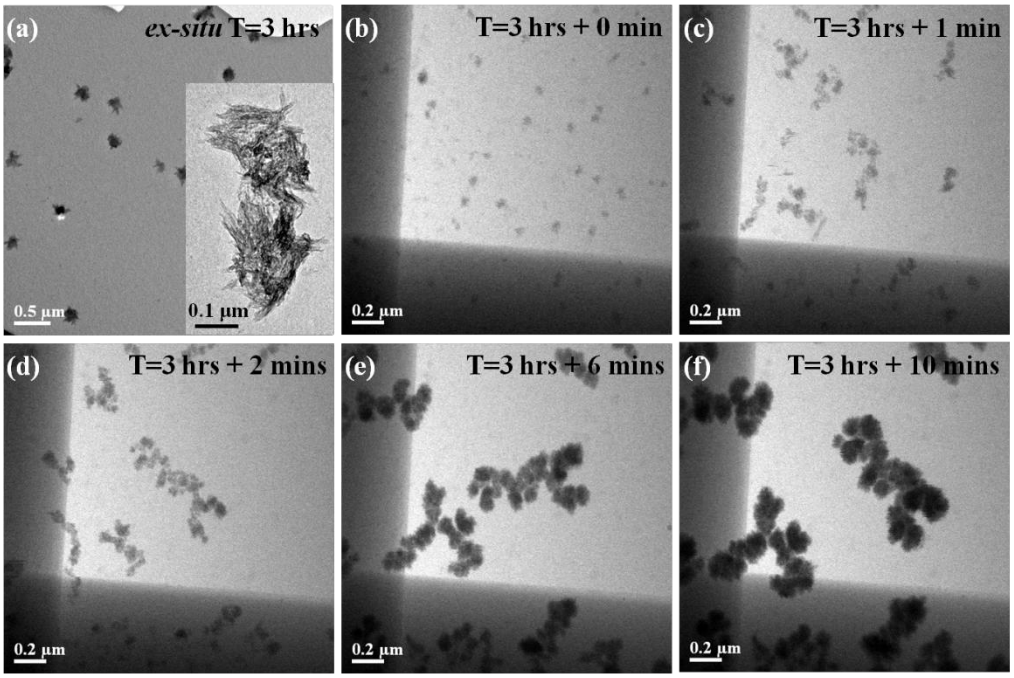

Figure 6.3. CaP growth and morphology after 3 h pre-mineralization. a, BF-TEM images of flake-like particles that resulted after ex-situ mineralization on E-chips without exposure to the electron beam, b–f, corresponding *in situ* BF-STEM images showing CaP growth progression after 3 h, and the growth of dark particles with roughened borders.

In addition to initial nucleation and growth, it is also critical to investigate the particle morphology after longer growth times, since CaP biomineralization involves sequential morphological transformations which could serve as indications of phase changes.[229,230] In *in vitro* CaP mineralization studies, the morphology of ribbon-like structures was observed after 3 hours[229,247], also noted here in a similar *ex-situ* experiment of Figure 6.3a flake-like particles developed. This phase of CaP mineralization was also studied here by another representative *in situ* TEM experiment shown in Figure 6.3. In this experiment, the silicon nitride microchips patterned with discrete micro-wells were used. After 3 hrs the electron beam was moved to a new micro-well that had not experienced electron beam exposure and the images in Figure 6.3b-f were captured. This enabled the capture of mineralization events after the initial nucleation and growth period. While this approach assumes that the liquid is confined to each separate micro-well, and therefore, at time t=3hrs represents growth that was not beam induced, recent works have shown that radiolysis products are largely beam-confined[90] and unlikely to effect a neighboring micro-well. Now, sphere-shaped aggregates that were larger than those formed during initial nucleation under electron beam exposure at time zero were observed (Figure 6.3b), which during further real-time TEM imaging (Figure 6.3c-f), grew into aggregated assemblies (Figure 6.3c) with roughened borders arising from their needle-like nature, which grew darker (Figure 6.3d), and larger while they rotated within the liquid (Figure 6.3e, f). After around 6 minutes, the aggregates still had the ability to move by rotation in the liquid, and by 10 minutes further darkened and grew slightly due to what appears to be conventional crystal growth. Since the particle morphology from *ex-situ* experiments, shown in Figure 6.2f and 6.3a, so closely matches the events shown *in situ* after 1 hr and 3 hrs, respectively, we can assume that the beam effects on the mineralization pathway are not substantial.

Based on our real-time *in situ* investigation of this dynamic process, the early mineralization of CaP can be divided into several stages. Initially, nanoscale particles appeared after around 2 minutes, these continued to aggregate to form branched assemblies within 1 hr. In other works, these assemblies were proposed to directly assemble into ribbon aggregates[229]. Here, we see this transformation after 3 hrs, where the formation of similar needle-like aggregates occurs by particle attachment, and subsequent continued growth takes place by seemingly conventional methods.

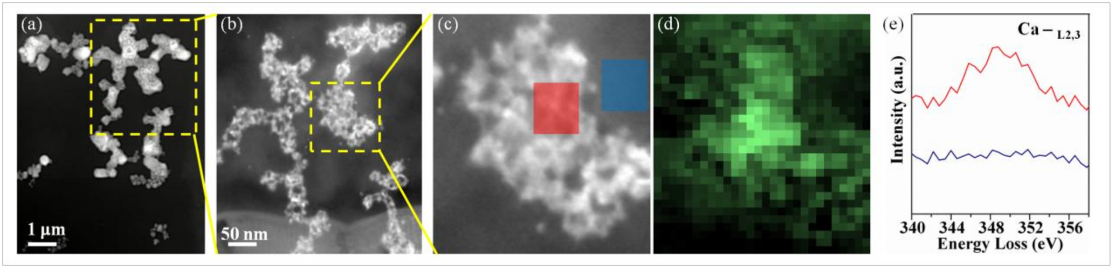

Figure 6.4. *Post situ* characterization of the *in situ* synthesized particles. a–c, HAADF STEM images of a, the *in situ* region of interest and b, the same area once the silicon nitride microchips have been opened, and shown at c, higher magnification and as d, an EELS Ca-map as extracted from the *post situ* e, EELS spectra of the Ca-$L_{2,3}$ edge which demonstrates these particles are Ca-based. The Ca $L_{2,}$3-edge was identified inside mineralized particles (red), and absent in the surrounding regions (blue).

6.4.2 *Post situ* correlative chemical composition analysis

Due to the relatively thick liquid layer in LP-TEM compared to conventional TEM specimens, spectroscopy characterization *in situ* is a challenge. Here, we exploited several so-called *post situ*, or post *in situ* correlative spectroscopy characterization approaches to probe the mineralization products, specifically X-ray photoelectron spectroscopy (XPS) and electron energy loss spectroscopy (EELS) on the removed *in situ* chips. This is an essential experiment to validate that the products formed in the microscope are the same products that would form in the absence the electron beam. After the *in situ* experiment presented in Figure 6.1, the silicon nitride microchips were removed from the liquid TEM holder and dried for *post situ* characterization *via* XPS. XPS (Supplementary Figure 6.1) showed the existence of Ca and P, and the high-resolution spectrum of P contains the peak at 133.89 eV which matches with the photoelectron line of P in CaP. In addition, the quantitative elemental ratio of XPS analysis showed the Ca/P is ~0.67, which has a nice agreement with the calculated Ca/P ratio range of 0.55 to 0.75 in other studies[229]. This same sample was then probed by EELS, where Figure 6.4a and b highlight the region of interest *in situ* and after drying, respectively. An EELS spectrum image (Figure 6.4d) and extracted Ca-$L_{2,3}$ edges (Figure 6.4e) confirm the presence of Ca inside mineralized particles and absence in the surrounding regions which demonstrates these particles are Ca-based. The correlative *post situ* chemical analyses by XPS and EELS provide strong evidence that the *in situ* mineralized particles are CaP-based. Also, the Ca/P ratio from the XPS quantitative data reported as 0.67 from the one-hour *in situ* mineralized sample suggests that the phase of these branched assemblies is not amorphous calcium phosphate (ACP) whose Ca/P ratio is 1.5. ACP was considered as the nanometer-sized building blocks of CaP in other studies.[229] Due to the large liquid layer, and small particle size, obtaining a reliable diffraction pattern *in situ* to determine the exact phase of the CaP formed was not possible.

6.5 Conclusions

For the first time, the real-time observation of CaP mineralization was recorded, which is a direct demonstration that CaP initially mineralizes by particle attachment. Complementary *in situ*, *post situ* characterization and *ex-situ* beam-blank experiments were designed to support this claim. According to *post situ* TEM-EELS and XPS analysis, the *in situ* mineralized particles were confirmed to be CaP-based. The samples mineralized in *ex-situ* beam-blank experiments follow similar morphologies as *in situ* samples, which validates that the *in situ* morphological observations were not solely artifacts of electron beam dose. This study lays the foundation for further investigation of

CaP biomineralization involving more complex organic-inorganic physiological interactions. This paper presents the first use of liquid-phase *in situ* TEM on a calcium phosphate mineralization system. The approach we show not only provides concrete answers to questions in the field of crystallization such as, the sequence of precursor formation, aggregation and crystal formation, but also demonstrates the feasibility of investigating biological processes in buffer solutions, which can be used on a variety of biological and mineral research in the future.

6.6 Acknowledgements

K.G. acknowledges financial support from the Discovery Grant program of the Natural Sciences and Engineering Research Council of Canada (NSERC). L.S. acknowledges financial support from the Natural Sciences and Engineering Research Council of Canada and the Canada Research Chair program. X.W. acknowledges support from the Ontario Trillium Scholarship. Electron microscopy was performed at the Canadian Centre for Electron Microscopy (CCEM), a facility supported by NSERC and other governmental agencies. Gianluigi Botton, scientific director of the CCEM, is gratefully acknowledged for his continued support and guidance.

6.7 Supplementary information

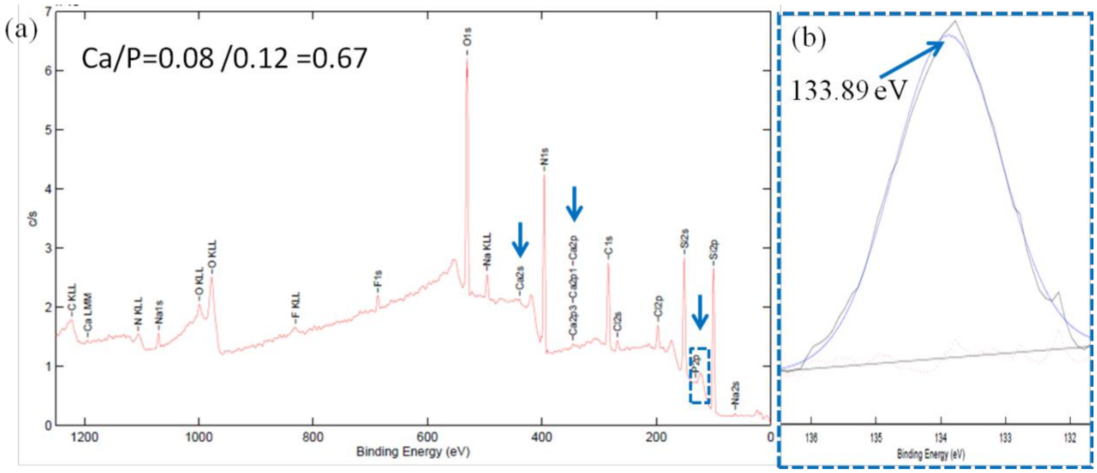

Figure S6.1.The *in situ* synthesized particles are characterized by *post situ* XPS. The deconvoluted P high energy resolution peak matches with the photoelectron line of 2p3/2 of P.

Chapter 7 Summary, Conclusions, Limitations, Future Work, and References

Chapter outline

In this chapter, the findings of this thesis work are summarized and the impact they will have on the characterizations of dynamic processes involving nanomaterials are discussed. Next, the limitations of the current work are presented and future work that builds on these findings is proposed.

7.1 Thesis Summary

The objective of this work was to: apply an *in situ* TEM system to study the nucleation and growth mechanism of nanostructures, investigate the effect of electrochemical conditions on the structural evolution of nanostructures through electrodeposition and electrochemical cycling, and extend the *in situ* technique to study biological processes such as biomineralization.

The *in situ* studies began with an examination of the electron beam effect, and then an optimization of the *in situ* system was performed for studying the structural evolution of nanomaterials in electrochemical and biomineralization processes. Analyses were conducted by combining *in situ* characterization techniques for visualizing the formation of different morphologies and *post situ* characterization techniques to identify the structure and composition of the structures. The in situ techniques used were *in situ* electrochemical measurements and *in situ* scanning transmission electron microscopy (STEM). *Post situ* techniques used were scanning electron microscopy (SEM), electron energy loss spectroscopy (EELS), energy-dispersive x-ray spectroscopy (EDS), and X-ray photoelectron spectroscopy (XPS).

Using the above the methods, the electrodeposition of gold on carbon electrode was studied, quantitative analysis on the growth process was conducted to describe the growth process by examining the classical Scharifker-Hills growth model. Electrodeposition of palladium on carbon electrode was studied, the self-limited, surface diffusion and aggregation model was used to describe the early stage of growth process. Furthermore, electrochemical cycling was applied to study the growth, dissolution, movement and aggregation of palladium nanostructures under different potentials. The effect of supporting electrolyte (HCl) on the electrodeposition and electrochemical cycling of palladium nanostructures was analyzed. Finally, *in situ* biomineralization process was studied to provide direct experimental proof on the non-classical pre-nucleation and attachment growth model of calcium phosphate formation.

We have demonstrated that the *in situ* technique provides direct experimental evidence valuable for the studies of different dynamic processes at the nanoscale. It also facilitates the use of quantitative analysis on the growth rate, cluster density and distribution and the amount of formed nanostructures for understanding the mechanisms involved in these dynamic processes, which provides insights into the development and applications of nanostructured materials.

7.2 Thesis Conclusions

1) *In situ* microscopy enables the capture of images with high spatial resolution of a few nanometers while dynamic processes are in progress. We have shown that the miniaturized liquid cell used for *in situ* TEM is capable of emulating the dynamic processes occurring under their actual conditions after various optimizations. These optimizations involve varying the electrochemical and microscopy imaging conditions including the imaging mode, electron beam dose rate, fluid rate and liquid thickness.

2) The electrochemical deposition process examined during an *in situ* observation is affected by the electron beam by showing accelerated growth on the electrode or crystal growth on non-conductive silicon nitride membrane. The experimental conditions determine the mechanism and degree of interference by the electron beam and how it affects the structural evolution of nanoparticles. To minimize the beam effect, a common method is to decrease the beam dose rate below a threshold value. We have discovered that increasing the thickness of the liquid is an effective method to minimize the beam impact. Through our studies, we demonstrated that there are morphological, density and distribution differences between the beam-induced and electrodeposited crystallites. We observed beam-induced gold crystals with the morphology of diffusion-limited aggregates confined in beam scanned area on the silicon nitride membrane, with its total amount (about two orders-of-magnitude) smaller than electrodeposited crystals on the working electrode.

3) The optimized *in situ* TEM system was applied to study the electrodeposition of gold nanostructures. The growth of gold crystallites was quantitatively analyzed based on the acquired current time transients and *in situ* images. By fitting the results to the commonly

used classical Scharifker-Hills growth model, we found that the model only accurately describes the diffusion-limited three-dimensional multiple nucleation growth process after electrodeposition duration of 3s. Heterogeneous deposition was also found using *post situ* SEM. There was enhanced deposition along the electrode edge, which explained the discrepancy of the amount of deposits observed *in situ* and that measured using the current time transient.

4) In addition to gold deposition, we also studied the nucleation and growth mechanism of palladium electrodeposited on a carbon substrate in palladium salt solution (H_2PdCl_4) with and without HCl using chronoamperometry. Based on the acquired current time transients and the *in situ* images, an aggregative growth model was found to better describe the electrodeposition process, rather than the commonly applied Volmer-Weber 3D island growth model based on direct adatom addition. This aggregative growth mode at the early stages of growth includes the self-limiting growth, surface diffusion, aggregation and recrystallization of nanoparticles which act as building blocks of the deposits. The effect of HCl as a supporting electrolyte for nucleation and growth of palladium through electrodeposition process and beam-induced process have also been studied. HCl was found to hinder the recrystallization of aggregated palladium nanoclusters. Furthermore, adding HCl resulted in aggregated structures with a dendritic morphology, in comparison to the smooth spherical nanoparticles from solution without HCl. Moreover, HCl also affected the growth process under the combination of the electron beam and electrodeposition. The *in situ* observation demonstrated that in a palladium salt solution without HCl, electron beam induced palladium formation was

found on the nonconductive silicon nitride membrane adjacent to the electrode which was not found in the case with HCl.

5) Besides chronoamperometry, cyclic voltammetry was used to study the role of HCl in palladium structural evolution under potential cycling. The in situ CV profiles form solutions with and without HCl showed characteristics of reduction, oxidation, hydrogen adsorption/absorption/evolution and hydrogen desorption associated with palladium. Rapid growth was observed at reduction peaks in both solutions. However, HCl induced enhanced dissolution of palladium during oxidation process. Movements and aggregations of the palladium clusters during hydrogen adsorption/absorption/evolution and hydrogen desorption processes was only observed in solution with HCl, possibly due to the defects generated during the phase transformation of Pd-H structures. The morphology of the palladium nanostructures formed after *in situ* CVs were also compared. Smooth spherical structures were observed from the solution without HCl, whereas chain-like structures and irregular aggregates were found from the solution with HCl. We proposed that the formation process of these chain-like structures and irregular clusters were dominated by the aggregation of pre-grown particles during the hydrogen adsorption/absorption/evolution and desorption processes.

6) The *in situ* TEM system was used to study the mechanism of calcium phosphate mineralization in a solution simulating human/vertebrate body fluid. It was found that calcium phosphate initially mineralized by particle attachment, and then aggregated to form branched assemblies. For long growth time, the *in situ* observation has shown that the assemblies followed the conventional growth methods of direct assembly into ribbon

aggregates. The *post situ* TEM-EELS, XPS analysis and *ex situ* control experiments further confirmed that mineralized particles are CaP-based.

7) The *in situ* TEM has shown to be an efficient technique to study intermediate reactions and products during various processes. The combination of *in situ* observation with *ex situ* and *post situ* characterization techniques provides essential and invaluable insights into the complex phenomena occurring in different dynamic processes.

7.3 Contribution to the Field

This work contributes to the field of *in situ* electron microscopy by providing the following.

1) A protocol for optimizing *in situ* TEM system for the study of dynamic processes

The study of electron beam interference with electrodeposition provides an approach to evaluate the structural evolution of nanomaterials caused by the electron beam, electrodeposition, and their coupling effect. The comparison of results from *post situ* characterizations with those of standard *ex situ* experiments provides a platform to decouple the electron beam effect from electrodeposition processes. This will allow researchers to investigate different intrinsic dynamic processes using the *in situ* system. Furthermore, the experimental procedures used in this work to decrease electron beam induced growth show more controllability over the imaging conditions for *in situ* studies.

2) A validation and modification of hypotheses on mechanism of structural evolution of nanomaterials through electrochemical processes

In this work, the *in situ* study of gold and palladium electrodeposition, as well as palladium nanostructures under potential cycling have provided direct experimental data of the structural evolution of nanomaterials during nucleation, growth, and dissolution, aggregation and hydrogen contribution to the process. The data provided verification of the existing Volmer-Weber 3D island growth mode (Scharifker-Hills model) for long time growth of gold and palladium, and with modification on the initial stage of palladium electrodeposition where self-limiting, surface diffusion and aggregation growth dominates the process. This work shows that the *in situ* technique is capable of probing intermediate products during complex electrochemical processes.

3) An *in situ* study for biological processes

The *in situ* study of calcium phosphate biomineralization process has shown that the formation mechanism of nanomaterials during its early stage in simulated body fluid. This work will enable researchers to study other biological processes involving organic and inorganic physiological interactions.

7.4 Future Work

These sections address some of the remaining challenges and possible future directions of this work in terms of the *in situ* characterization technique and its application to fundamental studies and theoretical modeling. These possible directions involve defining research problems that encompass many fields, including microfabrication, nanotechnology, electrical engineering, materials engineering, chemistry, and biochemistry.

7.4.1 Development of *in situ* technique

The *in situ* TEM technique has already contributed to various fields of study by providing real time high resolution imaging, but since this is a newly developed technique, there is still some space to improve its functionalities.

The improvement of the design of *in situ* TEM systems can lead to benefits in three main areas: controlling the electron beam effect with changes to the liquid cell design, overcoming resolution limitations, and integrating multiple functionalities within the liquid cell. These are discussed in the following sections.

1) Improving the liquid cell design

As discussed in chapter 2, reducing the electron beam interference for the dynamic process under study is an essential step, except when exploiting electron beam to induce growth, dissolution, assembly or movement of nanostructures. To achieve this, several improvements can be considered in terms of the liquid cell design. For example, some modification can be done for the liquid cell with sandwich structure. Silicon nitride is commonly used to isolate the electrodes fabricated on the silicon chip, but the silicon nitride membrane on both chips will be charged by electron beam during the *in situ* observation leading to extra physical/chemical changes. Conductive materials can be used as an alternative choice to overcome this limitation. For example, graphene has been be used to seal samples in liquid for TEM[54,55]. For studies of electrochemistry or heating, the membrane on the top chip can be partly or fully replaced with graphene. The robustness of the graphene film should be considered, and the thickness should be optimized.

2) Resolution limitation

The resolution for imaging through liquid has yet to reach the atomic level. This is very important for studies on the initial stage of structural evolution, for example, the nucleation of electrochemical processes. There are several factors that determine resolution: beam dose rate, spacer thickness, and bulging of the membranes. As discussed in chapter 2, there is always a need to balance the contribution from these factors. In STEM mode used in this thesis, the imaging conditions provides the best resolution on the top chip. Therefore, if the microelectrodes are on the top chip, the resolution will be greatly improved. The liquid thickness can also be decreased to give higher resolution. There is a 500 nm spacer on the bottom E-chip which will contribute to the liquid thickness. Reducing the thickness of the spacer is another way to decrease the liquid thickness. In general, the improved design of the *in situ* system with better control over the electron beam effect and resolution will contribute greatly to understanding dynamic processes at the nanoscale.

3) Multiple functionalities

The liquid holder integrated with electric circuits can realize either electrochemical or heating function independently. The next step is to integrate these two functions into one system so that the effect of temperature on electrodeposition processes can be studied. In addition, there are different phases involved in some of the biochemical and electrochemical processes to be studied. Thus, besides the study of dynamic processes in the liquid, or at the liquid-solid interface, the observation of processes at the liquid-gas or liquid-solid-gas interface is also very important. Some examples of these processes are soft tissue degradation, corrosion and catalytic process involving fuel cells. An idea is to incorporate gas circulation into the *in situ* TEM liquid cell to study the processes occurring at the liquid-gas-solid interface.

7.4.2 Applications

There are also a multitude of new applications that can be explored in the future, and here some of these possible examples are suggested.

7.4.2.1. Electrochemical processes

1) Mechanism of nucleation and growth during electrodeposition

The *in situ* study of electrodeposition of gold, in chapter 3, and palladium, in chapter 4, has mainly analyzed the growth of gold and palladium crystals on carbon electrodes using chronoamperometry. The nucleation process still lacks direct experimental evidence due to the limited spatial and temporal resolution of the *in situ* technique. The nucleation and growth processes can be studied separately using potentiostatic double pulse deposition. This electrochemical technique applies high *overpotential* for a short duration of time which initiates the nucleation process and then a low *overpotential* for the growth process. During the nucleation process, the active species at the electrode surface are rapidly depleted. In a short time, without supplies of the species from the bulk solution, the density of the nuclei on the substrate is supposed to remain the same. The double pulse technique separates the nucleation and growth processes, allowing the control of the nucleation density and subsequent sizes independently through varying the conditions of the two steps. Using this technique, the nucleation rate, distribution, and density can be quantitatively analyzed and the relationship between nucleation/growth and morphology formation mechanism can be studied.

The self-limiting growth, surface diffusion, aggregation and recrystallization processes discussed in chapter 4 should be further investigated by controlling the applied potential and electrolyte concentration. Figure 7.1 shows the early stage of gold deposition on a carbon electrode from a decreased concentration under a typical *overpotential* used to fabricate gold nanostructures for biosensors. During the early stage of the deposition, from image (b) to (c), we observed movement and disappearance of nanoparticles under 10 nm as circled around particles P_2, P_3, P_4 and P_7. For longer deposition time, the movement of large particles of 15 nm to 20 nm was seen, such as P_1, P_5 and P_6. Due to the limitation of temporal resolution, the attachment process of the particles below 10 nanometers was not captured, but as a start, the movement of deposits on low energy surface has been observed, and the following control experiments indicated that the electron beam did not induce particle formation or movement under the same condition without electrochemical potentials. For in-depth investigations, systematic *in situ* electrodeposition and control experiments with increased temporal resolution can be performed within shorter deposition times.

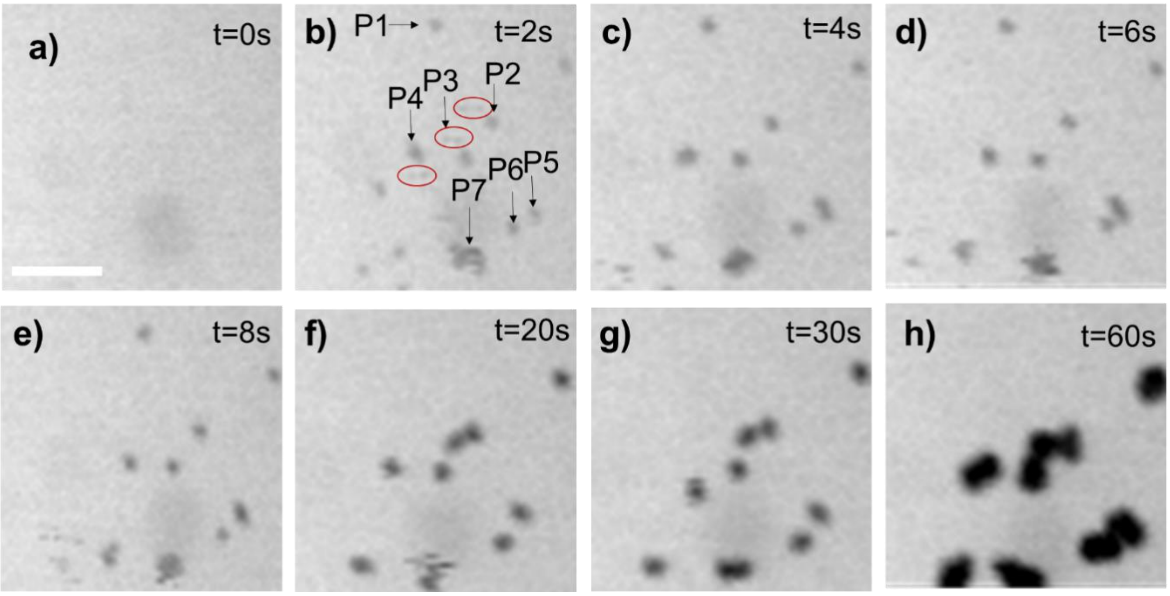

Figure 7.1. *In situ* bright-field STEM images showing electrodeposition of gold nanoparticles on carbon electrode under -0.2V (vs. Ag/AgCl reference electrode) in 0.5 mM $HAuCl_4$ in 0.1 M HCl. Scale bar represents 50nm.

2) Development of desired surface morphology with optimized conditions

It has been reported that electrodeposited palladium with different degrees of nanotexturing can be obtained by simply varying the applied potential and concentration of supporting electrolyte[2]. These conditions could be investigated using the *in situ* TEM system, and a comprehensive study on the effect of the deposition conditions could be conducted. Based on the mechanism of electrodeposition, desired surface morphology could be developed by electrodeposition by controlling the electrochemical conditions.

7.4.2.2. Bio-sensing process

Affinity-based nucleic acid detection has shown advantages such as portability, low cost, and rapid analysis in applications like health monitoring, disease diagnosis, and drug discovery[248]. In this technique, nanostructured surfaces are modified with bio-recognition layers and integrated with different readout methods to produce a biosensor[248,249]. The motivation of this thesis comes from the study that shows different nanostructured surfaces demonstrate different sensitivity during nucleic detection[2]. Based on the gold or palladium nanostructured substrate fabricated by electrodeposition, the binding interaction between complementary nucleic sequences will be observed and studied *in situ*.

The first step would be to visualize the probe single strand DNA, or RNA (oligonucleotides). The most applied method is to use gold nanoparticles (AuNP) to label them. The development of Au nanoparticle labeled oligonucleotide/single strand DNA (AuNPs-DNA) is a significant development and has been applied in the field of clinical diagnosis[250,251]. Then the deposition of thiolated DNA probes on these different nanostructured substrates could be studied to evaluate the binding efficiency of these substrates. The commercially available oligonucleotide containing a thiol group at the 5’ and amino group at 3’ could be used. The amino group binds with carboxyl-modified AuNPs to form DNA-AuNPs with the free thiol group at the 5’ which binds with the surface of the gold/palladium substrate. These DNA-AuNPs will be flowed into the liquid cell and their adsorption to the nanostructured surface will be observed. The hybridization of nucleic acid probes with complementary sequences will be studied *in situ*. The target sequence labeled with AuNPs will be flowed at a constant rate to the gold/palladium nanostructured substrate immobilized with oligonucleotides with probe sequence, the hybridization process will be observed through the attachment of gold nanoparticles. Challenges include optimizing the flow conditions and decreasing non-specific adsorption. Systematic control experiments are needed including the investigation of electron beam damage to the DNA-AuNPs.

7.4.2.3. Biological processes

The *in situ* technique has enabled researchers to study biological processes as shown in chapter 6. Besides the *in situ* imaging of metal crystals, the imaging of dynamic processes involving protein, DNA, cellulose, etc, are of great importance in many research fields. In these studies, it is challenging to reduce sample damage, and keep the liquid environment similar to their native environment. Any changes caused by the electron beam, as discussed in chapter 2, including the temperature and pH of the liquid, generation of active species, and their interaction with the biological process, should be investigated. Figure 7.2 shows the *in situ* imaging of DNA amplification process.

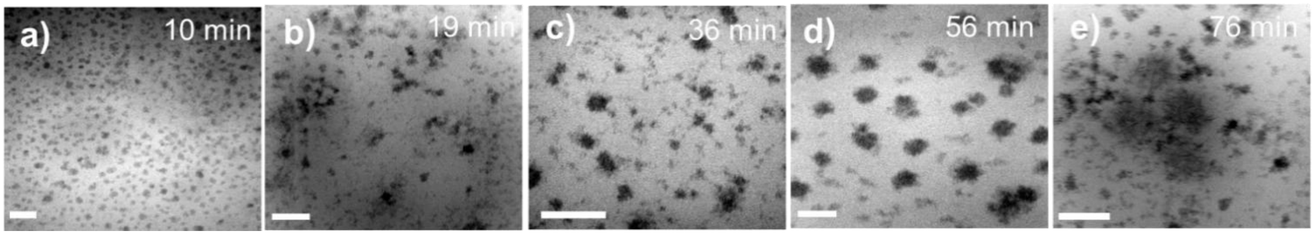

Figure 7.2. *In situ* bright field STEM images taken at different stages during the DNA formation process, from (a) to (e) show the structural evolution of 3D DNA structures at different time points.

This *in situ* TEM technique can be further explored for use in other biological processes to provide direct experimental proof for the mechanism involved in these processes.

7.4.3 Fundamental studies

The *in situ* technique has shown great potential to study various dynamic processes. In order to perform the experiments effectively and conduct proper analysis, further fundamental studies of the *in situ* system should be conducted to understand in more depth how the electron beam affects different dynamic processes. An example of such studies would be the modeling of electrodeposition process inside the *in situ* TEM system. As shown in chapter 4, the electric field distribution on the surface of the micro-electrode during *in situ* electrodeposition explained the heterogeneous growth of palladium nanostructures on the microelectrode. More precise modeling should be carried out by considering the actual electrochemical conditions. One of such conditions is the electron beam that affects the double layer formation process, electric field distribution inside the liquid cell, local temperature change, electrolyte potential and pH, and concentration of reactive species change. This holistic modeling would significantly help researchers design and predict *in situ* experiments.

References

1 L. P. Bicelli, B. Bozzini, C. Mele and L. D'Urzo, *Int. J. Electrochem. Sci.*, 2008, **3**, 356–408.

2 L. Soleymani, Z. Fang, E. H. Sargent and S. O. Kelley, *Nat. Nanotechnol.*, 2009, **4**, 844–848.

3 E. Antolini, *Energy Environ. Sci.*, 2009, **2**, 915.

4 E. Environ, X. H. Liu and J. Y. Huang, *Energy Environ. Sci.*, 2011, **4**, 3844–3860.

5 K. L. Klein, I. M. Anderson and N. De Jonge, *J. Microsc.*, 2011, **242**, 117–123.

6 A. A. Gewirth, B. K. Niece, B. Platinum, F. Copper, G. Nickel, B. Platinum, B. Silver, B. Steel and C. Aluminum, *Chem.Rev.*,1997, **97**, 1129−116.

7 N. Borisenko, S. Z. El Abedin and F. Endres, *J. Phys. Chem. B.,* 2006, **110**, 6250-6256.

8 L. A. Kibler, A. Cuesta, M. Kleinert and D. M. Kolb, *Journal of Electroanalytical Chemistry,* 2000, **484**, 73–82.

9 T. Teshima, K. Ogaki and K. Itaya, *J. Phys. Chem. B.,*1997, **5647**, 2046–2053.

10 T. Suzuki, T. Yamada and K. Itaya, *J. Phys. Chem. B.,* 1996, **3654**, 8954–8961.

11 M. E. Hyde, R. Jacobs and R. G. Compton, *J. Phys. Chem. B.,* 2002, **106**, 0–5.

12 J. J. De Yoreo, S. Chung and R. W. Friddle, *Adv. Funct. Mater.,* 2013, 2525–2538.

13 J. Y. Huang *et al, Science.,* 2010, **330,** 1515–1521.

14 P. L. Gai, *Microsc.Microanal.*, 2017, **8**, 21–28.

15 L. L. Dai, R. Sharma and C. Wu, *Langmuir*, 2005, **21**, 2641–2643.

16 S. Chen, K. Kobayashi, R. Kitaura, Y. Miyata, H. Shinohara, *ACS Nano*, 2011, **5**, 4902–4908.

17 D. Chen, S. Indris, M. Schulz, B. Gamer and R. Mönig, *J. Power Sources*, 2011, **196**, 6382–6387.

18 H. Liao, Y. Shao, C. Wang, Y. Lin and Y. Jiang, *Mater. Lett.*, 2014, **116**, 299–303.

19 Z. Yang, J. Xiao, S. Thevuthasan and D. R. Baer, *Nano Lett.,* 2011, **11**, 1874–1880.

20 R. M. Glaeser, *Biophys. J.*, 2012, **103**, 163–164.

21 B. Scharifker and G. Hills, *Electrochem. Acta*, 1983, **28**, 879–889.

22 P. I. Number, P. E. R. Site, W. Diffusion and O. F. A. Sites, *J Electroanal*

Chem., 1984, **177**, 13–23.

23 M.V.Mirkin and A.P.Nilov, *J. Electroanal. Chem.,* 1990, **283**, 35–51.

24 L. Heerman and A. Tarallo, *J. Electroanal. Chem.,*1999, **470**, 70–76.

25 A. Bewick, M. Fleischma and H. R. Thirsk, *Trans. Faraday Soc.*, 1962, **58**, 2200-2216.

26 J. Ustarroz, J. A. Hammons, T. Altantzis, A. Hubin, S. Bals and H. Terryn, *J. Am. Chem. Soc.*, 2013, **135**, 11550–11561.

27 J. Ustarroz, X. Ke, A. Hubin, S. Bals and H. Terryn, *J. Phys. Chem. C*, 2012, **116**, 2322–2329.

28 E. Budevski, G. Staikov and W. J. Lorenz, *Electrochim. Acta*, 2000, **45**, 2559–2574.

29 E. Alfonso, J. Olaya and G. Cubillos, *Crystallization - Science and Technology*, 2012, DOI:10.5772/35844.

30 N. Elgrishi, K. J. Rountree, B. D. McCarthy, E. S. Rountree, T. T. Eisenhart and J. L. Dempsey, *J. Chem. Educ.*, 2018, **95**, 197–206.

31 A. J. Bard and L. R. Faulkner, *Electrochemical methods- Fundamentals and Applications*, New York: Wiley, 1944.

32 L. Pilon, H. Wang and A. d'Entremont, *J. Electrochem. Soc.*, 2015, **162**, A5158–A5178.

33 A. J. Bard and L. R. Faulkner, *Electrochemical methods- Fundamentals and Applications (second edition)*, New York: Wiley, 2001.

34 G. J. Hills, D. J. Schiffrin and J. Thompson, *Electrochim. Acta*, 1974, **19**, 657–670.

35 M. Sluyters-Rehbach, J. H. O. J. Wijenberg, E. Bosco and J. H. Sluyters, *J. Electroanal. Chem.*, 1987, **236**, l-20.

36 M. Tokuyama and Y. Enomoto, *Physica,* 1995, **220**, 261–276.

37 B. R. Scharifker, *J. Electroanal. Chem.,* 1998, **458**, 253–255.

38 P. A. Bobbert, M. M. Wind and J. Vlieger, *Physica*, 1987, **146A**, 69–88.

39 A. Milchev, S. W. Kruijt, M. Sluyters-Rehbach and J.H. Sluyters, *J. Electroanal. Chem.,* 1993, **362**, 21–31.

40 S. Fletcher, *J. Electroanal. Chem.*, 1986, **215**: l-9.

41 A. Milchev, *J. Electroanal. Chem.,* 1998, **457**, 35–46.

42 S. Fletcher, *J. Electroanal. Chem.,* 2002, **530**, 105–107.

43 S. Fletcher, *J. Electroanal. Chem.,* 2002, **530**, 119–122.

44 H. L. Xin and H. Zheng, *Scinece*, 2012, 10–14.

45 L. M. Plyasova, I. Y. Molina, A. N. Gavrilov, S. V. Cherepanova, O. V. Cherstiouk, N. A. Rudina, E. R. Savinova and G. A. Tsirlina, *Electrochim. Acta*, 2006, **51**, 4477–4488.

46 T. Katsuyama, M. Aziz, *Handb. Chem. Phys.*, 2007, 732–735.

47 Y. R. Kim, S. C. S. Lai, K. McKelvey, G. Zhang, D. Perry, T. S. Miller and P. R. Unwin, *J. Phys. Chem. C*, 2015, **119**, 17389–17397.

48 G. Jerkiewicz, *Electrocatalysis*, 2010, **1**, 179–199.

49 M. Grdeń, M. Łukaszewski, G. Jerkiewicz and A. Czerwiński, *Electrochim. Acta*, 2008, **53**, 7583–7598.

50 A. Zalineeva, S. Baranton, C. Coutanceau and G. Jerkiewicz, *Langmuir*, 2015, **31**, 1605–1609.

51 C. Hsu, M. Wei, Z. Wei and F. Liu, *RSC Adv.*, 2016, **6**, 24645–24650.

52 R. E. White, M. Mecklenburg, B. Shevitski, S. B. Singer, and B. C. Regan. Langmuir 2012, **28**, 3695−3698.

53 K. Nishijima, J. Yamasaki, H. Orihara and N. Tanaka, *Nanotechnology*, 2004, **15**, S329-S332.

54 J. M. Yuk, J. Park, P. Ercius, K. Kim, D. J. Hellebusch, M. F. Crommie, J.Y. Lee, A. Zettl, A. P. Alivisatos, *Science,* 2012, 61–65.

55 N. Mohanty, M. Fahrenholtz, A. Nagaraja, D. Boyle and V. Berry, *Nano Lett.*, 2011, 1270–1275.

56 M. J. Williamson, R. M. Tromp, P. M. Vereecken, R. Hull and F. M. Ross, *Nat. Mater.*, 2003, **2**, 532–536.

57 K.-L. Liu, C.-C. Wu, Y.-J. Huang, H.-L. Peng, H.-Y. Chang, P. Chang, L. Hsu and T.-R. Yew, *Lab Chip*, 2008, **8**, 1915–1921.

58 A. Radisic, P. M. Vereecken, P. C. Searson and F. M. Ross, *Surf. Sci.*, 2006, **600**, 1817–1826.

59 A. Radisic, F. M. Ross and P. C. Searson, *J. Phys. Chem. B*, 2006, **110**, 7862–7868.

60 A. Radisic, P. M. Vereecken, J. B. Hannon, P. C. Searson and F. M. Ross, *Nano Lett.*, 2006, **6**, 238–242.

61 H. M. Zheng, R. K. Smith, Y. W. Jun, C. Kisielowski, U. Dahmen and A. P. Alivisatos, *Science*, 2009, **324**, 1309–1312.

62 H. Zheng, S. A. Claridge, A. M. Minor, A. P. Alivisatos and U. Dahmen, *Nano Lett.*, 2009, **9**, 2460–2465.

63 T.W. Huang S.Y. Liu, Y.J. Chuang, H.Y. Hsien, C.Y. Tsai, Y.T. Huang, U. Mirsaidov, P. Matsudaira, F.G. Tseng, C.S. Chang and F.R. Chen., *Lab Chip*, 2012, **12**, 340–347.

64 S. Brems, M. Hauptmann, E. Camerotto, E. R. White, M. Mecklenburg, S. B. Singer, S. Aloni and B. C. Regan, *Appl. Phys. Express*, 2011, **4**, 055201.

65 J. M. Grogan, N. M. Schneider, F. M. Ross and H. H. Bau, *J. Indian Inst. Sci.*, 2012, **92**, 295–308.

66 J. M. Grogan and H. H. Bau, *J. Microelectromechanical Syst.*, 2010, **19**, 885–894.

67 X. Chen, K. W. Noh, J. G. Wen and S. J. Dillon, *Acta Mater.*, 2012, **60**, 192–198.

68 M. Gu, L. R. Parent, B. L. Mehdi, R. R. Unocic, M. T. Mcdowell, R. L. Sacci, W. Xu, J. G. Connell, P. Xu, P. Abellan, X. Chen, Y. Zhang, D. E. Perea, J. E. Evans, L. J. Lauhon, J. Zhang, J. Liu, N. D. Browning, Y. Cui, I. Arslan and C. Wang, *Appl. Surface Science.,* 2018, **427**, 1064–1070.

69 N. de Jonge, N. Poirier-Demers, H. Demers, D. B. Peckys and D. Drouin, *Ultramicroscopy*, 2010, **110**, 1114–1119.

70 E. a Ring and N. de Jonge, *Microsc. Microanal.*, 2010, **16**, 622–629.

71 N. De Jonge, D. B. Peckys, G. J. Kremers and D. W. Piston, *Proc. Natl. Acad. Sci. U.S.A*. 2009, **106**, 2159.

72 E.S. Pohlmann, K.Patel, S. Guo, M. J. Dukes, Z. Sheng, and D. F. Kelly, *Nano Lett.,* 2015, **15**, 2329−2335.

73 M. J. Dukes, D. F. Kelly, *Chem. Commun.,* 2013, **49**, 3007–3009.

74 R. R. Unocic, R. L. Sacci, G. M. Brown, G. M. Veith, N. J. Dudney, K. L. More, F. S. W. Ii, D. S. Gardiner, J. Damiano and D. P. Nackashi, *Microsc. Microanal.,* 2017, 452–461.

75 M. E. Holtz, Y. Yu, J. Gao, H. D. Abruña and D. A. Muller, *Microsc. Microanal.*, 2013, 1027–1035.

76 N. D. Browning, P. Sciences and S. Abellan, *Chem. Commun.* 2014, **50**, 4873−4880.

77 N. Nanotechnol and N. De Jonge, *Nat. Nanotechnol.,* 2016, 695–704.

78 E. A. Stach, *Mater. Today*, 2008, **11**, 50–58.

79 T. J. Woehl, K. L. Jungjohann, J. E. Evans, I. Arslan, W. D. Ristenpart and N. D. Browning, *Ultramicroscopy*, 2013, **127**, 53–63.

80 T. J. Woehl, J. E. Evans, I. Arslan, W. D. Ristenpart and N. D. Browning, *ACS Nano*, 2012, 8599–8610.

81 R. F. Egerton, P. Li and M. Malac, *Micron*, 2004, **35**, 399–409.

82 T. Huang, S. Liu, Y. Chuang, H. Hsieh, C. Tsai, W. Wu, C. Tsai, U. Mirsaidov, P. Matsudaira, C. Chang, F. Tseng and F. Chen, *Soft Matter.*, 2013, **1**, 8856–8861.

83 J. Hermannsdo, N. de Jongeab and A. Verch, *Chem. Commun*, 2015, 16393–16396.

84 S. Le Caë, *Water*, 2011, **3**, 235–253.

85 T. Yokota, M. Murayama and J. M. Howe, *Phys. Rev. Lett.,* 2003, 1–4.

86 E. R. White, M. Mecklenburg, B. Shevitski, S. B. Singer and B. C. Regan, *Langmuir,* 2012, 8–11.

87 J. Cazaux, *Ultramicroscopy*, 1995, **60**, 41 l-425.

88 T. J. Woehl and T. Prozorov, *J. Phys. Chem. C*, 119, 36, 21261-21269.

89 W. H. Hamill, *J. Phys. Chem.,* 1969, **5**, 1341–1347.

90 N. M. Schneider, M. M. Norton, B. J. Mendel, J. M. Grogan, F. M. Ross and H. H. Bau, *J. Phys. Chem. C* 2014, **118**, 22373−22382.

91 T.J. Woehl, P. Abellen, *J. of Microscopy*, 2017, **265**, 135–147.

92 K. R. Siefermann, Y. Liu, E. Lugovoy, O. Link, M. Faubel, U. Buck, B. Winter and B. Abel, *Nat. Chem.*, 2010, **2**, 274–279.

93 M. Den Heijer, I. Shao, A. Radisic, M. C. Reuter, F. M. Ross, *APL Materials,* 2014, **2**, 022101.

94 T. J. Woehl, K. L. Jungjohann, J. E. Evans, I. Arslan, W. D. Ristenpart and N. D. Browning, *Ultramicroscopy*, 2013, **127**, 53–63.

95 J. E. Evans, K. L. Jungjohann, N. D. Browning and I. Arslan, *Nano Lett.*, 2011, **11**, 2809–2813.

96 L. R. Parent, D. B. Robinson, T. J. Woehl, W. D. Ristenpart, J. E. Evans, N. D. Browning and I. Arslan, *ACS Nano*, 2012, 3589–3596.

97 K. L. Jungjohann, S. Bliznakov, P. W. Sutter, E. A. Stach and E. A. Sutter, *Nano Lett.* 2013, **13**, 2964−2970.

98 J. Park, S. Kodambaka, F. M. Ross, J. M. Grogan and H. H. Bau, *Microsc. Microanal.*, 2012, **18**, 1098–1099.

99 Q. Chen, H. Cho, K. Manthiram, M. Yoshida, X. Ye and A. P. Alivisatos, *ACS Cent. Sci.*, 2015, **1**, 33-39.

100 Y. Zhao, L. Zhan, J. Tian, S. Nie and Z. Ning, *Electrochim. Acta*, 2011, **56**, 1967–1972.

101 J. Yang, C. M. Andrei, G. A. Botton and L. Soleymani, *J. Phys. Chem. C*, 2017, **121**, 7435–7441.

102 D. B. Peckys, *ACS Nano*, 2016, 9061–9063.

103 J. H. Park, N. M. Schneider, J. M. Grogan, M. C. Reuter, H. H. Bau, S. Kodambaka and F. M. Ross, *Nano Lett.*, 2015, **15**, 5314–5320.

104 Y. Liu, K. Tai and S. J. Dillon, *Chem. Mater.* 2013, **25**, 2927−2933.

105 H. Liao, L. Cui, S. Whitelam and H. Zheng, *Science*, 2012, **336**, 1011–1015.

106 M. Egawa, T. Ishida, L. Jalabert, H. Fujita, M. Egawa, T. Ishida, L. Jalabert and H. Fujita, *Appl. Phys. Lett.,* 2016,108, 023104.

107 J. H. Park, N. M. Schneider, J. M. Grogan, M. C. Reuter, H. H. Bau, S. Kodambaka and F. M. Ross, *Nano Lett.*, 2015, **15**, 5314–5320.

108 B. L. Mehdi, J. Qian, E. Nasybulin, C. Park, D. A. Welch, R. Faller, H. Mehta, W. A. Henderson, W. Xu, C. M. Wang, J. E. Evans, J. Liu, J. G. Zhang, K. T. Mueller and N. D. Browning, *Nano Lett.*, 2015, **15**, 2168–2173.

109 K. L. Klein, I. M. Anderson and N. de Jonge, *J. Microsc.*, 2011, **242**, 117–23.

110 J. M. Grogan, N. M. Schneider, F. M. Ross and H. H. Bau, *Nano Lett.,* 2014, **4**, 0–5.

111 D. B. Peckys, G. M. Veith, D. C. Joy and N. De Jonge, *PLoS ONE,* 2009, **4**, 1–7.

112 J. M. Grogan, L. Rotkina and H. H. Bau, *Phys. Rev. E* 2011, **83**, 1−5.

113 A. Verch and N. De Jonge, *Chem. Commun.*, 2015, 51, 16393-16396.

114 D. B. Peckys, P. Mazur, K. L. Gould and N. De Jonge, *Biophysj*, 2011, **100**, 2522–2529.

115 D. B. Peckys and N. De Jonge, *Microsc. Microanal.,* 2017, 346–365.

116 M. J. Dukes, D. B. Peckys and N. De Jonge, *ACS Nano,* 2010**, 4,** 4110−4116.

117 D. B. Peckys and N. De Jonge, *Nano Lett*, 2011, 1733–1738.

118 Y. Wang, X. Chen, H. Cao, C. Deng, X. Cao and P. Wang, *J. Anal. Methods Chem.*, 2015, 829302.

119 K. Liu, C. Wu, Y. Huang, H. Peng and H. Chang, *Lab chip,* 2008, 1915–1921.

120 E. Kennedy, E. M. Nelson, T. Tanaka, J. Damiano and G. Timp, *ACS Nano*, 2016, **10**, 2669−2677.

121 T. J. Woehl, S. Kashyap, E. Firlar, T. Perez-gonzalez, D. Faivre, D. Trubitsyn, D. A. Bazylinski and T. Prozorov, *Scientific Reports*, 2014, 22–29.

122 H. Liao and H. Zheng, *J. Am. Chem. Soc.*, 2013, 135, 5038–5043.

123 M. H. Nielsen, S. Aloni, J. J. De Yoreo, *Science,* 2014, **345**, 1158-1162.

124 K. Niu, J. Park, H. Zheng and A. P. Alivisatos, *Nano Lett.*, 2013, **13**, 5715–5719.

125 M. Den Heijer, I. Shao, A. Radisic, M. C. Reuter and F. M. Ross, *APL Mater.*, 2014, **2**, 022101.

126 N. M. Schneider, J. Hun Park, J. M. Grogan, S. Kodambaka, D. a. Steingart, F. M. Ross and H. H. Bau, *Microsc. Microanal.*, 2014, **20**, 1530–1531.

127 M. Egawa, T. Ishida, L. Jalabert and H. Fujita, *Appl. Phys. Lett.*, 2016,**108**, 023104.

128 A. J. Leenheer, J. P. Sullivan, M. J. Shaw and C. T. Harris, *J. Microelectromechanical system,* 2015, **24**, 1061–1068.

129 E. R. White, S. B. Singer, V. Augustyn, W. A. Hubbard, M. Mecklenburg, B. Dunn and B. C. Regan, *ACS Nano,* 2012, 6308–6317.

130 S. Schilling, A. Janssen, N. J. Zaluzec and M. G. Burke, *Microsc. Microanal.*, 2017, **23**, 741–750.

131 Y. Yu, M. E. Holtz, H. L. Xin, D. Wang, H. D. Abruña and D. A. Muller, *Microsc. Microanal.,* 2013, **19**, 1666–1667.

132 G.-Z. Zhu, S. Prabhudev, J. Yang, C. M. Gabardo, G. A. Botton and L. Soleymani, *J. Phys. Chem. C*, 2014, **118**, 22111–22119.

133 M. E. Holtz, Y. Yu, D. Gunceler, J. Gao, R. Sundararaman, K. a Schwarz, T. a Arias, H. D. Abruña and D. a Muller, *Nano Lett.*, 2014, **14**, 1453–9.

134 X. H. Liu and J. Y. Huang, *Energy Environ. Sci.*, 2011, **4**, 3844.

135 B. L. Mehdi, J. Qian, E. Nasybulin, C. Park, D. A. Welch, R. Faller, H. Mehta, W. A. Henderson, W. Xu, C. M. Wang, J. E. Evans, J. Liu, J. G. Zhang, K. T. Mueller and N. D. Browning, *Nano Lett.*, 2015, **15**, 2168–2173.

136 P. Abellan, B. L. Mehdi, L. R. Parent, M. Gu, C. Park, W. Xu, Y. Zhang, I. Arslan, J. G. Zhang, C. M. Wang, J. E. Evans and N. D. Browning, *Nano Lett.*, 2014, **14**, 1293–1299.

137 R. R. Unocic, X. Sun, R. L. Sacci, L. A. Adamczyk, D. H. Alsem, S. Dai, N. J. Dudney and K. L. More, *Microsc. Microanal.*, 2017, 1029–1037.

138 R. L. Sacci, N. J. Dudney, K. L. More, L. R. Parent, I. Arslan, N. D. Browning and R. R. Unocic, *Microsc. Microanal.,* 2014, 2104–2107.

139 B. L. Mehdi, M. Gu, L. R. Parent, W. Xu, E. N. Nasybulin, X. Chen, R. R. Unocic,

P. Xu, D. A. Welch, P. Abellan, J. Zhang, J. Liu, C. Wang, I. Arslan, J. Evans and N. D. Browning, *Microsc. Microanal.,* 2017, 484–492.

140 J. M. Yuk, H. K. Seo, J. W. Choi and J. Y. Lee, *ACS Nano*, 2014, 7478–7485.

141 Z. Zeng, W. Liang, H. Liao, H. L. Xin, Y. Chu and H. Zheng, *Nano Lett.,* 2014, **14**, 1745–1750.

142 M. Y. Abyaneh and M. Fleischmann, *J. Electroanal Chem.,* 2002, **530**, 108–118.

143 M. Y. Abyaneh and M. Fleischmann, *J. Electroanal Chem.,* 2002, **530**, 123–125.

144 M. Egawa, T. Ishida, L. Jalabert and H. Fujita, *Appl. Phys. Lett.,* 2016,**108**, 023104

145 M. J. Platek, O. J. Gregory, T. Duarte, J. C. Oxley, J. L. Smith and E. Bernier, *Microsc. Microanal.*, 2010, **16**, 1570–1.

146 S. O. Kelley, C. a Mirkin, D. R. Walt, R. F. Ismagilov, M. Toner and E. H. Sargent, *Nat. Publ. Gr.*, 2014, **9**, 969–980.

147 X. Zheng, W. Smith, J. Jackson, B. Moran, H. Cui, D. Chen, J. Ye, N. Fang, N. Rodriguez, T. Weisgraber and C. M. Spadaccini, *Nat. Mater.*, 2016, 1–8.

148 L. Soleymani, Z. C. Fang, E. H. Sargent and S. O. Kelley, *Nat. Nanotechnol.*, 2009, **4**, 844–848.

149 L. Soleymani, Z. Fang, X. Sun, H. Yang, B. J. Taft, E. H. Sargent and S. O. Kelley, *Angew. Chem. Int. Ed. Engl.*, 2009, **48**, 8457–60.

150 C. J. Johnson, E. Dujardin, S. A. Davis, C. J. Murphy and S. Mann, *J. Mater. Chem.*, 2002, **12**, 1765–1770.

151 T. K. Sau and C. J. Murphy, *J. Am. Chem. Soc.*, 2004, **126**, 8648–8649.

152 A. V Ievlev, S. Jesse, T. J. Cochell, R. R. Unocic, V. A. Protopopescu and S. V Kalinin, *ACS Nano*, 2015, **9**, 11784–11791.

153 D. Alloyeau, W. Dachraoui, Y. Javed, H. Belkahla, G. Wang, H. Lecoq, S. Ammar, O. Ersen, A. Wisnet. F. Gazeau, and C. Ricolleau, *Nano Lett*., 2015, **15**, 2574–2581.

154 Y. Jiang, G. Zhu, F. Lin, H. Zhang, C. Jin, J. Yuan, D. Yang and Z. Zhang, *Nano Lett.,* 2014, 1**4**, 3761–3765.

155 Y. J. Tan and K. Y. Lim, *Surf. Coatings Technol.*, 2003, **167**, 255–262.

156 L. Guo and P. C. Searson, *Electrochim. Acta*, 2010, **55**, 4086–4091.

157 J. Hermannsdörfer, N. de Jonge and A. Verch, *Chem. Commun.*, 2015, **51**, 16393–16396.

158 G. Gunawardena and G. Hills, *Chem. Interfacia*, 1982, **138**, 225–239

159 D. Drouin, A. R. Couture, D. Joly, X. Tastet, V. Aimez and R. Gauvin, *Scanning*, 2007, **29**, 92–101.

160 J. Pavlovski, S. Myrskog, P. Dufour, C. M. Gabardo and L. Soleymani, *J. Electrochem. Soc.*, 2015, **162**, D503–D508.

161 G. Gunawardena and G. Hills, *Chem. Interfacial*, 1982, **138**, 225–239.

162 B. Scharifker and G. Hills, *Electrochim. Acta*, 1983, **28**, 879–889.

163 T. M. Squires, R. J. Messinger and S. R. Manalis, *Nat. Biotechnol.*, 2008, **26**, 417–426.

164 G.-Z. Zhu, S. Prabhudev, J. Yang, C. M. Gabardo, G. a. Botton and L. Soleymani, *J. Phys. Chem. C*, 2014, **118**, 22111–22119.

165 C. M. Gabardo, J. Yang, N. J. Smith, R. C. Adams-McGavin and L. Soleymani, *ACS Nano*, 2016, **10**, 8829–8836.

166 Y. Hu, J. Jin, P. Wu, H. Zhang and C. Cai, *Electrochim. Acta*, 2010, **56**, 491–500.

167 L. Soleymani, Z. Fang, S. O. Kelley and E. H. Sargent, *Appl. Phys. Lett.*, 2009, **95**, 143701.

168 A. L. González, C. Noguez and A. S. Barnard, *J. Phys. Chem. C*, 2012, **116**, 14170–14175.

169 Y. Tian, H. Liu, G. Zhao and T. Tatsuma, *J. Phys. Chem. B*, 2006, **110**, 23478–23481.

170 Y. Jiang, Z. Wang, X. Yu, F. Shi, H. Xu, X. Zhang, M. Smet and W. Dehaen, *Langmuir*, 2005, **21**, 1986–1990.

171 B. Wiley and Y. Sun, *Acc. Chem. Res.*, 2007, **40**, 1067–1076.

172 M. Martín-González, G. J. Snyder, A. L. Prieto, R. Gronsky, T. Sands and A. M. Stacy, *Nano Lett.*, 2003, **3**, 973–977.

173 L. Chen, Y. Tang, K. Wang, C. Liu and S. Luo, *Electrochem. commun.*, 2011, **13**, 133–137.

174 C. Zhu, G. Meng, Q. Huang, Z. Zhang, Q. Xu, G. Liu, Z. Huang and Z. Chu, *Chem. Commun.*, 2011, **47**, 2709–2711.

175 T.-H. Lin, C.-W. Lin, H.-H. Liu, J.-T. Sheu and W.-H. Hung, *Chem. Commun.*, 2011, **47**, 2044.

176 C. M. Gabardo, Y. Zhu, L. Soleymani and J. M. Moran-Mirabal, *Adv. Funct. Mater.*, 2013, **23**, 3030–3039.

177 M. Matsushita, M. Sano, Y. Hayakawa, H. Honjo and Y. Sawada, *Phys. Rev. Lett.*, 1984, **53**, 286–289.

178 Y. Yang and Y. F. Cheng, *Surf. Coatings Technol.*, 2013, **216**, 282–288.

179 N. D. Nikolic, M. G. Pavlovic and K. I. Popov, *J. Electroanal. Chem.*, 2006, **588**, 88–98.

180 A. P. F. Turner, *Chem. Soc. Rev.*, 2013, **42**, 3184–3196.

181 B. R. Evans, H. M. O'Neill, V. P. Malyvanh, I. Lee and J. Woodward, *Biosens. Bioelectron.*, 2003, **18**, 917–923.

182 M. Krishna Kumar and S. Ramaprabhu, *Int. J. Hydrogen Energy*, 2007, **32**, 2518–2526.

183 H.-H. Hsu, P. R. Selvaganapathy and L. Soleymani, *J. Electrochem. Soc.*, 2014, **161**, D3078–D3086.

184 G. Lu and G. Zangari, *J. Phys. Chem. B*, 2005, **109**, 7998–8007.

185 L. Hsu, L. Soleymani, P. R. Selvaganapathy, *J. Electrochem. Soc.*, 2014, **161**, D3078–D3086.

186 Y. I. Yanson and M. J. Rost, *Angew. Chemie - Int. Ed.*, 2013, **52**, 2454–2458.

187 W. Shao, G. Pattanaik and G. Zangari, *J. Electrochem. Soc.*, 2007, **154**, D201.

188 L. Xu, Y. Guo, Q. Liao, J. Zhang and D. Xu, *J. Phys. Chem. B*, 2005, **109**, 13519–13522.

189 Y. Tsuru, M. Nomura and F. R. Foulkes, *J. Appl. Electrochem.*, 2000, **30**, 231–238.

190 J. C. Canullo and A. J. Arvia, *J. Electroanal. Chem.*, 1986, **215**, 317-329.

191 Y. Gimeno, A. Herna, P. Carro, S. Gonza and R. C. Salvarezza, *J. Phys. Chem. B*, 2002, 4232–4244.

192 M. Wojnicki, K. Pacławski, E. Rudnik and K. Fitzner, *Hydrometallurgy*, 2011, **110**, 56–61.

193 Y. Gimeno, A. Hernández Creus, P. Carro, S. González, R. C. Salvarezza and A. J. Arvia, *J. Phys. Chem. B.,* 2002, **106**, 4232–4244.

194 B. L. Mehdi, A. Stevens, J. Qian, C. Park, W. Xu, W. A. Henderson, J. G. Zhang, K. T. Mueller and N. D. Browning, *Sci. Rep.*, 2016, **6**, 1–8.

195 H. M. Khan, W. L. Waltz and R. J. Woods, *Radiat. Phys. Chem.,* 1986, **27**, 41–45.

196 A. J. Bard and L. R. Faulkner, *Electrochemical methods: fundamentals and applications*, John Wiley & Son, Inc., New York, 2nd edn., 2001.

197 G. Jerkiewicz, *Prog. Surf. Sci.*, 1998, **57**, 137–186.

198 Y. L. Wang, Y. Q. Zhao, C. L. Xu, D. D. Zhao, M. W. Xu, Z. X. Su and H. L. Li, *J.*

Power Sources, 2010, **195**, 6496–6499.

199 C. L. Lee and H. P. Chiou, *Appl. Catal. B Environ.*, 2012, **117–118**, 204–211.

200 H. Heydari, A. Abdolmaleki, M. B. Gholivand and H. Shayani-jam, *Ciencia e Natura, Santa Maria*, 2015, 23–33.

201 N. Hoshi, M. Nakamura and S. Kondo, *Electrochem. commun.*, 2009, **11**, 2282–2284.

202 G.-Y. Gao, D.-J. Guo and H.-L. Li, *J. Power Sources*, 2006, **162**, 1094–1098.

203 M. Shao, J. Odell, M. Humbert, T. Yu and Y. Xia, *J. Phys. Chem. C*, 2013, **117**, 4172–4180.

204 R. Kazemi and A. Kiani, *Int. J. Hydrogen Energy*, 2012, **37**, 4098–4106.

205 S. Hu, J. Noborikawa, J. Haan, L. Scudiero and S. Ha, *ECS Trans.*, 2014, **64**, 1113–1120.

206 S. Mukdasai, U. Crowley, M. Pravda, X. He, E. P. Nesterenko, P. N. Nesterenko, B. Paull, S. Srijaranai, J. D. Glennon and E. Moore, *Sensors Actuators, B Chem.*, 2015, **218**, 280–288.

207 S. H. Lim, J. Wei, J. Lin, Q. Li and J. KuaYou, *Biosens. Bioelectron.*, 2005, **20**, 2341–2346.

208 S. Mubeen, T. Zhang, B. Yoo, M. A. Deshusses and N. V. Myung, *J. Phys. Chem. C*, 2007, **111**, 6321–6327.

209 A. Safavi, N. Maleki, F. Farjami and E. Farjami, *J. Electroanal. Chem.*, 2009, **626**, 75–79.

210 A. Safavi, N. Maleki, F. Tajabadi and E. Farjami, *Electrochem. commun.*, 2007, **9**, 1963–1968.

211 A. Zalineeva, S. Baranton, C. Coutanceau and G. Jerkiewicz, *Sci. Adv.*, 2017, **3**, e1600542.

212 T. Mehner, D. Nickel, S. Nehrkorn, A. Yulinova, M. Pügner, I. Scharf, G. Lanzinger, R. Böck and T. Lampke, *Adv. Eng. Mater.*, 2015, **17**, 167–171.

213 C. D. Weber, C. Bradley and M. C. Lonergan, *J. Mater. Chem.*, 2014, **2**, 303.

214 Y. Yu, M. E. Holtz, H. L. Xin, D. Wang, H. D. Abruña and D. A. Muller, *Microsc. Microanal.,* 2013, **19**, 1666–1667.

215 J. Genesca, *Electrochim. Acta*, 32 (1987) 541-544..

216 M. Seo and M. Aomi, *J. Electrochem. Sot.*, 1993, **347**, 185–194.

217 J. M. Wheeler and T. W. Clyne, *Int. J. Hydrogen Energy*, 2012, **37**, 14315–14322.

218 F. D. Manchester, A. San-Martin and J. M. Pitre, *J. Phase Equilibria*, 1994, **15**, 62–83.

219 T. C. Narayan, F. Hayee, A. Baldi, A. Leen Koh, R. Sinclair and J. A. Dionne, *Nat. Commun.*, 2017, **8**, 1–8.

220 R. Griessen, N. Strohfeldt and H. Giessen, *Nat. Mater.*, 2016, **15**, 311–317.

221 H. Naohara, S. Ye and K. Uosaki, *Colloids Surfaces A Physicochem. Eng. Asp.*, 1999, **154**, 201–208.

222 S. Weiner and P. M. Dove, *Rev. Mineral.*, 2003, **54**, 1–29.

223 L. Addadi and S. Weiner, *Phys. Scr.*, 2014, **89**, 098003.

224 S. V. Dorozhkin, *Materials (Basel).*, 2009, **2**, 399–498.

225 L. Guangbin, D. Patricia, M. M. D., P. G. J., L. Evelyne, B. R. R. and K. Gerard, *Nature*, 1997, **386**, 78–81.

226 S. V Dorozhkin and M. Epple, *Angew. Chemie Int. Ed.*, 2002, **41**, 3130–3146.

227 A. J. Yiu, D. Callaghan, R. Sultana and B. C. Bandyopadhyay, *J. Cardiovasc. Dev. Dis.*, 2015, **2**, 141–164.

228 A. Dey, P. H. Bomans, F. a Muller, J. Will, P. M. Frederik, G. de With and N. a Sommerdijk, *Nat. Mater.*, 2010, **9**, 1010–1014.

229 W. J. E. M. Habraken, J. Tao, L. J. Brylka, H. Friedrich, L. Bertinetti, A. S. Schenk, A. Verch, V. Dmitrovic, P. H. H. Bomans, P. M. Frederik, J. Laven, P. van der Schoot, B. Aichmayer, G. de With, J. J. DeYoreo and N. a. J. M. Sommerdijk, *Nat. Commun.*, 2013, **4**, 1507.

230 A. E. S. Van Driessche, M. Kellermeier, L. G. Benning and D. Gebauer, *New Perspectives on Mineral Nucleation and Growth*, Springer, 2017.

231 F. Nudelman, A. J. Lausch, N. a J. M. Sommerdijk and E. D. Sone, *J. Struct. Biol.*, 2013, **183**, 258–269.

232 J. Mahamid, B. Aichmayer, E. Shimoni, R. Ziblat, C. Li, S. Siegel, O. Paris, P. Fratzl, S. Weiner and L. Addadi, *Proc. Natl. Acad. Sci.*, 2010, **107**, 6316–6321.

233 S. Boonrungsiman, E. Gentleman, R. Carzaniga, N. D. Evans, D. W. McComb, A. E. Porter and M. M. Stevens, *Proc. Natl. Acad. Sci.*, 2012, **109**, 14170–14175.

234 J. J. De Yoreo, P. U. P. A. Gilbert, N. A. J. M. Sommerdijk, R. L. Penn, S. Whitelam, D. Joester, H. Zhang, J. D. Rimer, A. Navrotsky, J. F. Banfield, A. F. Wallace, F. M. Michel, F. C. Meldrum, H. Colfen and P. M. Dove, *Science*, 2015, **349**, aaa6760-aaa6760.

235 P. J. M. Smeets, K. R. Cho, R. G. E. Kempen, N. A. J. M. Sommerdijk and J. J. De

Yoreo, *Nat. Mater.*, 2015, **14**, 394–399.

236 M. H. Nielsen, S. Aloni and J. J. De Yoreo, *Science.*, 2013, **218**, 213–218.

237 N. De Jonge and F. M. Ross, *Nat. Nanotechnol.*, 2011, **103**, 695–704.

238 F. M. Ross, *Science*, 2015, **350**, 1–9.

239 A. Verch, I. E. G. Morrison, R. Van De Locht and R. Kröger, *J. Struct. Biol.*, 2013, **183**, 270–277.

240 M. J. Olszta, X. Cheng, S. S. Jee, R. Kumar, Y. Y. Kim, M. J. Kaufman, E. P. Douglas and L. B. Gower, *Mater. Sci. Eng. R Reports*, 2007, **58**, 77–116.

241 A. J. Lausch, B. D. Quan, J. W. Miklas and E. D. Sone, *Adv. Funct. Mater.*, 2013, **23**, 4906–4912.

242 F. Nudelman, K. Pieterse, A. George, P. H. H. Bomans, H. Friedrich, L. J. Brylka, P. A. Hilbers, G. de With and N. a. J. M. Sommerdijk, *Nat. Mater.*, 2010, **9**, 1004–1009.

243 B. E. Deshpande A.S., *Cryst Growth Des.*, 2008, **8**, 3084–3090.

244 P. J. M. Smeets, K. R. Cho, R. G. E. Kempen, N. a J. M. Sommerdijk and J. J. De Yoreo, *Nat. Mater.*, 2015, **4193**, 1–6.

245 M. E. Holtz, Y. Yu, J. Gao, H. D. Abruña and D. a. Muller, *Microsc. Microanal.*, 2013, **19**, 1027–1035.

246 N.M. Schneider, M.M. Norton, B.J. Mendel, J.M. Grogan, F.M. Ross and H.H. Bau, *J. Phys. Chem. C*, 2014, **118** , 22373–22382.

247 K. Nitiputri, Q. M. Ramasse, H. Autefage, C. M. McGilvery, S. Boonrungsiman, N. D. Evans, M. M. Stevens and A. E. Porter, *ACS Nano*, 2016, **10**, 6826–6835.

248 A. P. F. Turner, *Science*, 2000, **290**, 1315–1317.

249 T. G. Drummond, M. G. Hill and J. K. Barton, *Nat. Biotechnol.*, 2003, **21**, 1192–1199.

250 C. A. Mirkin, R. L. Letsinger, R. C. Mucic and J. J. Storhoff, *Nature*, 1996, **382**, 607–609.

251 J. M. Nam, S. I. Stoeva and C. A. Mirkin, *J. Am. Chem. Soc.*, 2004, **126**, 5932–5933.